FINITE ELEMENT MODELING OF LEAD ACID BATTERIES

A THESIS

SUBMITTED IN FULFILMENT

OF THE REQUIREMENTS FOR THE DEGREE

OF

DOCTOR OF PHILOSOPHY

AT THE

UNIVERSITY OF WAIKATO

By

GEOFFREY JAMES FOSTER

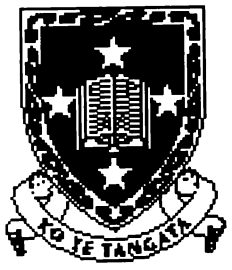

The University of Waikato

Te Whare Wānanga o Waikato

UNIVERSITY OF WAIKATO

1998

This work is dedicated to the memory of my late Mother.

ACKNOWLEDGEMENTS

I would like to thank my advisor and mentor, Associate Professor Evan Bydder for the project, the guidance, support, and the encouragement he has given over the years. Evan's ability to tackle hands on, seemingly impossibly complicated problems and treat them from first principles was not only the source of motivation for this work, but has spawned my own skill-set with which I now approach any task.

I am grateful to my sponsoring company, Power Beat International Limited for allowing me to work on a meaningful project.

I would like to thank FORST and and more specifically, the Technology for Business Growth scheme for their financial input.

A very warm thank you to my friends who have helped, supported and gone out of their way to accommodate me in order to finish this project.

I am grateful to my father and especially my late mother whose compassion, love and dependability will always be remembered.

TABLE OF CONTENTS

LIST OF TABLES

LIST OF FIGURES

FINITE ELEMENT MODELING OF LEAD ACID BATTERIES

By

Geoffrey James Foster

This thesis investigates the finite element method with regard to the macrohomogeneous theory for flooded porous electrochemical cells, more specifically lead-acid cells. One- and two-dimensional finite element models are developed for flooded porous electrochemical lead acid cells. Chapter One introduces the background of the technology of lead-acid batteries, theory fundamentals, previous mathematical models for lead acid batteries, and the reason for the work. Chapter Two develops Newman's macrohomogeneous equations for flooded porous electrodes. Chapter Three details the finite element theory, and how it is used to solve time dependent coupled non-linear partial differential equations. Chapter Four applies finite element theory to one-dimensional macrohomogeneous equations that describe lead-acid batteries. The results of the model are compared to previously published papers utilising finite difference methods. In Chapter Five, the technique is extend to two-dimensions and is validated with previously published papers of models on lead-acid batteries.

CHAPTER 1
THE LEAD-ACID BATTERY

1.1 Overview

This chapter is divided into two parts. The first section discusses lead-acid battery technology. This ranges from the historical origin, to its fundamental theory and the pertinent parameters which are used to design the battery for its intended application. The second part of this chapter leads into the subject of this thesis, i.e. mathematical models of lead-acid batteries. The types of models published and how they can be used to optimise lead-acid batteries are discussed . The principle model reviewed is Newman's macrohomogeneous model. The technique used to numerically solve the resultant partial differential equations, the finite element method, is then introduced. This is principally the purpose for this thesis.

1.2 Introduction

The lead-acid battery system is the most widely manufactured secondary battery system in the world today. In fact it is manufactured in nearly every country of the world. Applications range from small sealed batteries of a few watt-hour capacity to large batteries of many megawatt-hours capacity. Lead-acid batteries are used in small electrical devices such as radios, laptop computers, to cars, to emergency power supplies, to submarines and for load load-leveling applications. Over 75% of all lead-acid batteries manufactured are for automotive applications. In 1991, 238.3 million automotive batteries were shipped worldwide [Bullock 94]. Generally, the applications for lead-acid batteries can be classified in the following manner.

The Starting Lighting Ignition Battery (SLI): SLI is the common term for the battery used to start an internal combustion engine and to power the electrical system in emergencies when the engine is not running. More storage batteries are used in this application than any other.

Stationary Batteries: Lead storage batteries are applicable to communications systems, electric utilities, computer systems, emergency lighting, and railways to provide peak loads, emergency power, or filtering of ac power.

Motive Power Batteries: Lead storage batteries provide power for the propulsion of electric lift trucks, mining equipment, street delivery vehicles, and other types of materials handling.

Special Purpose Batteries: Aircraft, submarine, marine, special military, and small sealed batteries (SLAB) for consumer applications.

1.3 A Brief History of Lead-Acid Batteries

Galvani's "frog leg experiment" in 1789 [Bode 77] can be considered to be the starting point for an electrochemical source of current. Following Galvani's experiment, Volta developed his "Volta pile" [Bode 77]. He later postulated his "dry contact theory".

In 1803 Ritter [Ritter 1803] observed that an electrical current passed between two like electrodes in an electrolyte produced polarisation. After the source of current has been disconnected the polarised assembly yields a current in the reverse direction. Ritter's pile represented the starting point for the secondary battery.

Planté in 1859 [Planté 1959] found that lead electrodes can be permanently polarised by an external current source and that the arrangement constituted a relatively efficient means of storing energy. It was really the first lead-acid battery. He found that the amount of stored energy depended on the amount of lead dioxide formed. Nine years later Planté discovered the capacity could be increased by longer

or repeated charges in a process he called "forming", which was published 3 years later in 1872 [Planté 1872]. The Planté cell was born, and has remained basically the same since.

In 1881 Fraure [Fraure 1881] coated lead foil with lead oxide. Two years later Tudor [Vinal 55] pasted the oxide on cast ribbed lead plates which were pre-formed according to the Planté method for better adhesion. The flooded porous pasted electrodes dramatically increased the capacity of the lead-acid system. Since then an assortment of grid designs have been developed for the retention of the active material and transmission of electrical current. At first they were perforated or slitted plates, but later horizontal and vertical or diagonal rods of various cross sections were added. From these earlier designs we have the flooded porous plates used today.

Antimony was first added to the grids in 1881 [Bode 77]. It has been found to increase the hardness, lower the casting temperature of the grid and increase cycling life of the plate. It has the disadvantage of increasing water loss of the lead-acid battery.

In 1955 the Calcium-Lead plate was introduced [Bode 77]. It increases the structural strength and practically eliminates the so called water loss effect that occurs with antimony plates. This allows for low maintenance batteries.

Essentially, the lead-acid battery has changed only in details of manufacture since 1881. The greatest improvements in the development of the lead-acid battery have been made because of the porous electrode.

1.4 Active Materials

The reaction at the electrodes on charge and discharge are given in the "double sulphate" theory:

The overall discharge reaction of the lead-dioxide electrode is:

$$PbO_2 + Pb + 2H_2SO_4 \rightleftharpoons 2PbSO_4 + 2H_2O \tag{1.1}$$

This equation shows the relevant stoichiometric ratios and shows the importance sulphuric acid plays as an active material. However the enthalpy, Gibbs free energy and its temperature coefficients for this chemical reaction do not completely agree with theory [Bode 77]. For example, the discovery of two forms of lead dioxide lead to new thermodynamic values. The free energies of the two lead dioxides are practically the same, however the entropies differ considerably. The kinetics of the reactions from the stoichiometry and thermodynamics are not yet completely explained. Indeed experimentally determined values are generally used.

A brief description of the physical properties of the reactants follows. For further data refer to [Bode 77].

1.4.1 Lead Pb

Although a naturally occurring element, the lead used in the batteries is mainly derived from the recycling of the batteries themselves. It is a soft ductile metal of atomic number 82. A freshly prepared surface of lead has a metallic luster that is rapidly oxidised in air. Its crystal structure is a face-centered unit cell.

1.4.2 Lead Dioxide PbO_2

PbO_2 is polymorphous. The following forms are found or believed to occur:

$\alpha - PbO_2$, a rhombic form (columbite);

$\beta - PbO_2$, a tetragonal form (rutile); and

an undetermined pseudotetragonal form [Bode 77].

$\beta - PbO_2$ is converted to $\alpha - PbO_2$ during grinding and under high pressure. The reverse process is not readily seen. Various chemical procedures are used to produce the pure forms. These methods are generally prefered to the electrochemical process [Bode 77].

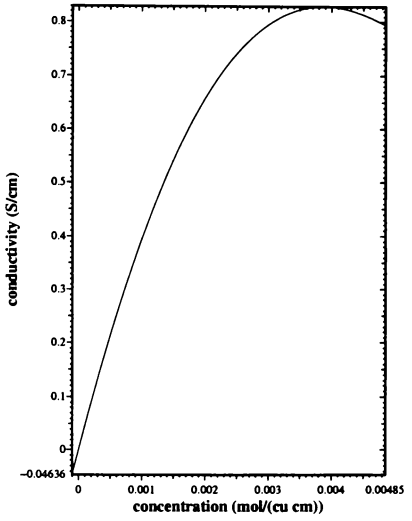

Figure 1.1: Sulphuric acid conductivity as a function of concentration at 25 C.

1.4.3 Lead Sulphate $PbSO_4$

During discharge lead sulphate, $PbSO_4$, is formed on both electrodes. It is an insulator and has a low solubility in sulphuric acid.

1.4.4 Sulphuric Acid H_2SO_4

Sulphuric acid is manufactured commercially by the oxidation of sulphur dioxide. The concentrated acid is a clear, odorless, colorless oily liquid, containing 98.3% H_2SO_4 by mass. Its density is 1.84kg/litre. The density of the electrolyte used for battery ranges from 1.2-1.28 kg/litre. The conductivity of sulphuric acid as a function of concentration is shown in Figure 1.1 [Nguyen *et al* 90].

1.5 Theory Fundamentals

1.5.1 Thermodynamics

Electrochemical reactions transform chemical energy either stored in electrodes or introduced from external sources (fuel cells) into electrical energy. This

process occurs on the discharge of the cell. The transformation is direct, although there is usually some heat energy associated with the reaction.

We can use thermodynamics to describe the transition from initial to final states. However this gives no insight into the kinetics of the processes involved.

Neglecting the properties of the internal surfaces and the charges that can form with the Nernst layer ($< 10^{-6}$m), we can characterise a state function by the pressure, the temperature and the chemical composition and the number of moles n_i of the components.

First Law of Thermodynamics

Firstly we consider two state functions: the enthalpy, $H(P,T,n_i)$, or heat constant at constant pressure and temperature; and the internal energy, $U(V,T,n_i)$, or heat content at constant volume and temperature.

The relation between the enthalpy and heat content is given by $H = U + pV$.

During the transition from an initial state H_1 to a state H_2, energy in the form of work A and heat Q is exchanged with the surroundings to which the first law of thermodynamics applies:

$$\begin{aligned} \Delta H &= A_2 - A_1 + Q_2 - Q_1 \\ &= \Delta A + \Delta Q \end{aligned} \tag{1.2}$$

The enthalpy of a system increases if the system absorbs heat, ΔQ, and/or mechanical work ΔA. ΔA and ΔQ are not state functions, i.e. they depend on the path taken during the exchange of energy.

Second law of Thermodynamics

We consider a further two state functions: The entropy, $S(P,T,n_i)$, the unavailability of a system's energy to do work; and the Gibbs free energy $G(P,T,n_i)$, a measure of the ability of a system's energy to do work.

The second law of thermodynamics is concerned with changes in the entropy of a system:

$$\delta Q_{rev} = T(S_2 - S_1) = T\Delta S \tag{1.3}$$

The Gibbs-Helmholtz equation relates the three functions ΔH, ΔG, and ΔS

$$\begin{aligned} \Delta G = (\Delta A_{rev})_p &= \Delta H - (\Delta Q_{rev})_p \\ &= \Delta H - T\Delta S \end{aligned} \tag{1.4}$$

For a reversible process, the enthalpy consists of useful available work (mechanical or electrical) and heat which is exchanged with the surroundings seen in reversible processes. Reversible processes yield the maximum useful work. For irreversible processes, more heat than is expected from the entropy term is transferred to the surroundings and cannot be recovered if the process is reversed.

The more negative the Gibbs free energy, ΔG, the more useful work can be obtained from reactions that proceed spontaneously and reversibly.

Taking the partial derivatives of G, we arrive at Gibbs's fundamental equation for free energy:

$$\begin{aligned} dG &= \left(\frac{\partial G}{\partial p}\right)_{T,n} dp + \left(\frac{\partial G}{\partial T}\right)_{p,n} dT + \sum_{i=1}^{k} \left(\frac{\partial G}{\partial n_i}\right)_{p,T,n_{j\neq i}} dn_i \\ &= V dp - S dT + \sum_{i=1}^{k} \mu_i dn_i \end{aligned} \tag{1.5}$$

where μ_i is the chemical potential of a system, i.e. μ_i is the change in Gibbs free energy with respect to the change in the amount of substance of the component, n_i with pressure, temperature and other substances being kept constant.

Because the absolute value of the enthalpy H and Gibbs free energy G cannot be determined, only the difference obtained by using an arbitrary selected reference state are used.

Similarly, taking the partial derivatives of the enthalpy:

$$\begin{aligned} dH &= \left(\frac{\partial H}{\partial p}\right)_{T,n} dp + \left(\frac{\partial H}{\partial T}\right)_{p,n} dT + \sum_{i=1}^{k} \bar{H}_i dn_i \\ &= \left(V - T\left(\frac{\partial V}{\partial p}_{p,n}\right)\right) dp + C_p dT + \sum_{i=1}^{k} \left(\frac{\partial H}{\partial n_i}\right)_{p,Tn_{j\neq i}} dn_i \end{aligned} \tag{1.6}$$

where C_p is the molar heat capacity at constant pressure.

Third Law of Thermodynamics

After taking the partial derivatives of the entropy of a system we can arrive at:

$$dS = -\left(\frac{\partial V}{\partial T}\right)_{p,n} dp + \left(\frac{C_p}{T}\right) dT + \sum_{i=1}^{k} \bar{S}_i dn_i \tag{1.7}$$

and $\alpha = (\frac{\partial V}{\partial T})_{p,n}$, where α is the thermal coefficient of thermal expansion. In contrast to H and G, S can be determined absolutely. This property is stated in the third law of thermodynamics, i.e.

$$S_{(T=0K)} = 0 \tag{1.8}$$

1.5.2 Electrochemical Kinetics

Application of thermodynamics to current producing electrochemical systems is only strictly valid at reversible equilibrium when $i \to 0$.

Obviously, when an electrochemical cell is loaded, neither the current density, i, or the deviation of the potential, ΔE, can be neglected.

The difference in electrode potential from the equilibrium potential E_{rev} are termed the overpotential or polarisation η, and can be defined:

$$\eta = E - E_{rev} \tag{1.9}$$

The overvoltage depends on the current density i, measured in Am^{-2} or mAcm^{-2}. The surface area can either be measured in an external geometric surface or an internal porous surface.

The overvoltages are due to physical, chemical, and electrochemical processes. We can further define the overvoltages in the following equation:

$$\eta = \eta_t + \eta_r + \eta_d + \eta_k + \eta_o \tag{1.10}$$

where:

η_t is the transfer overvoltage due to the transfer of charge carriers at phase boundaries.

η_r is the chemical or reaction overvoltage

η_d is the diffusion overvoltage

η_k is the crystallisation overvoltage

η_o is the resistance overvoltage

The reaction and diffusion overpotentials can be grouped together as the concentration overvoltage.

Charge Transfer Overvoltage, η_t

For the charge transfer reaction,

$$Me \rightleftharpoons Me^+_{aq} + e^- \tag{1.11}$$

The rate is determined from Arrhenius equations of partial reactions:

$$v_a = K_1 a(Me) e^{\frac{\Delta G^*_k}{RT}} \tag{1.12}$$

and

$$v_k = K_2 a(Me^+) e^{\frac{-\Delta G^*_k}{RT}} \tag{1.13}$$

where K_1 and K_2 are the rate constants of the anodic forward reaction and the cathodic reverse reaction. The ΔG^* are free energies of activation (the difference between activation energy before the reaction and after).

Concentration Overpotential, η_c

Concentration overpotentials may build up by diffusion or lack of convection or by migration of electrical species in a potential field. The diffusion and convection may be effected by movement of the electrolyte.

The reaction and diffusion overvoltages affect the concentration at the interface, which in turn affects the potential as given by the Nernst equation:

$$\eta_c = \left(\frac{RT}{zF}\right) ln \left[\frac{a(0,t)}{a_0}\right] \tag{1.14}$$

where the activity a_0 lies in the bulk of the solution and $a(0,t)$ occurs at the surface at time t.

Crystallisation Overpotential, η_k

Adsorbed particles in the crystal lattice or the formation of seed crystals in the electrolytes and the electrode cause crystallisation overpotentials.

Concentration effects are encountered in crystallisation phenomena as the formation of seed or nuclei often shows severe inhibition. For example, when $PbSO_4$ is initially formed and no seed is present, a supersaturated solution will occur. There must be a threshold amount of supersaturation before the seed can form. The Gibbs-Thomson equation determines their overvoltage:

$$\eta_k = \frac{-2\sigma V}{zF} d_k \tag{1.15}$$

and

$$\eta_k = \frac{-RT}{zF} \ln\left(\frac{a}{a_s}\right) \tag{1.16}$$

1.6 Flooded Porous Electrodes

Flooded porous electrodes play a very important role in lead-acid battery systems for the following reasons:

Porous electrodes provide an intimate contact of the active electrode material with the electrolyte.

If the intrinsic rate of the heterogeneous electrochemical reaction is slow, a porous electrode can increase the kinetics by providing a large interfacial area per unit volume.

The reactants can be stored in the solution virtually on the electrode surface by means of the porous electrode. This allows for a sustained high-rate discharge.

The compactness of porous electrodes can reduce the ohmic potential drop by reducing the distance through which current must flow. This has obvious advantages in reducing the energy losses in batteries. It can also allow the design of an electrode which controls the driving potential of the reactants.

Porous electrodes are quite different and considerably more complicated than plane electrodes. There are inherent complications due to the intimate contact between the electrode and the electrolyte. Methods have been developed and are continuing to be developed in order to attain a greater understanding for how and why the electrode processes occur nonuniformly through the depth of the electrode. In addition, methods are needed for the optimisation of porous electrodes for the particular application they are required to perform.

1.7 The Capacity of a Lead-Acid Cell

The performance of a lead-acid battery is determined by the composition of its active masses (which determine its capacity), the type of discharge regime it is subject to (outer parameters), and the design of the electrodes (inner parameters).

The parameters which affect the discharge of a lead-acid cell for a given amount of active material are:

Current density

Temperature

Acid concentration

Type of pretreatment

Age

Plate thickness

The main internal parameters which govern a lead-acid cell are:

Structure of the solid materials (chemical composition, crystal morphology)

Pore structure (porosity, pore distribution, tortuosity, inner surface)

Electrical properties (conductivity, impedance).

Structure of the interface (inhibitors, double layer adsorption)

1.7.1 Discharge Behaviour

Despite the specific structures of the active masses, the effects of the discharge conditions on the capacity are almost always identical. This discussion is, however, directed towards SLI batteries with thin plates.

Figures 1.2 and 1.3 [Berndt 70], show the general discharge behaviour of positive and negative electrodes for varying current and temperature. The discharge rate varies from 2.5 to 2400 Am^{-2} and the temperature from -50 to 40°C. We can see that for increasing current and decreasing temperature, the capacity decreases. However, as the current decreases, the capacity depends less on the load and tends to a maximum. We can also state from Figures 1.2 and 1.3 that the electrodes capacity is a function of temperature. Note that the discharge current varies between the positive and negative active masses.

Typically, for positive masses with 10 to 25% α -PbO_2, the mass utilisation is of the order of 55%. For negative masses, the mass utilisation is approximately 60%. Electrodes discharged at high currents can be further discharged with small current densities to remove capacity.

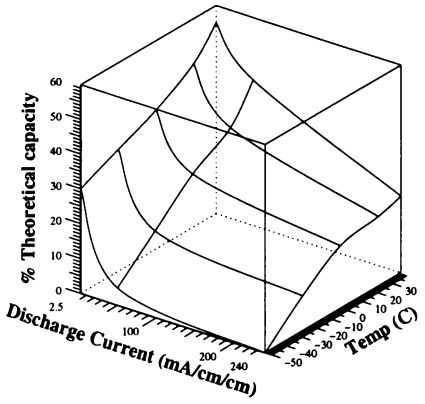

Figure 1.2: Relative discharge capacity of a PbO_2 electrode as a function of current density and discharge temperature.

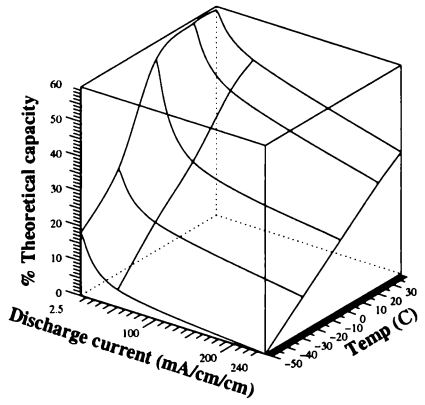

Figure 1.3: Relative discharge capacity of a Pb electrode as a function of current density and discharge temperature.

For the lead dioxide electrode shown in figure 1.2 we note that after a discharge at low temperatures more capacity can be taken out at elevated temperatures. The maximum value depends on the temperature as it does in cells whose capacity is generally determined by the positive electrode active mass.

In negative electrodes, the sum of high and low current capacity is smaller than the capacity obtainable with small currents.

The specific capacity of a cell as a function of acid concentration has a maximum value. This is especially pronounced in thin, lightly loaded plates. This maximum coincides approximately at the maximum conductivity of the acid. However, with high discharge currents and heavy plates other factors obscure this effect [Bode 77]. Figure 1.4 shows the material utilisation as a function of concentration

According to Vinal [Vinal 55], the capacity of a cell which is determined by the positive plate increases linearly with plate thickness. For single electrodes with electrolyte surplus no proportionality is found even at small current densities. The capacity of thick plates reaches a limiting value that depends on the current density.

1.7.2 Volumetric Changes during Discharge

Differences in chemical composition of charged electrodes are due to the changing proportions of α-PbO_2 and β-PbO_2 (a detailed explanation of α- and β- forms of PbO_2 is given in Bode ([Bode 77])) established during manufacture. During discharge the two dioxide modifications produce different specific capacities; β-dioxide is also preferentially discharged in an acidic solution.

$PbSO_4$ formed during discharge on both the positive and negative plates has a larger molar volume than the charged mass. Therefore the volume relationships, and with them the porosity and the inner surface, change. Experimentally, only a small change of the total volume is found in the positive plate during charge and discharge. This change in ΔV_s is taken up by the void volume. For a discharge of β-PbO_2, with a mass utilisation coefficient $\alpha \approx 0.55$, $\Delta V_s = -\Delta V_v = 0.054$ lkg^{-1}.

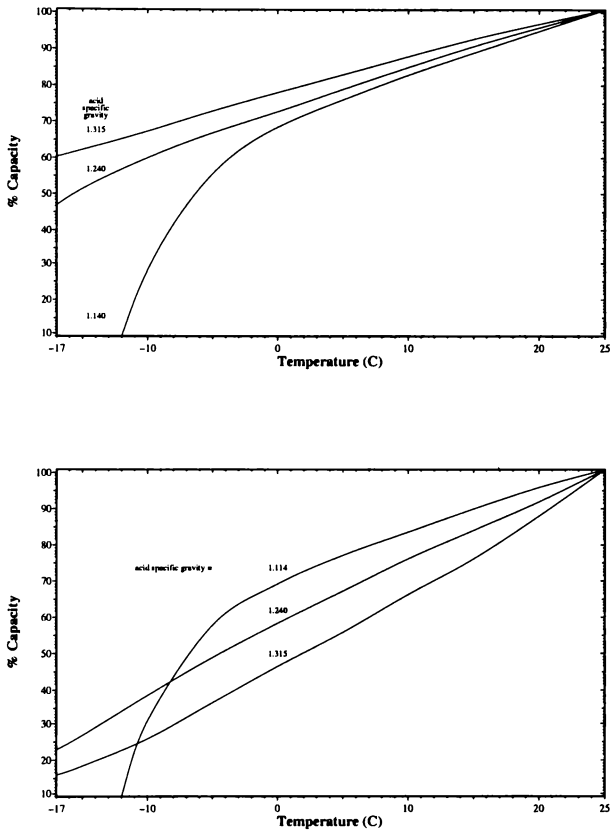

Figure 1.4: Influence of the temperature on the capacity as a function of the acid density; discharge with a 5-hour current. Top = positive plate; bottom = negative plate.

Hence, the porosity ρ is reduced from 54% to 31%. If the volume change ΔV_s is distributed over the BET (Brunnauer, Emmett, and Teller) surface (a technique used to determine the surface area of a porous electrode) [Bode 77] of 4.5 m^2g^{-1}, an increase in thickness of 0.0025 μm lead sulphate results, or 60 molecular layers. The average particle diameter increases by 0.025 μm. The diameter of the pores decreases by approximately the same amount so that the mass transport in the porous positive electrode is only slightly influenced during discharge.

Because of the increase in the volume of solids, the small cracks and pores that constitute the microporosity and the major portion of the inner surface are nearly filled. The measured BET surface decreases during the discharge from about 4.5 to 1 m^2g^{-1} for the positive electrode.

In the negative electrode, the volume change is $\Delta V_s = 0.064\ lkg^{-1}$. Distributed over the BET surface of 0.5 m^2g^{-1}, the increase in thickness is 0.13 μm, and a $PbSO_4$ layer of 0.3 μm thickness forms. The average diameter of the pores changes from approximately 4.0 to 3.7 μm [Simon *et al* 70].

Similarly, volume changes can be deduced from electrical data. For example, consider a positive plate discharged at a slow rate, at room temperature. If it delivers about 120 $Ahkg^{-1}$, this will correspond to an active mass usage of $\alpha = 0.54$. This corresponds to the formation of 0.108 litres of $PbSO_4kg^{-1}$. With an assumed BET surface of 4.5 m^2kg^{-1}, the thickness of the sulphate layer can be calculated to be 0.024 μm and the specific capacity area will be approximately 100 Cm^{-2}.

For the negative plate with a discharge capacity of 150 $Ahkg^{-1}$ Pb, we adequately assume an inner surface BET of 0.5 m^2g^{-1}. This will give a layer thickness of 0.27 μm, and will give a specific area capacity of approximately 1100 Cm^{-2}.

Experimentally derived specific area values range from 3 to $7 \times 10^3 Cm^{-3}$ (geometrical surface) for smooth lead electrodes discharged at small discharge rates and

room temperatures [Koch 59]. If we estimate a surface roughness of approximately 3 to 6, we arrive at corresponding theoretically derived values for typical porous electrodes of 5×10^2 to 1×10^4 Cm^{-2}.

The assumption of uniform coverage of the inner surface with lead sulphate is a gross simplification . In fact, the Pb^{2+} ions formed during discharge on both the PbO_2 and Pb electrodes first produces an oversaturated solution in the absence of crystal nuclei. The discharge starts preferentially at the peaks of the rough electrode surface, especially at the tips of dendrites, because this current density is larger than in the deeper points [de Levie 67a]. In the region of the valleys, seed formation starts and crystal deposit begins.

Spontaneous crystal formation occurs when the oversaturation is high but the material transport controls the crystal growth. Small crystals are formed at high current and acid densities and low temperatures. Conversely, large crystals are formed at low current and acid densities If crystal seeds are present as in slightly discharged positive electrodes or negative plates (due to their barium sulphate content), only very slight or no oversaturation occurs.

In a porous electrode with a pore diameter $< 5\mu$m , mass transport occurs over short distances. This value is well below the dimension of the Nernst diffusion layer, which is estimated to be about 500μm in an unstirred solution without convection. Generally, crystals are formed at the interface where lead ions are produced by the current. The crystals grow slowly at low current density into compact crystals with planes of low indices (*hkl* values). At high current densities, skeleton shaped and needle like crystal groups appear because of the accelerated formation of lead ions in non-equilibrated crystallisation from somewhat higher oversaturation.

Microscopic studies of negative plates show that at the beginning of the discharge the sulphate coverage follows the contours of the lead needles [Simon *et al* 70].

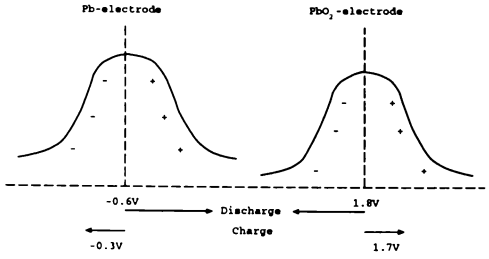

Figure 1.5: Inversion of the double layer during a change of the electrode potential

Later, compact lead sulphate crystals are formed. In this kind of discharge, parts of the plate are isolated and covered by $PbSO_4$ and can no longer be discharged.

It has been postulated that this is the reason why the discharge capacity of negative plates is never constant if a change is made from high to low current densities during a discontinuous discharge. In positive plates this coverage is not so severe because the inner surface is several times larger.

Differences of positive and negative plates structures are summarised in table (1.1). There are also differences on the phase boundary between the electrode and electrolyte. The double layer of storage battery plates are often called Helmholtz condensers with a fixed boundary [Bode 77]. At the surfaces the water dipoles have an orientation which is dependent on the charge. Oppositely charged ions are also adsorbed. During charging the potential changes sufficiently to permit a charge reversal of the double layer. A voltage range then exists in which there is no charged double layer. Only the oriented dipole molecules remain. The potential of this charge-free double layer (potential of zero charge) corresponds to the maximum of the electrocapillary curves, or Lippmann-potential, as shown in figure 1.6.

The point of zero charge occurs at +1.7 V in a PbO_2 electrode in 4M H_2SO_4 and at -0.6V in a Pb electrode when referenced to a standard hydrogen electrode.

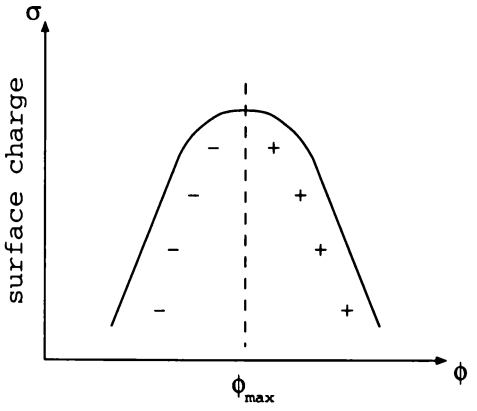

Figure 1.6: Interfacial tension σ as a function of applied potential

Characteristic Structure of Plates	Positive Plates	Negative Plates
Inner surface	Large	Small
Void volume	Macro/Microporosity	Macroporosity
Average pore diameter	Small	Large
Idealised thickness of the $PbSO_4$ layer after deep discharge	0.03μm	0.3μm
Electrode works above/below the potential of zero charge	Below	Above
Sign of the charge of the electrode:		
during disharge	Negative	Positive
during the first stage of charge	Negative	Positive
at the end of charge and overcharge	Positive	Negative
Specific adsorption	Cations	Anions

Table 1.1: Structural characteristics of the lead-acid plates [Bode 77]

1.8 Models of Lead-Acid Batteries

"Modeling phenomena is as much of a cornerstone of 20th century science as is collection of empirical data" [Jam 74]. In practically all fields of science, mathematical models of the real world become tested by fitting some parameters to empirical data.

The traditional approach for developing new batteries consists of experimental cell build-ups and an extensive testing regime. This is costly and very time consuming. Furthermore, and certainly more important from a scientific viewpoint, the results from such tests provide only global information and do not provide insight into the governing phenomena.

It is advantageous to develop mathematical models of such cells so that one may gain a better understanding of the cause and effect relationships of the phenomena involved, and suggest directions for improvements.

Complementing experimental testing with mathematical modeling is a cost effective approach to the development and design of batteries. Experimental data are still needed to verify the predictions of models and to identify any significant physical phenomena that may not have been included. But with the help of this mathematical tool, extensive experimental testing will no longer be needed. Great savings in material, labour and time can be realised in the development of a new battery system.

1.8.1 Empirical Models

Almost all discharge data of lead-acid batteries are related to discharge duration purely by Peukert's empirical equation,

$$I^n t = C \tag{1.17}$$

where I represents the current, t is time, and n and C are constants determined from experimental data. Peukert's equation is valid only as an interpolation formula in

the range of $n \approx 1.3 \rightarrow 1.4$ for intermediate currents. Basically it states that the capacity of cells and batteries drops non-linearly as the discharge current increases.

A more comprehensive empirical equation was developed by Shepherd [Shep 65] taking into account the usage of active material. Shepherd's equations correctly describe discharge curves for many batteries over a range of current densities. His polarisation coefficient and electrical internal resistance, however, have no physical significance. They are simply lumped parameters for the two electrodes and are correlated to experimental data.

1.8.2 Resistance Network Models

Ohmic losses in the current-collecting grids of electrodes, as shown in figure 1.7, reduce the performance of a lead-acid battery during high rates of discharge. Information of the potential distribution over a grid can be applied to the design of grids in order to minimise such losses.

Tiedemann and Newman [Tied 77] summarised the prior work on ohmic losses in lead grids and developed a model to solve Kirchoff's law at each node of the bare lead-acid battery grid. The potential distribution on the grid was examined by assuming a uniform current density. This model predicted the potential distribution on an unpasted battery grid with uniform current density across the face of the grid. They attained reasonable agreement with experimental data.

Tiedemann and Newman [Tied *et al* 79a] then expanded their earlier model to examine the transient behaviour of a lead-acid cell. Cell polarisation between the positive and negative electrodes was expressed by using an empirical equation whose coefficients were determined based on the porous electrode model developed by Tiedemann and Newman [Tied *et al* 79b].

Sunu and Burrows [Sunu *et al* 82] extended Tiedemann's resistance model to include the conductivity of active material in the pasted grid. Good agreement was found between the predicted potential distribution and experimental data. Sunu

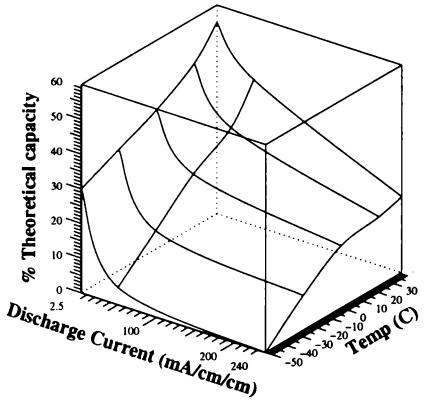

Figure 1.7: Current collecting grids of a typical lead-acid battery electrode

and Burrows [Sunu *et al* 84] expanded this model to account for nonuniform current density distribution. Excellent agreement was found between data and predicted potential distribution. With this model they could: (a) describe physical changes occurring during discharge; (b) quantify interactions between grid design, grid weight; and (c) determine cell performance, and optimise grid designs. Purely resistive models like these can not, however, predict the effects of concentration and porosity. Nishiki *et al* [Nish *et al* 86] developed a simple two-dimensional finite element model of a simple cell configuration for current distribution. They showed that even for simple geometries, nonuniformities in the current and potential distributions will occur due to ohmic drop. This corroborated the two-dimensional current-collector grid models of Sunu and Burrows [Sunu *et al* 82], [Sunu *et al* 84].

1.8.3 Porous Electrochemical Models

The first use of a mathematical model to describe the behaviour of the lead-acid battery was applied to the porous positive electrode by Stein [Stein 58]. Euler &

Nonenmacher [Euler 60] developed a steady-state one-dimensional macroscopic theory. They showed that for linear polarisation and uniform concentration, the current tends to pass from one phase to the other preferentially near the electrolyte-electrode interface or the metal backing interface depending, on the relative conductivities of the two phases. Newman & Nonenmacher [Newman *et al* 62] built upon Euler's [Euler 60] general equations and showed linearised kinetics leads to an inadequate description of the actual electrode when the reaction is distributed non-uniformly in the depth of the electrode. They demonstrated that the polarisation equation and the mass transport of the reacting species both play a major role in electrode performance.

Dunning & Newman [Dun *et al* 71] were the first to attempt to predict overpotential as a function of time in a single battery electrode. The authors used a Butler-Volmer type polarisation equation combined with a mass transport of an active species given by an empirically derived mass transfer coefficient. Time dependent phenomena were handled by assuming that the mass transfer coefficient was a function of the amount of active material present in any part of the electrode. They predicted cell failure caused by an internal mass transfer limitation with a sparingly soluble reactant. Their model was unable to predict cell failure by pore blockage.

Gidaspow & Baker [Gid *et al* 73] developed a porous electrode model to describe the transformation of one solid phase into another. Their model predicted cell failure due to the pores plugging by $PbSO_4$ deposition. However, they used a linear polarisation equation which is valid only at low current densities.

Simonsson [Sim 73], and Micka and Roušar [Micka *et al* 73], [Micka *et al* 74], [Micka *et al* 76] used a macro-homogeneous model to disregard the actual geometric detail of the pores and describe the porous electrodes as a superposition of the two continuous phases, liquid and solid. Simonson predicted that a reaction layer moves inward into the lead dioxide electrode due to gradual insulation of the surface by

converting lead sulphate crystals. Micka and Roušar modeled a positive PbO_2 electrode [Micka *et al* 73] and a negative Pb electrode [Micka *et al* 74] separately, and afterwards combined the equations to model a complete cell [Micka *et al* 76]. They predicted that for normal temperatures and discharge rates the discharge capacity of the cell is positive plate limited.

Tiedeman & Newman [Tied *et al* 79b] provided a detailed, one-dimensional mathematical model to simulate the discharge behaviour of a complete lead-acid cell. Sunu [Sunu 84] developed a similar one-dimensional model and took account of a nonuniform concentration in the electrolyte reservoir which the Tiedeman & Newman did not include. Gu *et al* [Gu 87] developed this type of one-dimensional model to include the simulation of charge and rest behaviour. These models allow the determination of pertinent system parameters over an entire discharge/recharge cycle. For example, the effect of thickness and porosity of the electrodes and the separator can be evaluated, and the profile of concentration of acid electrolyte throughout the depth of the whole cell can be predicted. One-dimensional models cannot, however, detail nonuniformities along the cell height. During discharge, the current density increases non-linearly towards the top of the cell. This leads to inefficient material utilisation and limits cell performance.

The development of two-dimensional lead-acid cell models, capable of detailing information along the cell height, as well as the cell width, is a natural progression. A two-dimensional model is capable of describing the experimentally observed acid density gradient that can develop in the electrolyte in a rapid discharge or slow charge. The acid density gradient is commonly called electrolyte stratification and influences the active material utilisation, and hence the capacity attainable in such a cell.

Dimpault-Darcy *et al* [Dimp 88] solved the porous electrode equations for a single PbO_2 electrode in two dimensions using the finite difference method. In their

model, the constraint that the current density be uniform at the face of the electrode resulted in insignificant variations along the electrode height.

Mao *et al* [Mao 91] analysed the potential and current distributions in a sealed lead-acid HORIZON® cell using a two-dimensional steady-state model. They used an IMSL finite element package which allowed them to analyse curved boundaries. Their model showed that the active material utilisation and electrode rechargeability are strongly influenced by electrode design.

Alavyoon *et al* [Alav *et al* 91] investigated the effects of acid density induced free convection and stratification on electrolyte composition in lead-acid cells. They dealt with equations in two dimensions for electrolyte velocity and composition but did not consider equations including voltage characteristics. They assumed for simplicity that the current density and electrode porosity were distributed uniformly in both spatial dimensions, and dilute solution theory was used to describe mass transport. The results predicted by the model agreed well with experimental data, both for the velocity and for the concentration fields.

Bernardi *et al* [Bern *et al* 93] expanded the Dimpault-Darcy two-dimensional PbO_2 electrode model to a complete cell using a finite difference method to solve the coupled non-linear equations. They assumed that the effects of free convection are ignorable for low rate discharges, and concentrated on voltage characteristics and distributions of current density, porosity, reaction rate, and active-material utilisation, as well as electrolyte composition. Electrolyte transport was described by concentration solution theory. The model predicted significant variations along cell height even at relatively low rates of discharge.

Recently Gu *et al* [Gu 97] developed a macrohomogeneous model which incorporated a combination concentrated/dilute solution theory in one and two dimensions. It not only included the coupled processes of electrochemical kinetics and mass

transport, but also accounted for free convection. Convection can become significant for low current density discharge/recharges, and causes acid stratification in the battery. Gu *et al* also utilised finite difference methods, this time, however, utilising fluid dynamics techniques instead of those previously used, which have basically been derivatives of Newman's techniques [Newman 75]. They achieved consistent results with previously published articles, whilst reducing solution times.

1.8.4 Thermal Models

Choi and Yao developed two-dimensional thermal models for the lead-acid batteries to aid in the design for load-leveling [Choi 78] and electric-vehicle propulsion [Choi 79] applications. These models were used to determine temperature profiles to design an optimum electrolyte circulation process for efficient heat removal in a battery system. They determined that electrolyte circulation would be an effective means for regulating the heat generated in charging.

1.9 Scope of the Thesis

The purpose of this thesis is several fold: Initially it was to develop reliable one and two dimensional mathematical models for a flooded porous lead-acid battery. Existing mathematical models utilised finite difference methods and matched the boundary conditions of each region to the opposing neighbouring region. Each region possesses its own set of governing equations. Formulations of this kind often lead to long solution times, especially for non-linear partial differential equations. These methods do not practically scale up to full three dimensional models; both the solution times and the rather awkward boundary conditions severely limit their applicability. Also, the existing models are essentially limited to rectangular regions, resulting in idealised geometry for the battery model.

For the above reasons, the method for numerical solution technique was the finite element method. The principle aim was the investigation of applicability of the

method to Newman's macrohomogeneous equations for concentrated solution flooded porous electrodes. If the boundary conditions can be incorporated naturally into the variational formulation for the system, then not only could the mathematical and numerical models be simplified, but also the solution times would be considerably shorter.

The purpose of the finite element models is to analyse the potential field, current distribution, mass transfer, porosity change, and concentration of electrolyte of lead-acid cells. The equations modeled are not only applicable to lead-acid cells, but to other electrochemical cells of a similar nature.

Because finite element techniques haven't previously been applied to a fully coupled set of electrochemical equations, considerable work has been undertaken on their applicability. The approach taken in this regard has been in a more engineering form than mathematical form. The principles are applied using intuition, physical reasoning and numerical experimentation applied to the problems reflecting the practice. The emphasis is not on mathematical rigor, exactly formulated definitions and assumptions, but rather that it works for practical examples and engineering practice. Final validation in this approach is that the results agree with results from other methods of solution, namely finite difference methods. Good agreement to date has been found.

On the other hand if the approach taken was mathematical, the work would have emphasised mathematical rigor, with exactly formulated definitions and assumptions. It would be essential for the work to be completely "clean", whether it works in all cases characterised by the assumptions made, etc.

The finite difference method has been used extensively to model electrochemical cells, and has a record of proven success. However the finite element method is naturally suited to complicated geometry; general boundary conditions and variable

or non-linear material properties can be handled with relative ease. In all these cases one meets unnecessary artificial complications with finite difference methodology.

More recently, especially in the field of computational fluid dynamics the finite volume method (or otherwise known as the cell-centred finite difference method) has been developed to encompass more complicated regions. However, it is found that the crude finite difference approximations of the integrands limit the effectiveness of finite volumes to relatively simple mesh structures and simple treatments of boundary conditions [Zienkiewicz 89].

The clear structure and versatility of the finite element method makes it possible to construct general purpose software for applications. The trial and test functions defined on the discretised domain provide accurate and robust approximations to the unknowns. However, the mathematical generality of the finite element method can be a weakness as well as strength: the computational overhead required to set up the finite element matrix system of equations can be expensive compared to the set up costs of finite volumes on general computational meshes. Furthermore, this overhead is relatively fixed: the set up costs for finite elements is largely problem independent for a general mesh. Relatively simple physical problems require as much work as complex physical phenomena. It is this computational overhead that has lead to two camps in computational fluid dynamics, and finite difference based methods are still widely used in this field. Essentially, there is no clear cut winner, each method has certain advantages over the other.

To the author's knowledge, this is the first time the finite element method has been applied to the transport equations of electrochemical cells in such a fundamental way. It is anticipated that the numerical techniques established for this work will stimulate future work in this field and allow for the interface with Computer

Aided Design (CAD) packages for commercial applications in electrochemical simulations, much the same as has happened in the field of structural and fluid dynamic engineering.

CHAPTER 2
POROUS ELECTRODE THEORY

2.1 Macroscopic Description of Porous Electrodes

2.1.1 Discussion

A "porous electrode" can range from a single reactive electronic conductor to mixtures of solids, including non-conducting reactive materials in addition to electronic conductors. An electrolytic solution penetrates the void spaces of the porous matrix. At any given time, there may be a large range of reaction rates within the pores. The distribution of these rates are dependent on: (a) the physical structure of the matrix; (b) the conductivities of the matrix and of the electrolyte; and (c) various parameters of the electrode which characterise the processes themselves.

Due to the intricacies of the system it is necessary to develop a model which describes the important features of a real electrode without taking into account the actual geometry of the pores. Additionally, the model's parameters should be readily obtainable experimentally. Typically, a porous media can be represented by its porosity averaged over a unit volume, average surface area per unit volume, and a volume-average resistivity to describe the electrolytic phase in the voids, etc. The volume averages taken of various variables should be small with respect to the overall dimensions but large compared to the pore structure as shown in figure 2.1. In such a model, rates of reactions and double-layer charging in the pores will have to be defined in terms of transferred current per unit volume.

A number of early models represent the structure with straight pores, perpendicular to the external face of the electrode, and a one-dimensional approximation is introduced and justified on the basis of the small diameter of the pore compared to

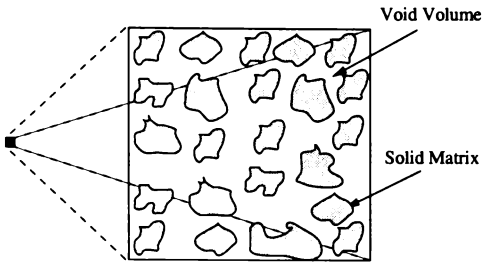

Figure 2.1: Volume element for macroscopic model

its length. de Levie [de Levie 67b] pointed out that the mathematical equations are basically equivalent to those of the macroscopic model although certain parameters such as the diffusion coefficient have different interpretations.

2.1.2 Averaged Quantities

The macrohomogeneous model is an extension of the concepts of conventional electrochemical systems, specifically, those of transport phenomena in electrolytic solutions and of the kinetics of electrode reactions. The actual geometry of the pore is ignored; instead a volume element inside the electrode is averaged. We can now define two potentials: ϕ_{soln}, the potential of the electrolyte in the pores; and ϕ_{solid}, the potential in the conducting matrix solid. Similarly, the current density can be defined in terms of the pore filling electrolyte current i_{soln}, and the solid matrix current i_{solid}. These current densities are referred to the projected volume of the electrode, rather than the volumes of the individual phases. Essentially, the electrode is now a superposition of the two continua. The quantities are assumed to be continuous functions of time and space.

The porosity, ϵ, is the void volume fraction within the element, and is filled with electrolyte. The volume element can also contain volumes of several solid phases which may be present. c_i is the solution-phase concentration of species i, averaged over the pores. Thus the superficial concentration averaged over the volume of both matrix and pores is ϵc_i.

The specific electro-interactive interfacial area a represents the surface area of the pore walls per unit volume of the electrode. Also, j_{in} represents the pore-wall flux of species i averaged over the same interfacial area. The pore-wall flux to be averaged is the normal component of the flux of species i at the pore wall, relative to the velocity of the pore wall, and in the direction pointing into the solution. The pore wall may be moving slightly due to a dissolution process. Thus aj_{in} represents the rate of transfer of the species from the solid phases to the pore solution (per unit volume of the total electrode).

Let $\mathbf{N}_i$ be the average flux of species i in the pore solution when averaged over the cross-sectional area of the electrode. Thus, for a plane surface of normal unit vector $\mathbf{n}$ cutting the porous solid, $\mathbf{n} \cdot \mathbf{N}_i$ represents the amount of species i crossing this plane in the solution phase, but is referred to the projected area of the whole plane rather than to the area of an individual phase.

The fluxes of charged species, when appropriately summed, yield a charge balance equation for the superficial current density $\mathbf{i}_{soln}$, i.e.

$$\mathbf{i}_{soln} = F \sum_i z_i \mathbf{N}_i \tag{2.1}$$

Here F is the Faraday constant and z_i is the valence number of species i; hence $z_i \mathbf{N}_i$ represents the charge per mole.

Similarly, the current density $\mathbf{i}_{solid}$ in the matrix phase is defined to refer to the superficial area and not to the area of an individual phase.

2.1.3 Electroneutrality

If the electric force in a volume element (within the porous electrode) cannot create a significant separation of charge over an appreciable distance then it can be said to be electrically neutral. The electroneutrality condition for the solution phase is thus:

$$\sum_i z_i c_i = 0 \tag{2.2}$$

where c_i is the concentration of species i in moles/cm^3, and z_i is the charge number of ionic species i.

Thus the interfacial region which comprises the electric double layer (where the electroneutrality condition breaks down) constitutes only a small volume compared to any of the phases or the electrode itself. This assumption fails for finely porous media and very dilute solutions, where the diffuse layer may be more than 100 $\mathring{A}$ thick. Electro-kinetic effects such as electro-osmosis and the streaming potential are also ignored.

The concentration, c_i, of ionic species i is defined by:

$$c_i = \nu_i c \tag{2.3}$$

where c is the concentration of neutral electrolyte in moles/cm^3, and ν_i is the number of ionic species i per electrolyte molecule,

We can now express the electroneutrality condition for sulphuric acid. H_2SO_4 can be considered to be a binary electrolyte containing a cation (species +), an anion (species −), and water (species o), whence

$$z_+\nu_+ + z_-\nu_- = 0 \tag{2.4}$$

A single electrode reaction can be represented as

$$\sum_i s_i M_i^{z_i} \rightarrow ne^- \tag{2.5}$$

where $M_i^{z_i}$ is the symbol representing the species i, s_i is the stoichiometric coefficient of species i, n is the number of electrons e transferred by the electrode reaction, and $1, 2, o$, and e^- represent the cation, anion, water, and electron respectively.

Faraday's Law for the above single electrode reaction in the absence of double layer charging is:

$$aj_{in} = -\frac{as_i}{nF} i_n = -\frac{s_i}{nF} \nabla \cdot \mathbf{i}_{soln} \tag{2.6}$$

where a is the specific interfacial area, j_{in} is the pore wall flux of species i, and $\mathbf{i}_{soln}$ is the superficial current density in the pore phase.

From the assumption of electroneutrality it can be stated that the divergence of the total current density is zero, i.e.

$$\nabla \cdot \mathbf{i}_{solid} + \nabla \cdot \mathbf{i}_{soln} = 0 \tag{2.7}$$

Restated, current which leaves the matrix phases enters the pore solution.

2.1.4 Material Balance of Electrolyte Species

Within a pore, in the absence of homogeneous chemical reactions, a differential material balance can be written for a species i. This equation can be integrated over the volume of the pores in an element of the electrode, and surface integrals can be introduced by means of the divergence theorem. Careful use of the definitions of average quantities yields [Dun 71] the material balance for species i:

$$\underset{\text{Accumulation}}{\frac{\partial \epsilon c_i}{\partial t}} = \underset{\text{Production}}{a j_{in}} \quad \underset{\text{NetInput}}{- \nabla \cdot \mathbf{N}_i} \tag{2.8}$$

Here ϵ is the porosity of the matrix and a is the specific interfacial area. Three volume averages are represented in equation (2.8): c_i is an average over the volume of the solution in the pores; j_{in} is an average over the interfacial area between the matrix and the pore solution; and $\mathbf{N}_i$ is an average of the transport rate of species i per unit cross-sectional area through the electrode. Note again that the averages involve a volume which is large relative to the pore structure, but is sufficiently small relative to regions in which significant variations occur.

Equation (2.8) states that the concentration can change at a point within the porous electrode because the species moves away from the point or because the species is involved in electrode processes (Faradaic electrochemical reactions or double-layer charging) or simple dissolution of a solid material. This aj_{in} term is analogous to

the term which describes the bulk production of a species by homogeneous chemical reactions ([Newman 73], p 218). However, in the macroscopic model, the production term from the matrix phases occurs throughout the bulk of the electrode (due to the averaging process).

2.1.5 Concentrated Binary Electrolyte

As the lead-acid battery system has a single binary electrolyte, we can develop relatively simple equations using concentrated solution theory. This is aided with the fact that thermodynamic and transport data are readily available for the binary electrolyte, sulphuric acid.

The flux of species i can be defined as

$$\frac{N_i}{\nu_i} = \underbrace{-D_{eff}\nabla c}_{\text{Diffusion}} \quad \underbrace{+\frac{t_i}{z_i\nu_i F}\mathbf{i}_{soln}}_{\text{Migration}} \quad \underbrace{+c\mathbf{v}}_{\text{Convection}} \tag{2.9}$$

where the subscript i represents the ionic species $+$ or $-$, t_i the transference number of ionic species i, and $\mathbf{v}$ is the volume average velocity of the pore solution.

Similarly for water,

$$N_o = D_{eff}\nabla c + c\mathbf{v} \tag{2.10}$$

The effective diffusion coefficient D_{eff} is corrected for porosity and tortuosity by the Bruggeman-type ([Mer 62] relation:

$$D_{eff} = D\epsilon^{ex} \tag{2.11}$$

where ex is a correction for the tortuosity of the porosity of the solid matrix, and is generally 0.5 for a porous lead-acid electrode.

The volume average velocity $\mathbf{v}$ and the porosity ϵ in equations (2.8), (2.9) and (2.10) can be expressed explicitly in terms of the volume changes during electrode reaction. The electrode porosity varies during electrode reaction due to the volume

difference between solid products and reactants and can be written as:

$$\frac{\partial \epsilon}{\partial t} = \frac{1}{nF} \sum_{solid\ species,i} s_i \bar{V}_i \nabla \cdot \mathbf{i}_{soln} \tag{2.12}$$

where s_i is the stoichiometric coefficient of species i defined in equation (2.5) and $\bar{V}_i$ is the molar volume of species i. We now seek an expression for the convective velocity $\mathbf{v}$.

Rewriting equations (2.8), (2.9) and (2.10) for each of the species:

$$\frac{\partial \epsilon c_+}{\partial t} = -\nabla \cdot \left(-D_{eff} \frac{dc_+}{dx} + \frac{t_+}{z_+ F} - c_+ \mathbf{v} \right) - \frac{s_+}{nF} \nabla \cdot \mathbf{i}_{soln} \tag{2.13}$$

$$\frac{\partial \epsilon c_-}{\partial t} = -\nabla \cdot \left(-D_{eff} \frac{dc_-}{dx} + \frac{t_-}{z_- F} - c_- \mathbf{v} \right) - \frac{s_-}{nF} \nabla \cdot \mathbf{i}_{soln} \tag{2.14}$$

$$\frac{\partial \epsilon c_o}{\partial t} = -\nabla \cdot \left(-D_{eff} \frac{dc_i}{dx} - c_o \mathbf{v} \right) - \frac{s_i}{nF} \nabla \cdot \mathbf{i}_{soln} \tag{2.15}$$

Multiplying equations (2.13), (2.14) and (2.15) by $\bar{V}_+$, $\bar{V}_-$ and $\bar{V}_o$, respectively and summing the three resultant equations gives:

$$\frac{\partial \epsilon}{\partial t} + \nabla \cdot \mathbf{v} = -\frac{1}{nF} \left(s_+ \bar{V}_+ + s_- \bar{V}_- + s_o \bar{V}_o \right) \nabla \cdot \mathbf{i}_{soln} \tag{2.16}$$

Combining equations (2.12) and (2.16) leads to an expression for the volume average velocity:

$$\nabla \cdot \mathbf{v} = -\frac{1}{nF} \left(s_+ \bar{V}_+ + s_- \bar{V}_- + s_o \bar{V}_o + \sum_{solid\ species,i} s_i \bar{V}_i \right) \nabla \cdot \mathbf{i}_{soln} \tag{2.17}$$

which gives:

$$\mathbf{v} = -\frac{1}{nF} \left(s_+ \bar{V}_+ + s_- \bar{V}_- + s_o \bar{V}_o + \sum_{solid\ species,i} s_i \bar{V}_i \right) \mathbf{i}_{soln} \tag{2.18}$$

The material balance equation (2.8) can now be written as:

$$\epsilon \frac{\partial c}{\partial t} + \mathbf{v} \nabla c = \nabla \cdot (D_{eff} \nabla c) + \left(-\frac{s_-}{\nu_-} - \frac{n t_-}{z_- \nu_-} + c(s_+ \bar{V}_+ + s_- \bar{V}_- s_+ s_o \bar{V}_o) \right) \tag{2.19}$$

where

$$s_+ \bar{V}_+ + s_- \bar{V}_- = \frac{s_-}{\nu_-} - \frac{n t_-}{z_- \nu_- \bar{V}} \tag{2.20}$$

2.1.6 Electrode Kinetics

Electrode kinetics do not follow fundamental laws that can be written down as reliably as the law of conservation of matter. The overall kinetic behaviour of a porous electrode is a result of the mutual dependence of intrinsic kinetics, structural changes, current distribution and concentration changes. The porous structure is in itself of decisive importance for the electrode kinetics. Specific surface area and pore size distribution are important structural parameters. These parameters are not constant in the porous lead dioxide electrode because of the structural transformations that occur between the solid phases Pb, PbO_2 and $PbSO_4$.

As the phenomena are so complex, the polarisation equation is used to predict the behavior of a complex electrochemical system rather than to have to explain the mechanism of the electrode reaction itself. It expresses the dependence of the local rate of reaction on the various concentrations and on the potential jump at the matrix-solution interface.

The Butler-Volmer type polarisation equation can be written as

$$\nabla \cdot \mathbf{i}_{soln} = A_a i_0^o (\frac{c}{c_{ref}})^\gamma \left(e^{(\frac{\alpha_a F}{RT}\eta_s)} - e^{-(\frac{\alpha_c F}{RT}\eta_s)} \right) \tag{2.21}$$

where A_a is the electrochemically active interfacial area per unit electrode volume and is electrode specific, i_0^o is the exchange current density evaluated at the reference concentration c_{ref}, γ is the order of dependence of the exchange current density on the electrolyte concentration, α_a and α_c are anodic cathodic transfer coefficients determined from experimental data, and η_s is the local value of the surface overpotential. The surface overpotential can be defined as the potential difference of the working electrode relative to a reference electrode of the same kind positioned adjacent to it, just outside the double layer. η_s is equal to the potential difference $\phi_{solid} - \phi_{soln}$, plus an additive term depending on the local solution composition.

Ideally, the polarisation equation should not only account for the mechanism of the charge-transfer process but also for the morphology of the electrode, the formation of covering layers or of crystallites of sparingly soluble species, and the transport from such sparingly soluble phases to the site of the charge-transfer process. This is a principle limitation of the macroscopic theory to date.

2.1.7 Ohms Law in the Solid Matrix Phase

In the solid matrix (active material) phase the movement of electrons is governed by Ohm's law:

$$\mathbf{i}_{solid} = -\sigma_{eff} \nabla \phi_{solid} \tag{2.22}$$

where ϕ_{solid} is the potential of the solid matrix, $\mathbf{i}_{solid}$ is the superficial current density transferred through the solid active material, and σ_{eff} is the effective conductivity of the solid matrix being corrected for porosity and tortuosity by the Bruggeman-type ([Mer 62]) relation:

$$\sigma_{eff} = \sigma \epsilon^{ex} \tag{2.23}$$

Using equation (2.22) we can rewrite the divergence of current (2.7) as:

$$\nabla \cdot \mathbf{i}_{solid} - \nabla \cdot (\sigma_{eff} \nabla \phi_{solid}) = 0 \tag{2.24}$$

2.1.8 Ohms Law in the Pore Solution Phase

The potential loss in solution is governed by Ohm's law and may be written in the form [Newman 73]

$$\frac{\mathbf{i}_{soln}}{\kappa_{eff}} = -\nabla \phi_{soln} - \left(\frac{s_+}{\nu_+} + \frac{n t_+^0}{z_+ \nu_+} - \frac{s_0 c}{c_0} \right) \frac{\nabla \mu_e}{nF} \tag{2.25}$$

ϕ_{soln} is the potential in the pore solution measured with a reference electrode having the stoichiometric coefficients s_i and number n of the electrons transferred, μ_e is the chemical potential of the electrolyte in J/mole, and κ_{eff} is the effective conductivity

of the pore solution in mho/cm, and is corrected for porosity and tortuosity by the Bruggeman-type ([Mer 62]) relation:

$$\kappa_{eff} = \kappa\epsilon^{ex} \tag{2.26}$$

The chemical potential μ_e can be defined as [Newman 73]:

$$\mu_e = \nu RTln(c_i f_i a_i^{\theta}) \tag{2.27}$$

where c_i is the concentration of the species i expressed in molarity (moles/litre), f_i is mean molar activity coefficient if the species, and a_i^{θ} is a proportionality constant independent of composition and electrical state, but characteristic of the solute species and the solvent and dependent on temperature and pressure. The pressure dependence is minimal for the liquid phase, and often isothermal conditions are assumed.

Therefore,

$$\frac{\mathbf{i}_{soln}}{\kappa_{eff}} = -\nabla\phi_{soln} - \frac{\nu RT}{nF}\left(\frac{s_+}{\nu_+} + \frac{nt_+^0}{z_+\nu_+} - \frac{s_0 c}{c_0}\right)\nabla ln(cf_i) \tag{2.28}$$

2.1.9 Note for Species

For any arbitrary species i: + represents a cation H^+, − represents an anion HSO_4^-, and o represents the solvent water. Stoichiometric coefficients are:

Negative electrode reaction: $s_+ = -1$, $s_- = 1$, $n = 2$, $s_o = 0$, $s_{Pb} = 0$, and $s_{PbSO_4} = -1$;

Positive electrode reaction: $s_+ = 3$, $s_- = 1$, $n = -2$, $s_o = -2$, $s_{Pb} = 1$, and $s_{PbSO_4} = -1$;

z_i is the charge number of species i;

ν_{ij} is the number of ionic species i per mole of species j;

$\nu_+ = 1$, $\nu_- = 1$; and

$z_+ = 1$, $z_- =$ -1.

2.1.10 Electroneutrality and Conservation of Charge

It is a consequence of the assumption of electroneutrality that the divergence of the total current density is zero. For the macroscopic model, this is expressed as

$$\nabla \cdot \mathbf{i}_{solid} + \nabla \cdot \mathbf{i}_{soln} = 0 \tag{2.29}$$

Charge which leaves the matrix phases must enter the pore solution. In fact, a combination of equations (2.1), (2.9), and (2.2) gives

$$\nabla \cdot \mathbf{i}_{soln} = aF \sum_i z_i j_{in} = a i_n \tag{2.30}$$

where i_n is the average current density (from the matrix phase to the solution phase). $\nabla \cdot \mathbf{i}_{soln}$ is the transfer current per unit volume of the electrode (A/cm^3) and has the direction of the anodic current.

CHAPTER 3
THE FINITE ELEMENT METHOD

3.1 Introduction

This chapter introduces the finite element method (fem) as a general technique for the numerical solution of time dependent coupled non-linear partial differential equations. It is by no means a mathematically rigorous treatment of the fem. The emphasis is to build physically and numerically sound reasoning on the mathematical techniques in order for elements to be derived and computer programs to be written.

Firstly, the types of partial differential equations (pde) are classified, and as exact solutions can only be obtained for the most trivial examples, numerical procedures are detailed in order solve the pde. The techniques developed are categorised as finite element methods. The particular finite element method employed is a Mean Weighted Residual method.

The fundamentals of linear spaces are treated, and the Hilbert space is defined. This allows methods to be designed to discretise differential equations of certain forms that fit into the linear spaces that are defined. These methods characterise what is called the finite element method.

From here we are able to develop the mechanics of the finite element method, i.e. discretisation of the problem, shape functions, evaluation of the element matrices, the formulation of the global matrix, where, why and how the boundary conditions are applied, and how the resulting matrices are solved. Isoparametric elements are introduced along with numerical integration as a way of simplifying the process of forming the elemental matrices.

Finite element spaces are linear by their definition. Partial differential equations are often non-linear. The Newton-Raphson method is outlined in order to linearise the partial differential equations so that they are applicable to solution by finite element techniques.

Next, time stepping techniques are reviewed. The relative merits of implicit versus explicit methods are considered as well as their stability criteria.

The techniques used to solve large sparse matrices are not treated to any substantial degree as today it is possible to use "black box" software which allows one to solve the formulated matrix problem with complete confidence for general problem classes without having to understand the fine algorithmic details [Barret *et al* 1994].

3.1.1 Classification of Partial Differential Equations

A second order partial differential equation for two dimensions may be written as [Garcia 94]:

$$a\frac{\partial^2 A}{\partial x^2} + b\frac{\partial^2 A}{\partial x \partial y} + c\frac{\partial^2 A}{\partial y^2} + d\frac{\partial A}{\partial x} + e\frac{\partial A}{\partial y} + fA(x,y) + g = 0 \tag{3.1}$$

and is classified as hyperbolic if $b^2 - 4ac > 0$, parabolic if $b^2 - 4ac = 0$, and elliptic if $b^2 - 4ac < 0$. The general formulations can be extended to higher dimensions [Garcia 94].

The equations governing the electrochemical system of a Lead-Acid battery are a hybrid of the above three classifications.

Initial Value and Boundary Value Problems

Boundary value problems (bvp) require that we specify boundary conditions in order to solve the solution. Initial value problems (ivp) in addition to requiring boundary conditions, require an initial function distribution, say $\phi(x, 0)$, in order to seek a solution for $t > 0$.

We consider only the two main boundary conditions, Dirichlet and Neumann boundary conditions. For second order differential equations, the Neumann boundary conditions is specified as the flux at the boundary, and the Dirichlet boundary condition specifies the function at the boundary. For example, a parabolic differential equation of the form:

$$\frac{\partial \phi(x,t)}{\partial t} - \kappa \frac{\partial^2 \phi(x,t)}{\partial x^2} = 0 \text{ for } 0 < x < L \tag{3.2}$$

may possess the following Dirichlet boundary conditions:

$$\phi(0,t) = \phi_a; \quad \phi(a,t) = \phi_b \tag{3.3}$$

the following Neuman boundary conditions:

$$-\kappa \frac{\partial \phi(0,t))}{\partial x} = F_a; \quad -\kappa \frac{\partial \phi(a,t))}{\partial x} = F_b \tag{3.4}$$

and the following initial condition:

$$\phi(x,0) = f(x) \tag{3.5}$$

If the boundary conditions equal zero, e.g. $\phi(x,0) = 0)$, or $\frac{\partial \phi(0,t))}{\partial x} = 0$, then they are termed homogeneous. If the boundary conditions are not equal to zero, they are call non-homogeneous.

For a solution to exist it is required to be unique [White 85].

3.1.2 Solutions of Boundary Value Problems

Classical Solutions

If we find a solution $y(x,t)$ for a bvp, then we have a classical solution of the continuum problem if and only if, $\phi \in C^2[0,L]$ and equation 3.2 are satisfied. $C^2[0,L]$ is the set of functions on $[0,L]$ that have two continuous derivatives. Often classical solutions are unable to be found, and we approximate to the continuous solution by a discrete model, usually the finite difference method.

The Variational Formulation

We reformulate the given differential equation as an equivalent variational problem. This basically takes the form of a minimisation problem:

$$\text{For } u \in V \text{ such that } F(u) \leq F(v) \text{ for all } v \in V \tag{3.6}$$

where V is a given set of admissible functions and $F : V \rightarrow \mathcal{R}$ is a functional.

Often the exact solution cannot be solved and an approximation method such as the Rayleigh-Ritz method is used. This is called a Variational finite element method. A more general variational formulation to the minimisation problem is based on the weak formulation [Buchanan 95].

Weak Solutions

The weak formulation of a bvp can be obtained in the following manner:

Multiply the equation by a test function ψ. $\psi \in C^2[0, a]$, where $\psi(0) = 0 = \psi(L)$.

Integrate to obtain the resulting weak equation

The weak solution can be defined as:

1. ϕ has a piecewise-continuous derivative;
2. The weak equation, holds for all ψ that have piecewise-continuous derivative;
3. $\phi(0) = a$ and $\phi(L) = b$.

The Galerkin finite element solution is often used to derive algebraic equations which are used to solve for ϕ.

The adjective weak is used because the solution does not require two derivatives. Not all differential equations have classical solutions, and the energy and weak formulations have their respective merits depending on the problem at hand [Cuvelier 85].

The classical solution is a weak solution, and in fact if an energy solution exists, it and the weak solution are identical [White 85].

3.2 Finite Elements/Finite Differences

The numerical solution of partial differential equations is split up into two distinct disciplines, called respectively the finite difference method (fdm) and the finite element method (fem). Mathematically speaking, finite differences are a subset of finite elements [Zienkiewicz 89]. In the fdm, the differentials are replaced with difference quotients involving the values for the unknown at certain (finitely many) points. The discretisation process using a fem is different.

Systems of coupled partial differential equations of considerable complexity, such as those describing fluid flow, heat transfer, and electrochemical reactions are only accessible with numerical methods [Cuvelier 85]. Finite difference methods, but even more specifically finite volume methods (fvm) such as those described in [Prat 80], are very successful in this area. The robustness of the fvm discretisation schemes, employing just "Four Basic Rules", has no counterpart in finite element methodology [Cuvelier 85]. The main drawback of finite difference-like methods is well known, however. When attempting to get rid of inhomogeneous parts of the calculation domain, caused for example by curved boundaries, a considerable overhead is introduced, tending to make fdm/fvm methods unworkable. When employing a finite element method, curvilinear boundaries and topological complexity present no problem whatsoever. They are done in a uniform and natural fashion, in stark contrast to finite difference methodology. General boundary conditions and variable or non-linear material properties are also handled with relative ease. Further, the clear structure and versatility of the fem makes it possible to construct general purpose software for applications.

In order to formulate an fe discretisation scheme properly, something like a Variational or Galerkin principle has to be resorted to. When dealing with very complicated equations, especially those describing transport phenomena with many different high order derivatives, this can turn out to be a serious bottleneck [White 85].

3.3 Basic Definitions For Finite Elements

Consider a sequence of functions

$$\phi_1(x), \phi_2(x), \phi_3(x), ..., \phi_n(x) \tag{3.7}$$

The functions are assumed to satisfy certain given conditions, called admissibility conditions, relating to the boundary conditions and the degree of continuity.

If the elements can be linearly combined, for instance,

$$\phi = \alpha\phi_1 - \beta\phi_2 \tag{3.8}$$

where α and β are numbers, they are called elements of a linear space R, and the following properties apply:

$$\phi_1 + \phi_2 = \phi_2 + \phi_1 \tag{3.9}$$

$$(\alpha + \beta)\phi = \alpha\phi + \beta\phi$$

$$\alpha(\phi_1 + \phi_2) = \alpha\phi_1 + \alpha\phi_2$$

The inner product of two functions ϕ_1 and ϕ_2 is denoted by

$$< \phi_1, \phi_2 > \tag{3.10}$$

and it represents an operation on ϕ_1 and ϕ_2, such as

$$< \phi_1, \phi_2 >= \int_{x_1}^{x_2} \phi_1(x)\phi_2(x)dx \tag{3.11}$$

or

$$< \phi_1, \phi_2 >_c= \int_0^t \phi_1(t-\tau)\phi_2(\tau)d\tau \tag{3.12}$$

The second definition is called the convolution and will not be considered further.

For real functions, the inner product has the following properties:

$$\begin{aligned} < \phi_1, \phi_2 > &= < \phi_2, \phi_1 > \\ \alpha < \phi_1, \phi_2 > &= < \alpha\phi_1, \phi_2 > \\ < \phi_1, \phi_2 + \phi_3 > &= < \phi_1, \phi_2 > + < \phi_1, \phi_3 > \\ < \phi_1, \phi_1 > &> 0 \text{ if } \phi_1 \neq 0 \\ &= 0 \text{ if } \phi_1 = 0 \end{aligned} \tag{3.13}$$

where $\phi_1 = 0$ is a "null" function which exists in the space R.

A measure (norm) of the function ϕ can be taken as the square root of the inner product of ϕ by itself and is denoted by $\| \phi \|$.

$$\| \phi \| = \sqrt{< \phi, \phi >} \tag{3.14}$$

A sequence of functions such as (3.7) is said to be linearly independent if

$$\alpha_1\phi_1 + \alpha_2\phi_2 + \alpha_3\phi_3 + ... + \alpha_n\phi_n = 0 \tag{3.15}$$

only when all α_i are zero.

A sequence of linearly independent functions is said to be complete if a number N and a set of constants α_i can be found such that, given an arbitrary allowable function u, we have

$$\| u - \sum_{i=1}^{N} \alpha_i\phi_i \| < \epsilon \tag{3.16}$$

where ϵ is any small positive quantity.

The functions ϕ_i are called basis functions and the coefficients α_i are the Fourier coefficients.

If the normalised basis functions are mutually orthogonal,

$$\begin{aligned} < \phi_i, \phi_j > &= 0 \text{ if } i \neq j \\ < \phi_i, \phi_i > &= 1 \end{aligned} \tag{3.17}$$

Each additional term we take in the linearly independent and complete sequence ϕ_i will introduce a further α_i. For the Nth approximation, we have

$$u^{(N)} = \sum_{1}^{N} \alpha_i \phi_i \tag{3.18}$$

Thus

$$\| u^{(N)} \| \rightarrow \| u \| \quad \text{as } N \rightarrow \infty \tag{3.19}$$

The norm of $u^{(N)}$ for a mutually orthogonal complete sequence (if the sequence is not orthogonal we will accept that we can always reduce it to an orthogonal one) is

$$\begin{aligned} \| u^{(N)} \| &= \sqrt{\left\{ \left\langle \sum_{i=1}^{N} \alpha_i \phi_i, \sum_{j=1}^{N} \alpha_j \phi_j \right\rangle \right\}} \\ &= \sqrt{\left\{ \sum_{i=1}^{N} \sum_{i=1}^{N} \alpha_i \alpha_j < \phi_i \phi_j > \right\}} \end{aligned} \tag{3.20}$$

and since $< \phi_i, \phi_j >= 0$ if $i \neq j$, we have

$$\| u^{(N)} \| = \sqrt{\left\{ \sum_{i=1}^{N} \alpha_i^2 < \phi_i, \phi_i > \right\}} \tag{3.21}$$

Each term in the summation is positive, thus $\| u^{(N)} \|$ approaches $\| u \|$ from below as N increases.

$$\| u^{(N)} \| \leq \| u^{(M)} \| \leq \| u \| \quad \text{with } N < M \tag{3.22}$$

A linear operator $\mathcal{L}( )$ is defined as a process which, when applied to a given function u, produces another function p:

$$\mathcal{L}(u) = p \tag{3.23}$$

An operator is linear if

$$\mathcal{L}(\alpha u_1 + \beta u_2) = \alpha \mathcal{L}(u_1) + \beta \mathcal{L}(u_2) \tag{3.24}$$

This definition is general but we will consider here only differential operators.

Properties analogous to symmetry and positive definiteness for a matrix can also be defined for an operator. Consider a square matrix, $\mathbf{a} = [a_{ij}]$. We say $\mathbf{a}$ is symmetrical when $\mathbf{a}^T = \mathbf{a}$, where $\mathbf{a}^T$ is the transpose of $\mathbf{a}$. Symmetry requires $a_{ij} \equiv a_{ji}$. Another way of defining symmetry is to require

$$< \mathbf{y}, \mathbf{ax} > \equiv < \mathbf{x}, \mathbf{ay} > \tag{3.25}$$

for arbitrary vectors $\mathbf{x}$ and $\mathbf{y}$. Expanding (3.25) and noting that $(\mathbf{bc})^T = \mathbf{c}^T\mathbf{b}^T$,

$$< \mathbf{y}, \mathbf{ax} > = \mathbf{y}^T\mathbf{ax} \tag{3.26}$$

$$< \mathbf{x}, \mathbf{ay} > = \mathbf{x}^T\mathbf{ay} = \mathbf{y}^T\mathbf{a}^T\mathbf{x} \tag{3.27}$$

shows that (3.25) is equivalent to $\mathbf{a}^T = \mathbf{a}$. The latter definition is more convenient for extension to operators. Positive definiteness is defined by

$$< \mathbf{x}, \mathbf{ax} > \geq 0 \tag{3.28}$$

for all $\mathbf{a}$ and equals 0 only when $\mathbf{x}$ is a null vector. This property is extremely valuable in establishing solution schemes.

3.3.1 Hilbert Space

A Hilbert space (V) has the following properties. It is a linear space; It possesses a scalar product with a corresponding norm $\| \cdot \|$; and it is complete (i.e. every Cauchy sequence with respect to $\| \cdot \|$ is convergent). Simply put, a Hilbert space is a linear space with a scalar product.

We can define a Hilbert space, $L_2(I)$ of square integrable functions.

$$L_2(I) = \{v : v \text{ is defined on } I \text{ and } \int_I v^2 dV < \infty\} \tag{3.29}$$

There exists another Hilbert space $H^1(I)$, which, together with their first derivatives, are square-integrable, i.e., belong to $L_2(I)$.

$$H^1(I) = \{v : \ v \text{ and } v' \text{ belong to } L_2(I)\} \tag{3.30}$$

For boundary value problems with boundary conditions $u(a) = u(b) = 0$ the space $H_0^1(I)$ can be defined, i.e.

$$H_0^1(I) = \{v \in H^1(I) : v(a) = v(b) = 0\} \tag{3.31}$$

with the same scalar product and norm as for $H^1(I)$.

3.4 The Methods of Weighted Residuals

The methods of weighted residuals (mwr) are a numerical procedures that can be used to solve a single or set of partial equations of the form:

$$\mathcal{L}(u) = p; \quad x \in \Omega \tag{3.32}$$

with two prevalent boundary conditions,

$$\text{essential (Dirichlet)} \quad G(u_0) = g; \quad \text{on } \Gamma_{u_0} \tag{3.33}$$

where the value of the variable is prescribed, and

$$\text{natural (Neumann)} \quad S(u) = q; \quad \text{on } \Gamma_q \tag{3.34}$$

where u is the exact solution, Ω is the domain, and Γ is the external surface of the continuum. The function u is approximated by a set of functions ϕ_k:

$$u = \sum_{k=1}^{N} \alpha_k \phi_k \tag{3.35}$$

where α_k are undetermined parameters and ϕ_k are linearly independent functions taken from a complete sequence.

Initially we require that these functions satisfy all the boundary conditions of the problem (3.33) and have the necessary degree of continuity as to make the

left hand side of (3.32) different from zero. Substituting equation (3.35) into (3.32) produces an error function ϵ, which is called the residual:

$$\epsilon = \mathcal{L}(u) - p \neq 0 \tag{3.36}$$

where ϵ equals zero for the exact solution. This error is forced to be zero, in an average sense, by setting the weighted integral of the residual equal to zero:

$$< \epsilon, w_i > = 0, \quad i = 1, 2, ..., N \tag{3.37}$$

where w_i is a set of weighting functions.

Application of the mwr produces a set of algebraic equations. There are several types of mwr criteria, the most popular being: the collocation method; the least-square method; the method of moments; and Galerkin's method. Each will produce a different set of values, resulting in many different approximate solutions. Depending on the method chosen, the different solutions may all be close to each other and to the exact solution.

The method chosen is the most commonly employed, called the Galerkin method, due to its ease of applicability. It will be discussed next.

3.4.1 Galerkin's Method

In the Galerkin method the weighting functions are the same trial functions. Consider the equation

$$\mathcal{L}(u) - p = 0 \tag{3.38}$$

and an approximating function

$$u = \sum_{k=1}^{N} \alpha_k \phi_k \tag{3.39}$$

which satisfies the boundary conditions $S(u) = q(\Gamma)$. The residual

$$\epsilon = \mathcal{L}\left(\sum \alpha_k \phi_k\right) - p \tag{3.40}$$

is orthogonal with respect to the trial functions ϕ_i:

$$< \epsilon, \phi_i > = 0 \tag{3.41}$$

which leads to:

$$\int \left\{ \mathcal{L}\left(\sum \alpha_k \phi_k\right) - p \right\} \phi_i d\Omega = 0 \quad i = 1, 2, ..., N \tag{3.42}$$

If $\mathcal{L}$ is a linear operator, (3.42) produces a system of linear equations from which the α_k coefficients can be obtained.

Contrary to other weighted residual methods in which the error is orthogonalised with respect to a set of functions different from the trial functions, in the Galerkin procedure the weighting functions are the same as the trial ones.

3.5 Weak Formulations

For simplicity we have only considered, up until now, self-adjoint operators and essential boundary conditions. However, weighted residual methods are applicable for arbitrary operators and boundary conditions. We will now treat a general procedure for formulating weighted residual statements which allows only partial satisfaction of the boundary conditions, and, of more significance, the use of basis functions having relaxed continuity requirements.

We introduce a classification for the degree of continuity of a function. Consider a function $u(x)$ defined over a region Γ and having a shape as in Figure 3.1. The function is discontinuous at discrete points but is finite throughout the region. Its norm satisfies:

$$\| u \|_0 = \int_V u^2 d\Omega < \infty \tag{3.43}$$

All functions satisfying (3.43), i.e. those that are square integratable, are said to belong to the L_2 function space.

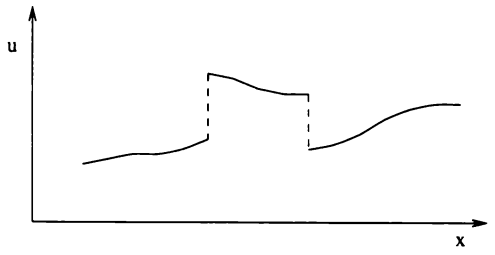

Figure 3.1: Discrete functions

Imposing restrictions on the continuity of the derivatives leads to a subset of spaces, called Sobolov spaces. The space $W_2^{(1)}$ (the superscript refers to the highest finite derivative, the subscript refers to the square norm measure) contains all functions whose first derivative is square integrable. Its definition equation is (in one dimension)

$$\| u \|_1 = \int \left(u^2 + \left(\frac{du}{dx} \right)^2 \right) dx < \infty \tag{3.44}$$

Higher-order spaces are defined in an analogous way. For example, the $W_2^{(2)}$ space contains all functions which satisfy

$$\| u \|_1 = \int \left(u^2 + \left(\frac{du}{dx} \right)^2 + \left(\frac{du^2}{dx^2} \right)^2 \right) dx < \infty \tag{3.45}$$

Examples of $W_2^{(1)}$ and $W_2^{(2)}$ functions are shown in Figure 3.2. Note that differentiation lowers the order of the space. If u belongs to $W_2^{(2)}$, then $\frac{du}{dx}$ belongs to $W_2^{(1)}$. The above definitions can be extended to two and three dimensions by replacing the scalar operators with vector products.

All functions satisfying (3.43), i.e. those that are square integrable, are said to belong to the L_2 function space. This space includes most of the functions that we shall deal with.

We now solve the problem of equation (3.38). Let $\mathcal{L}$ be an *nth* order operator and $p \in W_2^{(2)}$. Also, we do not distinguish between essential and natural boundary conditions. Thus $\mathcal{J} - g$ may represent a combination of essential and natural boundary conditions over the exterior domain.

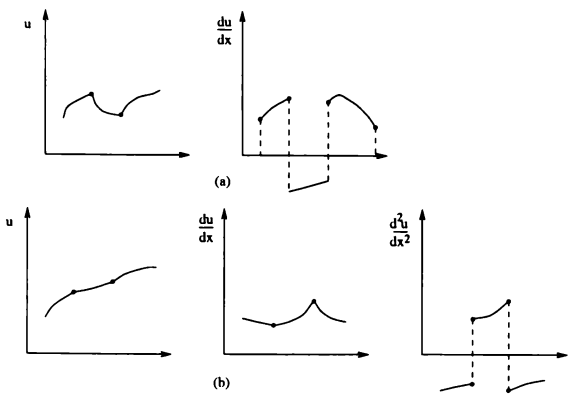

Figure 3.2: Types of function: (a) first-derivative square integrable, $W_2^{(1)}$; (b) second-derivative square integrable,$W_2^{(2)}$

The classical solution is a function belonging to the $W_2^{(n+1)}$ space and satisfies $\epsilon = \mathcal{L}(u) - p = 0$.

Using the weighted-residual method, the approximate solution is:

$$u = u_B + \sum_{j=1}^{N} \alpha_j \phi_j \tag{3.46}$$

where u_B satisfies the prescribed boundary condition,

$$\mathcal{L}(u_B) - p = 0 \tag{3.47}$$

and ϕ_j are functions belonging to the trial space which satisfy the homogeneous boundary conditions,

$$\mathcal{L}(\phi_j) = 0 \tag{3.48}$$

$$j = 1, 2, ..., N$$

The order of the trial space is determined by the order of $\mathcal{J}$ and p.

Our restriction on the approximation gave $\epsilon = 0$ on the boundary. A measure of the error is the inner product of the residual, ϵ, and a test (weighting) function, w:

$$\text{Error measure} =< \epsilon, w >= \int_\Gamma (\mathcal{L}(u) - p) w d\Omega \tag{3.49}$$

If we now release the continuity requirements on the function, i.e. lowering the order of the function space, we obtain a "weak" solution. If the weak solution can be proved to be unique, it is called the generalised solution. The "optimum" weak form is the one for which the trial and test spaces coincide. Optimum refers here to the balance between uniqueness and existence. Hence the weighted residual method is a numerical scheme for generating a weak solution.

3.6 Continuity

Continuity refers to the continuity of the solution along element boundaries. The very nature of the finite element method implies a piecewise solution of the problem. Functions can be assigned a degree of continuity. A function that is C^0, is continuous. A function for which the first derivative is continuous is said to be of class C^1, similarly if its second derivative is continuous, it is of class C^2.

Flux discontinuities cannot be modeled well inside an element because the shape functions and their derivatives are very smooth functions. On the other hand C^0 elements permit flux discontinuities on the boundaries. Hence elements can not overlap at interfacial boundaries. All the elements considered will be of class C^0 continuity.

3.7 The Finite Element Technique

3.7.1 Overview

In the fem technique, the matrix for the whole continuum (global matrix) is formed by the contributions of the matrices of the elements, which are expressed as functions of the nodal unknowns. To this global matrix the essential boundary conditions are applied. Similarly the element inputs form a vector of generalised nodal actions. Once the system of equations is solved for the unknowns, other functions can be calculated.

The basic steps of the method are:

Reformulation of the partial differential equation into an equivalent variational formulation via the weak method;

Discretisation of the region into finite elements;

Computation of the elemental matrices;

Assembly of the system matrix;

Insertion of the boundary conditions;

Solution of the resulting system of equations;

Calculation of any other function based on the nodal unknowns;

output the data.

The fem is applied to a region. The region is divided into a number of elements composed of nodes. We seek to solve the nodal unknowns of each element. Each element is analysed separately and its properties are generally derived from the minimisation of the Galerkin type expression governing the problem, after choosing some approximate function for the element variables. These approximation functions have to satisfy the admissibility and completeness conditions for the problem. Admissibility implies continuity of the essential variables between the elements for given boundary conditions. Completeness is a necessary condition for convergence to the exact solution. If both of these conditions are satisfied the solution will converge to its correct value as the total number of elements is increased. The element is said to be a conforming element. It should be noted that there are elements that satisfy only the admissibility condition (i.e. are complete, but not continuous). They are called non-conforming elements, but are not considered further. Refer to Cuvelier [Cuvelier 85] for a full discussion of such elements.

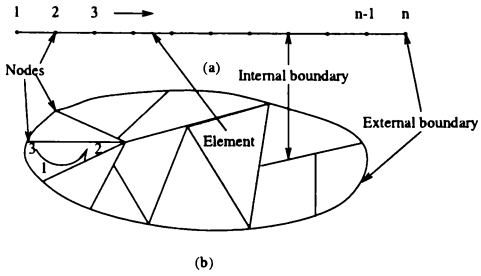

Figure 3.3: Finite element discretisation: (a) one dimension; (b) two dimensions

Figure 3.3 shows one and two dimensional regions discretised into "finite elements". The nodes are numbered in one dimension, from left to right, and in two dimensions, anti-clockwise.

Two reference systems are used: The local numbering system, which is used when referring to a single element; and the global system which is used when considering the assembled system of elements.

3.7.2 Formulation of the Problem

We reformulate the classical form of the pde by utilising the weighted residual method. The particular type of residual method chosen is the Galerkin method (i.e. the weighting and trial functions are the same). By integrating the highest order differential by parts we arrive at the equivalent weak formulation of the classical pde.

Consider the time independent pde:

$$-\nabla \cdot \nabla (\alpha u) + \nabla (\beta u) + \gamma u = f \tag{3.50}$$

with boundary conditions:

$$\begin{aligned} u &= g_0 \text{ on } \Gamma_1 \\ \alpha \frac{\partial u}{\partial n} &= g_1 \text{ on } \Gamma_2 \end{aligned} \tag{3.51}$$

where $\alpha, \beta, \gamma, f, q, u$ are some prescribed functions on the domain and $\Gamma = \Gamma_1 + \Gamma_2$ is the total boundary.

We multiply equation (3.90) by a function φ with $\varphi_{\Gamma_1} = 0$; integrate over Γ; apply Green's formula; and substitute the non-homogeneous Neumann boundary condition at Γ_2. That is:

$$\int_\Gamma \{-\nabla \cdot \nabla(\alpha u) + \nabla(\beta u) + \gamma u\} \varphi d\Omega = \int_\Gamma f\varphi d\Omega \tag{3.52}$$

$$\int_\Gamma \alpha \nabla u \nabla \varphi d\Omega + \int_\Gamma \varphi \nabla(\beta u) d\Omega + \int_\Gamma u\gamma\varphi d\Omega - [(\alpha \nabla u)\,\varphi]_\Gamma = \int_\Gamma f\varphi d\Omega$$

$$\int_\Gamma \alpha \nabla u \nabla \varphi d\Omega + \int_\Gamma \varphi \nabla(\beta u) d\Omega + \int_\Gamma u\gamma\varphi d\Omega = \int_\Gamma f\varphi d\Omega + g_1\varphi(\Gamma_2)$$

Let φ be a function with $\varphi(\Gamma_1) = 1$, then the weak formulation is:

$$\text{Find } u \text{ with } u - g_0\varphi_0 \in V \text{ such that} \tag{3.53}$$

$$a(u, \varphi) = \int_{\Gamma_0}^{\Gamma_1} f\varphi d\Omega + g_1\varphi(\Gamma_2) \text{ for all } \varphi \in V \tag{3.54}$$

where $V=$ the space of functions that vanish at Γ_1.

Note that the Dirichlet condition is an essential boundary condition and that the Neumann condition is a natural one since it is automatically satisfied by the solution u.

3.7.3 Discretisation

In the space V we choose a finite number of basis functions $\varphi_1, ..., \varphi_N$. When the function space spanned by these basis functions is denoted by V_N, the approximate weak formulation becomes

$$\text{Find } \tilde{u} \text{ with } \tilde{u} - g_0\varphi_0 \in V_N \text{ such that} \tag{3.55}$$

$$a(\tilde{u}, \varphi) = \int_{\Gamma_0}^{\Gamma_1} f\varphi d\Omega + g_1\varphi(\Gamma_2) \text{ for all } \varphi \in V_N$$

Writing $\tilde{u}$ in the form

$$\tilde{u} = g_0\varphi_0 + \sum_{j=1}^{N} \tilde{u}_j\varphi_j \tag{3.56}$$

then equation (3.56) is equivalent to

$$\sum_{j=1}^{N} \tilde{u}_j \int_{\Gamma_0}^{\Gamma_1} \frac{d\varphi_j}{dx} \alpha \frac{d\varphi_i}{dx} d\Omega + \sum_{j=1}^{N} \tilde{u}_j \int_{\Gamma_0}^{\Gamma_1} \varphi_i \beta \frac{d\varphi_j}{dx} d\Omega + \sum_{j=1}^{N} \tilde{u}_j \int_{\Gamma_0}^{\Gamma_1} \varphi_j \gamma \varphi_i d\Omega \tag{3.57}$$

$$= \int_{\Gamma_0}^{\Gamma_1} f\varphi_i d\Omega - g_0 \int_{\Gamma_0}^{\Gamma_1} \frac{d\varphi_0}{dx} \frac{d\varphi_i}{dx} d\Omega + g_1 \varphi_i(\Gamma_1) \quad i = 1, 2, ..., N$$

We can rewrite equation (3.58) in matrix form:

$$\left([U]^{(e)} + [K]^{(e)} + [H]^{(e)}\right) \{u\} \;=\; \{F\}^{(e)} \tag{3.58}$$

where:

$$\begin{aligned} K_{ij}^{(e)} &= \int^{(e)} \nabla \varphi_i^{(e)} \alpha \nabla \varphi_j^{(e)} d\Omega \\ U_{ij}^{(e)} &= \int^{(e)} \varphi_i^{(e)} \nabla (\beta \varphi_j^{(e)}) d\Omega \\ H_{ij}^{(e)} &= \int \varphi_i^{(e)} \gamma \varphi_j^{(e)} d\Omega \\ F_i^{(e)}(t) &= F f_i^{(e)}(t) + F\tau_i^{(e)}(t) \\ &= \int^{(e)} f\varphi_i^{(e)} d\Omega + g_1 \varphi^{(e)} \end{aligned} \tag{3.59}$$

We have assigned the superscript (e) to denote that we are working at the elemental level.

We have now reached a stage where the partial differential equation is suitable for numerical evaluation. The function in equation (3.56) is a linear combination of basis functions φ_j possessing the properties described in section 3.3. These basis functions represent the individual elements. The polynomial basis functions may be of varying order. Figure (3.4) shows some first, second and third order elements in 1 and 2 dimensions.

3.7.4 The Finite Elements

There exists a vast array of finite elements and techniques for generating them. In one dimension, the element can be built from a linear, parabolic, or higher order polynomial. There is a greater variety of elements in two dimensions. The representative elements are often either triangular or quadrilateral in shape, and are again of varying order of polynomial representation. Higher orders of representing polynomial functions generally result in faster rates of convergence and therefore usually greater accuracy.

For lower order elements it is often simpler to use direct methods for generating the elements. Numerical techniques are often used for higher order elements in conjunction with Isoparametric transformations.

Interpolation Functions/Shape Functions

Interpolation polynomials are chosen to represent the discrete model. Each element is defined using an interpolation function to describe its behaviour between end points (called nodes).

The shape function is the coefficient that appears in the interpolation polynomial. The shape function is a set of basis functions which span a defined space as discussed previously for each node of the element. A shape function is written for each individual node of a finite element and has the property that its magnitude is 1 at that node and 0 for all the other nodes in that element.

Usual terminology is to use N to represent the shape function. I have chosen a more descriptive terminology and use φ^e, which shows its relation to the interpolation polynomial. Let us now look at some of the formulations of some of the elements.

1-d C^0 Linear Element

The two-node 1-d linear element as shown in Figure 3.4a has the trial solution:

$$\tilde{U}^{(e)}(x;a) = \sum_{j=1}^{2} a_j \varphi_j^{(e)}(x) \tag{3.60}$$

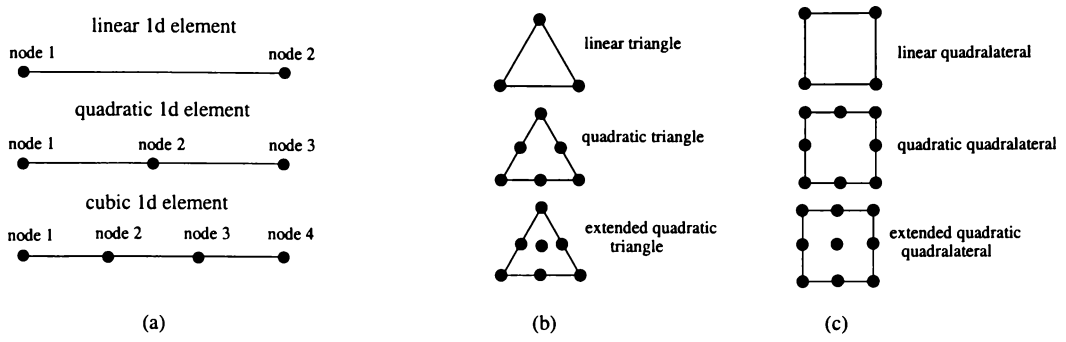

Figure 3.4: Finite elements: (a) one dimensional elements; (b) two dimensional triangular elements; (c) two dimensional quadrilateral elements.

where the shape functions $\varphi_j^{(e)}(x)$ are:

$$\varphi_1^{(e)}(x) = \frac{x_2 - x}{x_2 - x_1}, \quad \varphi_2^{(e)}(x) = \frac{x - x_1}{x_2 - x_1} \tag{3.61}$$

1-d C^0 Quadratic Element

The three-node 1-d quadratic element as shown in Figure 3.4a has the trial solution:

$$\tilde{U}^{(e)}(x; a) = \sum_{j=1}^{3} a_j \varphi_j^{(e)}(x) \tag{3.62}$$

where the shape functions $\varphi_j^{(e)}(x)$ are:

$$\begin{aligned} \varphi_1^{(e)}(x) &= \frac{(x - x_2)(x - x_2)}{(x_1 - x_2)(x_1 - x_3)} \\ \varphi_2^{(e)}(x) &= \frac{(x - x_1)(x - x_1)}{(x_2 - x_1)(x_2 - x_3)} \\ \varphi_3^{(e)}(x) &= \frac{(x - x_1)(x - x_1)}{(x_3 - x_1)(x_3 - x_2)} \end{aligned} \tag{3.63}$$

2-d C^0 Linear Triangular Element

The three-node 2-d C^0 linear element as shown in Figure 3.4b has the trial solution:

$$\tilde{U}^{(e)}(x, y; a) = \sum_{j=1}^{3} a_j \varphi_j^{(e)}(x, y) \tag{3.64}$$

where the shape functions $\varphi_j^{(e)}(x)$ are:

$$\varphi_j^{(e)}(x, y) = \frac{a_j + b_j x + c_j y}{2\Delta} \quad j = 1, 2, 3 \tag{3.65}$$

and

$$
\begin{aligned}
a_j &= x_k y_l - x_l y_k \qquad (3.66)\\
b_j &= y_k - y_l \\
c_j &= x_l - x_k \\
\Delta &= \frac{1}{2}\begin{vmatrix} 1 & x_1 & y_1 \\ 1 & x_2 & y_2 \\ 1 & x_3 & y_3 \end{vmatrix} \\
&= \frac{1}{2}[(x_2 y_3 - x_3 y_2) - (x_1 y_3 - x_3 y_1) + (x_1 y_2 - x_2 y_1)] \\
&= \text{area of element}
\end{aligned}
$$

The subscripts i, k, l have the values $1, 2, 3$ for $\varphi_1^{(e)}(x, y)$ and are permuted cyclically for $\varphi_2^{(e)}(x, y)$ and $\varphi_3^{(e)}(x, y)$.

The shape functions described above are formulated onto the real element's local coordinate system. This gives a physically intuitive feel to the shape function. However, shape functions can be considerably simplified and generalised with the concept known as isoparametric elements.

3.7.5 Isoparametric Elements

Isoparametric elements are formulated on a natural coordinate system. Natural coordinates are a local system that permit the specification of a point within the element by a set of dimensionless numbers whose magnitudes never exceed unity. The shape function uses a parametric mapping on a parent element and then maps them to the real element.

Isoparametric elements employ the standard form for the element trial solution and the shape functions satisfy the interpolation property. However, the shape functions are generated indirectly, by first developing a master set of shape functions using a direct approach, and then mapping (transforming) the master set onto each of the real elements in a mesh. The complexity of the mapping generally makes it impossible to write down explicit expressions for the resulting shape functions $\varphi_j^{(e)}(x)$.

Since the isoparametric approach results in shape functions being defined implicitly rather than explicitly, there is necessarily a greater reliance on numerical procedures.

Isoparametric transformation is the standard approach that the fem relies on when it has to deal with curved geometries, which is a strong point of the fem.

The transformation from straight to curved sides is done as follows. Consider that the x, y coordinates can be expressed in terms of curvilinear coordinates:

$$x = x(\xi, \eta), \quad y = y(\xi, \eta) \tag{3.67}$$

The general transformations for a function φ is

$$\begin{aligned} \frac{\partial \varphi}{\partial x} &= \frac{\partial \varphi}{\partial \xi}\frac{\partial \xi}{\partial x} + \frac{\partial \varphi}{\partial \eta}\frac{\partial \eta}{\partial x} \\ \frac{\partial \varphi}{\partial y} &= \frac{\partial \varphi}{\partial \xi}\frac{\partial \xi}{\partial y} + \frac{\partial \varphi}{\partial \eta}\frac{\partial \eta}{\partial y} \end{aligned} \tag{3.68}$$

Generally explicit expressions for ξ, η in terms of x and y are not easily available.

Taking the derivatives of $\varphi(x, y)$ with respect to ξ and ν:

$$\begin{Bmatrix} \frac{\partial \varphi}{\partial \xi} \\ \frac{\partial \varphi}{\partial \eta} \end{Bmatrix} = \begin{bmatrix} \frac{\partial x}{\partial \xi} & \frac{\partial y}{\partial \xi} \\ \frac{\partial x}{\partial \eta} & \frac{\partial y}{\partial \eta} \end{bmatrix} \begin{Bmatrix} \frac{\partial \varphi}{\partial x} \\ \frac{\partial \varphi}{\partial y} \end{Bmatrix} = J^{(e)}(\xi, \eta) \begin{Bmatrix} \frac{\partial \varphi}{\partial \xi} \\ \frac{\partial \varphi}{\partial y} \end{Bmatrix} \tag{3.69}$$

Inverting gives:

$$\begin{Bmatrix} \frac{\partial \varphi}{\partial x} \\ \frac{\partial \varphi}{\partial y} \end{Bmatrix} = (J^{(e)}(\xi, \eta))^{-1} \begin{Bmatrix} \frac{\partial \varphi}{\partial \xi} \\ \frac{\partial \varphi}{\partial \eta} \end{Bmatrix} \tag{3.70}$$

and

$$\begin{aligned} \frac{\partial \varphi}{\partial x} &= \frac{1}{|J^{(e)}(\xi, \eta)|}\left(\frac{\partial y}{\partial \eta}\frac{\partial \varphi}{\partial \xi} - \frac{\partial y}{\partial \xi}\frac{\partial \varphi}{\partial \eta}\right) \\ \frac{\partial \varphi}{\partial y} &= \frac{1}{|J^{(e)}(\xi, \eta)|}\left(-\frac{\partial x}{\partial \eta}\frac{\partial \varphi}{\partial \xi} + \frac{\partial x}{\partial \xi}\frac{\partial \varphi}{\partial \eta}\right) \end{aligned} \tag{3.71}$$

where $|J^{(e)}(\xi, \eta)|$ is the determinant of $J^{(e)}(\xi, \eta)$ and is called the Jacobian.

$$|J^{(e)}(\xi, \eta)| = \frac{\partial x}{\partial \xi}\frac{\partial y}{\partial \eta} + \frac{\partial x}{\partial \eta}\frac{\partial y}{\partial \xi} \tag{3.72}$$

The Jacobian gives the amount of local expansion or contraction of the coordinates due to the mapping and must be finite if the transformation is to be unique. The differential area transforms to:

$$\mathrm{d}A = |J^{(e)}(\xi,\eta)|\mathrm{d}\xi\mathrm{d}\eta \tag{3.73}$$

The value of $|J^{(e)}(\xi,\eta)|$ gives the amount of local expansion or contraction of the coordinates due to the mapping.

3.7.6 2-d C^0 Linear Triangular Element

The shape functions in curvilinear space are:

$$\begin{aligned} \varphi_1(\xi,\eta) &= \xi \\ \varphi_2(\xi,\eta) &= \eta \\ \varphi_3(\xi,\eta) &= 1-\xi-\eta \end{aligned} \tag{3.74}$$

3.7.7 2-d C^0 Quadratic Triangular Element

The shape functions in curvilinear space are:

$$\begin{aligned} \varphi_1(\xi,\eta) &= [1-(\xi+\eta)][1-2(\xi+\eta)] \\ \varphi_2(\xi,\eta) &= \xi(2\xi-1) \\ \varphi_3(\xi,\eta) &= \eta(2\eta-1) \\ \varphi_4(\xi,\eta) &= 4\xi[1-(\xi+\eta)] \\ \varphi_5(\xi,\eta) &= 4\xi\eta \\ \varphi_6(\xi,\eta) &= 4\eta[1-(\xi+\eta)] \end{aligned} \tag{3.75}$$

3.7.8 2-d C^0 Linear 4 Noded Quadrilateral Element

$$\begin{aligned} \varphi_1(\xi,\eta) &= \frac{1}{4}(1-\xi)[1-\eta) \\ \varphi_2(\xi,\eta) &= \frac{1}{4}(1+\xi)(1-\eta) \end{aligned} \tag{3.76}$$

$$\varphi_3(\xi,\eta) = \frac{1}{4}(1+\xi)(1+\eta)$$
$$\varphi_4(\xi,\eta) = \frac{1}{4}(1-\xi)(1+\eta)$$

3.7.9 2-d 8 Noded Quadratic Quadrilateral Element

$$\begin{aligned}
\varphi_1(\xi,\eta) &= -\frac{1}{4}(1-\xi)[1-\eta)(1+\xi+\eta) \\
\varphi_2(\xi,\eta) &= \frac{1}{2}(1-\xi^2)(1-\eta) \\
\varphi_3(\xi,\eta) &= \frac{1}{4}(1+\xi)(1-\eta)(\xi-\eta-1) \\
\varphi_4(\xi,\eta) &= \frac{1}{2}(1-\eta^2)(1+\xi) \\
\varphi_5(\xi,\eta) &= \frac{1}{4}(1+\xi)(1+\eta)(\xi+\eta-1) \\
\varphi_6(\xi,\eta) &= \frac{1}{2}(1-\xi^2)(1+\eta) \\
\varphi_7(\xi,\eta) &= -\frac{1}{4}(1-\xi)(1+\eta)(\xi-\eta+1) \\
\varphi_8(\xi,\eta) &= \frac{1}{2}(1-\eta^2)(1+\xi)
\end{aligned} \tag{3.77}$$

The (isoparametric) mapping functions for all of the above elements are:

$$\begin{aligned}
x &= \sum_{k=1}^{n} x_k^{(e)} \varphi_k(\xi,\eta) \\
y &= \sum_{k=1}^{n} y_k^{(e)} \varphi_k(\xi,\eta)
\end{aligned} \tag{3.78}$$

where n is 3 and 6 for their respective linear and quadratic triangular elements, and 4 and 8 for their respective linear and quadratic quadrilateral finite elements.

Computer algebra packages such as Macsyma [Macsyma] make the direct generation of elements relatively straight forward. They can even generate Fortran or C code for use in a finite element program.

No Gauss points, n	Accuracy of quadrature	Gauss points ξ_{nl}	Weights, w_{nl}
1	$0(h^2)$	$\xi_{11} = 0$	$w_{11} = 2$
2	$0(h^4)$	$\xi_{21} = -1/3$	$w_{21} = 1$
		$\xi_{22} = -\xi_{21}$	$w_{22} = w_{21}$
3	$0(h^6)$	$\xi_{31} = -\frac{\sqrt{3}}{\sqrt{5}}$	$w_{31} = 5/9$
		$\xi_{32} = 0$	$w_{32} = 8/9$
		$\xi_{33} = -\xi_{31}$	$w_{33} = w_{31}$

Table 3.1: Gauss points and weights for Gauss-Legendre quadrature rules for one-dimensional elements and two-dimensional quadrilateral elements.

3.7.10 Gaussian Quadrature

For the isoparametric transformation we need to evaluate the parent element. This is done numerically with Gauss Legendre quadrature. The integrals are each of the form: For the 1-d elements,

$$\int_{-1}^{1} I(\xi)d\xi \approx \sum_{l=1}^{n} w_{nl} I(\xi_{nl}); \tag{3.79}$$

for the 2-d triangular elements,

$$\int_0^1 \int_0^{1-\eta} I(\xi,\eta)d\xi d\eta \approx \frac{1}{2}\sum_{l=1}^{n} w_{nl} I(\xi_{nl},\eta_{nl}) \tag{3.80}$$

and for 2-d quadrilateral elements,

$$\int_0^1 \int_0^1 I(\xi\eta)d\xi d\eta \approx \sum_{l=1}^{n}\sum_{k=1}^{m} w_{nl} w_{mk} I(\xi_{nl},\eta_{nl}) \tag{3.81}$$

where w_{nl} and w_{nl} are weight factors and the ξ_{nl} are the quadrature points at which the integrand is evaluated.

Gauss-Legendre quadrature is used; the ξ_{nl} are the zeros of the *nth*-degree Legendre polynomial and are the Gauss points. The Legendre polynomials are an infinite set of orthogonal polynomials. The above tables show the Gauss points and weights for both the 1- and 2d shape functions used.

No Gauss points, n	Accuracy of quadrature	Gauss points ξ_{nl}	η_{nl}	Weights, w_{nl}
1	$0(h^2)$	$\xi_{11} = 1/3$	$\eta_{11} = 1/3$	$w_{11} = 1$
3	$0(h^3)$	$\xi_{31} = 1/6$	$\eta_{31} = 1/6$	$w_{31} = 1/3$
		$\xi_{32} = 2/3$	$\eta_{32} = 1/6$	$w_{32} = 1/3$
		$\xi_{32} = 1/6$	$\eta_{33} = 2/3$	$w_{33} = 1/3$
4	$0(h^4)$	$\xi_{41} = 1/3$	$\eta_{41} = 1/3$	$w_{41} = -27/48$
		$\xi_{42} = 1/5$	$\eta_{42} = 1/5$	$w_{42} = 25/48$
		$\xi_{43} = 3/5$	$\eta_{43} = 1/5$	$w_{43} = 25/48$
		$\xi_{44} = 1/5$	$\eta_{44} = 3/5$	$w_{44} = 25/48$

Table 3.2: Gauss points and weights for Gauss-Legendre quadrature rules for two-dimensional triangular elements.

3.7.11 Assembly of the System Matrix

An NxN system matrix is assembled from adding each local element matrix from 1 to the total number of elements (NEL) to it. The element matrices overlap where contributions to common nodes are encountered.

Once the system matrix is assembled the essential (Dirichlet) boundary conditions are inserted. As natural (Neuman) boundary conditions form part of the equation, they are incorporated into the elemental matrices.

3.7.12 Solution Techniques of the Assembled Matrices

The assembled system of equations form a set of matrices, $[A]\{x\} = \{b\}$. There exists a plethora of software available, both commercial and freeware, to solve such a system. The Sparse Linear Equation Solver [Kundert 1988] is an excellent free black box solver for both symmetric and unsymmetric $[A]$ matrices. The NAG libraries also provide excellent commercially supported matrix equation solvers [NAG].

3.8 Coupled Partial Differential Equations

Coupled pdes are a natural extension to fem techniques. An integrated method of solution for the coupled electrochemical equations is chosen. The degrees of freedom (DOF) are computed directly without numerical differentiation. The method

is clear and direct to understand. However, a major disadvantage of this method is the fact that the system of equations becomes very large and a lot of computing is required.

Each trial solution uses the same set of trial functions, but a different set of DOF. Using the same trial functions loses no generality since they are merely a "basis" in terms of which the trial solutions are expanded. It is the numerical values of the coefficients of these functions, i.e., the values of the DOF, that determine the resulting trial solution.

3.9 Numerical Solution of Non-Linear Differential Equations

Non-linear pdes are solved numerically by iteratively solving (i.e. linearising) the nonlinear simultaneous equations until a suitable convergence limit has been reached.

There are numerous methods for solving non-linear partial differential equations, with no one method being suitable for all problems. Two methods are described: the Newton-Raphson method; and the modified Newton Method. The Newton-Raphson method has stronger convergence properties; however, the modified Newton method often converges faster (the Jacobian matrix is only calculated once).

3.9.1 The Newton-Raphson Method

We extrapolate the matrix equation (3.58) to include a general non-linear coupled set of equations. The $[U]$, $[K]$, $[H]$ and $\{F\}$ matrices can now have non-linear terms. We define a vector $\{a\}$ to take into account coupled equations. For two unknowns $\{a\}$ is:

$$\{a\} = \begin{Bmatrix} u_1 \\ v_1 \\ u_2 \\ v_2 \\ \cdot \\ \\ \cdot \\ u_n \\ v_n \end{Bmatrix} = \begin{Bmatrix} a_1 \\ a_2 \\ a_3 \\ a_4 \\ \cdot \\ \\ \\ a_{2n-1} \\ a_{2n} \end{Bmatrix} \tag{3.82}$$

We set our generalised equation of (3.58) to zero and equate it to a residual vector $\{r^k\}$

$$\{r^k\} = \left([U]^{(e)} + [K]^{(e)} + [H]^{(e)}\right)\{a(t)\} - \{F(t)\}^{(e)} = 0 \tag{3.83}$$

In the Newton-Raphson method (and indeed in all Newton-type methods), we assume that the behavior of the residual vector in the neighborhood of the previous solution u^k is linear, i.e.

$$\left[J^k\right]\left(\left\{a^{k+1}\right\} - \left\{a^k\right\}\right) = -\left\{r^k\right\} \tag{3.84}$$

Rearranging (3.84) to find the new solution a^{k+1},

$$\left\{a^{k+1}\right\} = \left\{a^k\right\} - \left[J^k\right]^{-1}\left\{r^k\right\} \tag{3.85}$$

where J is the Jacobian matrix, and has the general equation form:

$$[J^k] = ([U]^{(e)} + [K]^{(e)} + [H]^{(e)})\frac{\partial a}{\partial a} - \frac{\partial f}{\partial a} \tag{3.86}$$

The numerical solution is more computationally efficient at solving equations (3.84) rather than the inversion technique suggested in equation (3.85).

Such paths are successively taken unless an appropriate norm of the residual vectors satisfies a given convergence criterion, e.g.

$$\| a^{k+1} \| < \epsilon_k \tag{3.87}$$

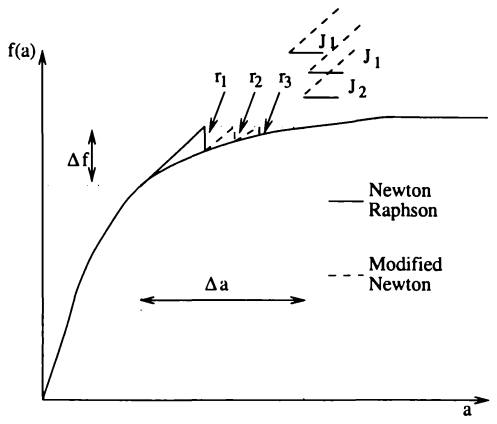

Figure 3.5: Newton-Raphson and Modified Newton methods in one-dimensional problems.

where $\| \cdot \|$ stands for the L_2 vector norm $\| a \| = (\sum_i a_i^2)^{1/2}$. Such a tangent iteration procedure is illustrated on Figure 3.5 for a one-dimensional case and is computationally expensive since the Jacobian matrix is allowed to vary continually and hence each iteration implies factorisation or Gauss elimination on a new matrix.

3.9.2 The Modified Newton Method

A modified Newton iteration technique is often preferred over the Newton-Raphson as it assumes that the actual Jacobian matrix may be kept constant for a certain number of paths, as shown in Figure 3.5.

$$\{a^{k+1}\} = \{a^k\} - [J^{k_0}]^{-1} \{r^k\}; \quad k \geq k_0 \tag{3.88}$$

The modified iteration procedure can be used from the beginning of each time step (pure modified Newton method) in which case only one evaluation and factorisation of the iteration matrix is needed per time step. The convergence criteria is

$$\| a^{k_0} \| < \epsilon_k \tag{3.89}$$

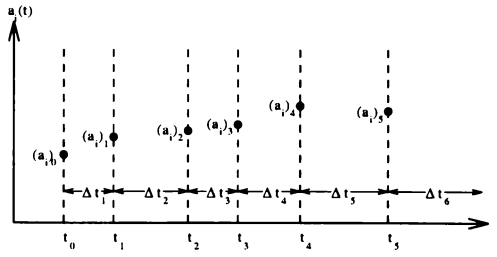

Figure 3.6: Division of the time axis into steps Δt_1, Δt_2,..., for time-stepping methods, and computed discrete values $(a_i)_n$ at times t_n, $n - 1, 2, ...$

with a convergence threshold $\epsilon > \epsilon_k$. That is, the corresponding number of iterations to convergence is greater than the standard tangent (Newton-Raphson) iteration procedure. However these types of iterations are generally much cheaper since they involve only computations of the current residual vector (corresponding to the previous displacement).

3.10 Time Stepping Techniques

3.10.1 Introduction

In all time-stepping methods, the time axis is divided into a succession of time steps Δt_i, $i = 1, 2, ...$, beginning at time t_0, as shown in Figure 3.6. Some methods require the steps to be of uniform length, others allow the steps to be of different length. We seek a solution for $\{a(t)\}$ over the continuous domain of t, using an approximate solution that consists of discrete values for $\{a(t)\}$ at the end of each step, starting from the known initial value a_0 at time t_0 for the ith component of $\{a(t)\}$.

The discrete values $\{a\}_n$, $n = 1, 2, ...$, are computed from a recurrence relation which relates the values for $\{a\}$ at two or more successive times. The recurrence relation is an approximation to the differential equation. Almost all of these time-stepping methods can be classified as Linear Multistep (LMS) methods, where linear refers to the nature of the recurrence relation, and not to the differential equation which can be non-linear.

The LMS one-step method chosen relates the discrete values at both ends of a single time-step. It is often used for first-order initial-value problems.

The general time-stepping equation used is often called the θ-time-stepping equation. It encompasses three finite difference formulas:

i The backward Euler method (backward difference);

ii The Crank-Nicolson method (mid-difference); and

iii The Euler method (forward difference).

Of these three time stepping techniques, the backward Euler and the Crank-Nicholson methods are used as implicit methods, and the Euler method as an explicit methods.

3.10.2 Implicit Time-Stepping Methods

The main drawback of an implicit method is the relative complexity of the associated computer program, especially for non-linear problems. This is for the following reasons:

i Implicit methods involve solving a full system of equations of the size of the system, with an iteration matrix which has to be updated regularly for nonlinear problems;

ii A re-evaluation of the Jacobian iteration matrix requires the computation; and of the element level. The computational efficiency of the finite element program is of course highly dependent on the cost of this operation and the way it is implemented in combination with the elimination or factorisation of the Jacobian matrix.

iii Computational strategies for non-linear analysis are more complex not only to develop, but also to use, since the user has freedom in the choice of the type of iteration method or combination of them in the same solution.

However, the advantages of the implicit method are:

i It is much more flexible than explicit methods. There is no restriction to the types of problems that can be solved; and

ii It is far more stable than explicit methods, and can lead to more economical solutions as longer time steps can be used.

3.10.3 The θ Finite Difference Method

As regards notation, each of the following recurrence relations will be derived for the nth time step, Δt_n, which carries the solution from time t_{n-1} to time t_n. This is illustrated symbolically in Figure 3.7 for a typical DOF $a_i(t)$ where we have already stepped the solution forward through the first $n-1$ time steps. We therefore know the solution at time t_{n-1} but not at t_n.

We extend our original pde, eqn (3.90) to the time domain, i.e.:

$$\mu \frac{\partial u}{\partial t} - \nabla \cdot \nabla (\alpha u) + \nabla (\beta u) + \gamma u = f \tag{3.90}$$

with the respective initial and boundary conditions as prescribed in section 3.90, and μ is a coefficient.

The time dependent component is formulated in exactly the same way as discussed in Section 3.7.3. If we keep the same matrix notation as discussed in Section 3.9.1 to account for coupled equations, then we get the following matrix equation:

$$[C] \left\{ \frac{da}{dt} \right\}_\theta + \left([U]^{(e)} + [K]^{(e)} + [H]^{(e)} \right) \{a\}_\theta = \{F\}_\theta \tag{3.91}$$

where

$$\theta = \frac{t - t_{n-1}}{\Delta t_n} \qquad (\Delta t_n = t_n - t_{n-1})$$

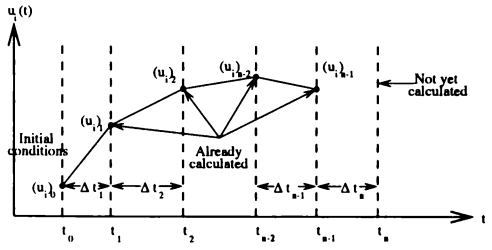

Figure 3.7: Solution has been computed at the end of the first $n-1$ time steps, $(a_i)_1, (a_i)_2, ...(a_i)_{n-1}$; next we want to compute the solution $(a_i)_n$ at time t_n.

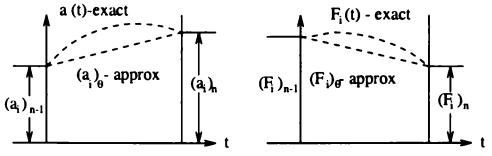

Figure 3.8: $\{a\}$ and $\{F(t)\}$ approximated by linear variation over nth step.

θ varies from 0 to 1 over the time step.

Approximate expressions for $\{da/dt\}_\theta$, $\{a\}_\theta$, and $\{F\}_\theta$ may be obtained by approximating $\{a(t)\}$ and $\{F(t)\}$ by linear polynomials over the step. θ can be written in term of interpolation polynomials in exactly the same manner as the C^0 linear element. Thus:

$$\{a\}_\theta \simeq (1-\theta)\{a\}_{n-1} + \theta\{a\}_n \tag{3.92}$$

and

$$\{F\}_\theta \simeq (1-\theta)\{F\}_{n-1} + \theta\{F\}_n \tag{3.93}$$

which are shown in Figure 3.8 for the ith components of the vectors. Differentiating (3.92) yields:

$$\left\{\frac{da}{dt}\right\}_\theta = \frac{1}{\Delta t_n}\frac{d\{a\}_\theta}{d\theta} = \frac{\{a\}_n - \{a\}_{n-1}}{\Delta t_n} \tag{3.94}$$

Substituting (3.92) through (3.94) into (3.91) and placing all the known terms on the right hand side (RHS) yields:

$$\left(\frac{1}{\Delta t_n}[C] + \theta\left([U]^{(e)} + [K]^{(e)} + [H]^{(e)}\right)\right)\{a\}_n \tag{3.95}$$

$$= (1-\theta)\{F\}_{n-1} + \theta\{F\}_n + \left(\frac{1}{\Delta t_n}[C] - (1-\theta)\left([U]^{(e)} + [K]^{(e)} + [H]^{(e)}\right)\right)\{a\}_{n-1}$$

This is now in the useful form:

$$[S_{eff}]\{a\}_n = \{F_{eff}\} \tag{3.96}$$

where

$$[S_{eff}] = \frac{1}{\Delta t_n}[C] + \theta\left([U]^{(e)} + [K]^{(e)} + [H]^{(e)}\right) \tag{3.97}$$

$$\begin{aligned}\{F_{eff}\} &= (1-\theta)\{F\}_{n-1} + \theta\{F\}_n \\ &+ \left(\frac{1}{\Delta t_n}[C] - (1-\theta)\left([U]^{(e)} + [K]^{(e)} + [H]^{(e)}\right)\right)\{a\}_{n-1}\end{aligned} \tag{3.98}$$

In equation (3.96) we get

$\theta = 0$: forward difference

$\theta = 1/2$: mid-difference

$\theta = 1$: backward difference

Note θ can be set to any value between 0 and 1 to allow the use of optimal recurrence relations.

The Explicit Forward Difference Method

Equation (3.96) is evaluated at the backward end of the time step, t_{n-1}, i.e.

$$[S_{eff}] = \frac{1}{\Delta t_n}[C] \tag{3.99}$$

$$\{F_{eff}\} = \{F\}_{n-1} + \left(\frac{1}{\Delta t_n}[C] - \left([U]^{(e)} + [K]^{(e)} + [H]^{(e)}\right)\right)\{a\}_{n-1} \tag{3.100}$$

If $[C]$ can be diagonalised (called lumping), then we can solve $\{a\}_n$ in equation (3.96) explicitly, i.e. divide the right hand side (RHS) term by the corresponding left hand side (LHS) coefficient on the diagonal of $[K_{eff}]$. This is computationally very fast.

Lumping is applied to the element consistent (non-lumped) capacity matrix $[C]^{(e)}$ prior to assembly. In each row of $[C]$ all the terms are added together and placed on the diagonal; the off-diagonal terms are zeroed. If we call the lumped capacity matrix $[CL]$, its components are

$$CL_{ii}^{(e)} = \sum_{j=1}^{n} C_{ij}^{(e)} \quad i = 1, 2, ..., n \tag{3.101}$$
$$CL_{ij}^{(e)} = 0 \quad i \neq j$$

Lumping can be interpreted as using a different set of shape functions just for the capacity integral. The shape functions would be equal to 1 over the part of the element touching a given node, and zero everywhere else. The shape functions: (i) satisfy the interpolation property $\varphi_j(x_i) = \delta_{ji}$; (ii) are discontinuous within the element; and (iii) do not overlap (this being the essential feature that diagonalises the matrix).

Equation (3.102) conserves the total capacity of the consistent capacity matrix:

$$\sum_{i=1}^{n}\sum_{j=1}^{n} CL_{ij}^{(e)} = \sum_{i=1}^{n}\sum_{j=1}^{n} C_{ij}^{(e)} \tag{3.102}$$

The rate of convergence for $[CL]$, however, may be lower than the consistent capacity matrix. Lumping can also can yield a significant increase in accuracy [Hint 76]. Also note that the variable $\mu(x)$ should be a constant over the element capacity integrals whereas with the other two implicit techniques, $\mu(x)$ can vary.

The main advantage of the explicit forward difference method over the other two methods is that it is computationally much faster. The disadvantage is that it is conditionally stable.

The Mid-Difference Method

Equation (3.96) is evaluated at the centre of the time step, i.e.

$$[S_{eff}] = \frac{1}{\Delta t_n}[C] + \frac{1}{2}\left([U]^{(e)} + [K]^{(e)} + [H]^{(e)}\right) \tag{3.103}$$

$$\{F_{eff}\} = \{F\}_{n-1/2} + \left(\frac{1}{\Delta t_n}[C] - \frac{1}{2}\left([U]^{(e)} + [K]^{(e)} + [H]^{(e)}\right)\right)\{a\}_{n-1} \quad (3.104)$$

The function values $\{a\}_{n-1/2}$ and $\{F\}_{n-1/2}$ are approximated by averaging over the step:

$$\{a\}_{n-1/2} \simeq \frac{\{a\}_{n-1} + \{a\}_n}{2}, \quad \{F\}_{n-1/2} \simeq \frac{\{F\}_{n-1} + \{F\}_n}{2} \quad (3.105)$$

$[S_{eff}]$ is a non-diagonal matrix, so equation (3.96) becomes coupled, necessitating $[S_{eff}]$ to be "inverted". Hence the unknown $\{a\}_n$ is defined implicitly by equation (3.96).

The mid-difference method is very popular. Its accuracy is $0(\Delta t^2)$, i.e. the error at a given time, in the limit $\Delta t \to 0$, is proportional to Δt^2 This is an order of magnitude better than the backward difference method. However, for typical time-step sizes the solutions often contain small oscillations (which die out as the solution steps forward). This means that asymptotic accuracy is frequently not realised.

The Backward Difference Method

The components of equation (3.96) become:

$$[S_{eff}] = \frac{1}{\Delta t_n}[C] + \left([U]^{(e)} + [K]^{(e)} + [H]^{(e)}\right) \quad (3.106)$$

$$\begin{aligned} \{F_{eff}\} &= \{F\}_{n-1} + \theta\{F\}_n \\ &+ \left(\frac{1}{\Delta t_n}[C] - \left([U]^{(e)} + [K]^{(e)} + [H]^{(e)}\right)\right)\{a\}_{n-1} \end{aligned} \quad (3.107)$$

Again, $[S_{eff}]$ is a non-diagonal matrix, so the unknown a_n is defined implicitly by equation (3.96).

The accuracy of the backward difference method is $0(\Delta t)$. Thus if you halve the time step, the error at a given time will generally decrease by approximately one half if Δt is small enough.

The backward difference method is quite well behaved, although it is not always optimal in terms of computational efficiency.

3.11 Stability of the Time-Stepping Methods

Stable or unstable behavior can be investigated by examining the free response of a multi-DOF system, i.e. when $f(x)$ vanishes:

$$[C]\left\{\frac{da}{dt}\right\}_\theta + \left([U]^{(e)} + [K]^{(e)} + [H]^{(e)}\right)\{a\}_\theta = \{0\} \tag{3.108}$$

The analytical solution is of the form

$$\{a(t)\} = \{v\}\, e^{-\lambda t} \tag{3.109}$$

where λ is the eigenvalue.

After some algebra, we can arrive at a general equation to describe the stability of the system for the θ-method:

$$\frac{(A_i)_n}{(A_i)_{n-1}} = \frac{1-(1-\theta)\lambda_i \Delta t}{1+\theta\lambda_i \Delta t} \quad i = 1, 2, ..., N \tag{3.110}$$

where $A(t)_j$ is described by:

$$\{a(t)\} = \sum_{j=1}^{N} A_j(t)\{v\}_j \tag{3.111}$$

The stability conditions predicted by equation (3.110) are illustrated in Figure 3.9. Note that in order for the successive values to not grow larger, the ratio of two successive time-step values must be less than 1, i.e.

$$\left|\frac{(A_i)_n}{(A_i)_{n-1}}\right| < 1 \quad i = 1, 2, ...N \tag{3.112}$$

Applying this inequality to (3.110) yields the following conditions:

$$\begin{aligned} \text{For } 0 \le \theta < 1/2: \ \lambda_i \Delta t &< \frac{2}{1-2\theta} \quad i = 1, 2, ..., N \\ \text{For } \theta \ge 1/2: \ \lambda_i \Delta t &> \frac{-2}{2\theta - 1} \quad i = 1, 2, ..., N \end{aligned} \tag{3.113}$$

Thus for conditional stability we could write:

$$\delta t < \delta t_{crit} \tag{3.114}$$

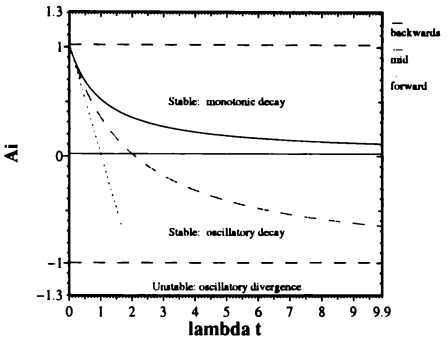

Figure 3.9: Stability behavior of one-step time-integration methods for first order initial-value problems.

where

$$\Delta t_{crit} = \left(\frac{2}{1-2\theta}\right)\frac{1}{\lambda_{max}} \tag{3.115}$$

Often λ_{max} can be very large, requiring very small time-steps. Thus conditionally stable methods are really only practical if they are explicit (as in the forward difference method) and computationally fast.

A simple method to determine λ_{crit} is outlined by Burnett ([Burnett 87]). Firstly one derives the exact eigensystem, for example consider the following problem:

$$\alpha\frac{\partial^2 U(x,t)}{\partial x^2} - \mu\frac{\partial U(x,t)}{\partial t} = 0 \quad 0 < x < L \tag{3.116}$$

The boundary conditions (b.c.) are $U(0,t) = U(L,t) = 0$ and α and μ are assumed constant. The free response has the form

$$U(x,t) = c(x)e^{-\lambda t} \tag{3.117}$$

Substituting equation (3.117) into (3.116) yields the eigenproblem

$$\frac{d^2 v(x)}{dx^2} + \lambda\frac{\mu}{\alpha}v(x) = 0 \tag{3.118}$$

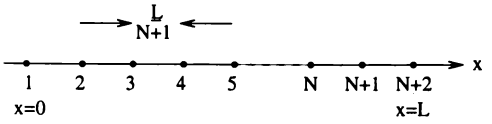

Figure 3.10: A uniform 1-d mesh

with b.c. $v(0) = v(L) = 0$. The solution of equation (3.118) is:

$$v(x) = asin\sqrt{\lambda\frac{\mu}{\alpha}}x + bcos\sqrt{\lambda\frac{\mu}{\alpha}}x \tag{3.119}$$

Applying the b.c. to equation (3.119) gives:

$$\lambda_n = \left(\frac{n\pi}{L}\right)^2 \frac{\alpha}{\mu} \tag{3.120}$$
$$v_n(x) = sin\frac{n\pi}{L}x$$

Now consider the 1-d mesh given in Figure 3.10 with $N + 2$. Nodes 1 and $N+2$ are both constrained, leaving only N free DOF. An eigensolution will therefore calculate the first N modes. The fe eigenvalue $\lambda_{max}(\lambda_N)$ will be an approximation to the *nth* exact eigenvalue:

$$\lambda_{max} \approx \left(\frac{N\pi}{L}\right)^2 \frac{\pi}{\mu} = \left(\frac{\pi}{\delta}\right)^2 \frac{\alpha}{\mu} \tag{3.121}$$

where $\delta = L/(N + 1)$ is the distance between the two adjacent nodes.

Equation (3.121) is an approximation for a uniform 1-d mesh. For a non-uniform mesh in multi-dimensions:

$$\lambda_{max} \leq \lambda_{max}^{(e)} \tag{3.122}$$

where $\lambda_{max}^{(e)}$ is the largest element eigenvalue of any element in the mesh. Thus, assuming the upper bound in equation (3.122) is an approximation, λ_{max} can be found by finding the largest eigenvalue of any single element.

3.12 Conclusion

This chapter has detailed the properties of pdes and the theory of the numerical fem schemes used to solve them. The types of pdes were classified, and it was

noted that analytical methods can only be used for the simplest of linear problems. Two types of numerical methods were defined for the approximate solutions of pdes, the finite difference method (fdm) and the finite element method (fem). The fem is covered in detail. The variational formulation of a pde is treated, and how it is discretised into a form suitable for computational solution is treated in detail.

The fem, although strictly linear, can be generalised to pdes that are nonlinear. The linearisation technique called the Newton-Raphson method is detailed and it is shown how it can be used to linearise a non-linear pde so that is suitable for the fem.

It is shown that coupled pdes are solved quite naturally with the fem, the direct method of solution for pdes is considered in length.

Finally, the θ time stepping method is detailed, and the applicability of each of its time stepping methods are stated.

The rest of this thesis will apply the theory covered in this Chapter to the solution of one and two dimensional electrochemical systems.

CHAPTER 4
1-D FINITE ELEMENT MODEL

4.1 Introduction

In this chapter we apply the finite element method, detailed in chapter 3, to the one dimensional macrohomogeneous equations which were covered in chapter 2 for a complete lead-acid battery system. The governing equations including initial and boundary conditions are given for the positive and negative plates, the separator, and the electrolyte reservoir. The equations are then put into a Galerkin formulation and discretised into an elemental residual and Jacobian matrix with the appropriate trial functions. The resultant non-symmetric banded sparse matrix is solved with a conjugent gradient method.

The following formulation is not necessarily the only or best way of formulating the equation set. However, the formulation used to examine and investigate as many similarities as possible between the finite element solution method and those previously published utilising finite differences.

4.2 The Mathematical Model

We consider the one dimensional lead-acid cell as shown in figure 4.1. Each electrode is an electrically conductive porous matrix filled with concentrated H_2SO_4. The sulphuric acid is assumed to be a binary electrolyte dissociating completely into H^+ and HSO_4^-. During discharge, electrolyte is forced out of the electrode pores as they fill with lead sulphate. The convective effects associated with this mechanism has been investigated previously in one-dimensional models, [Gu 87], and are not significant. Hence convection is ignored. Isothermal conditions apply.

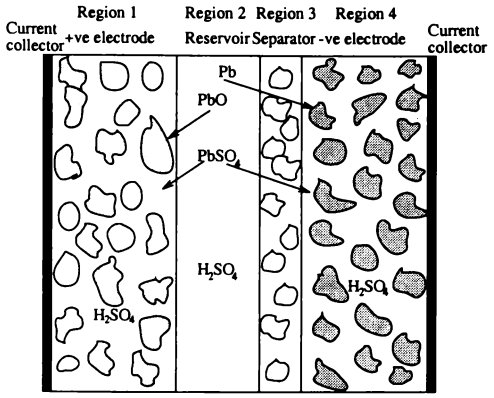

Figure 4.1: One-dimensional macro-homogeneous model of a lead-acid cell

The overall discharge reaction of the positive electrode is:

$$PbO_{2(solid)} + 3H^+ + HSO_4^- + 2e^- \underset{\text{charge}}{\overset{\text{discharge}}{\rightleftharpoons}} PbSO_{4(solid)} + 2H_2O \tag{4.1}$$

At the same time the discharge reaction of the negative electrode is:

$$Pb_{(solid)} + HSO_4^- \underset{\text{charge}}{\overset{\text{discharge}}{\rightleftharpoons}} PbSO_{4(solid)} + H^+ + 2e^- \tag{4.2}$$

PbO_2 and Pb are converted into $PbSO_4$ during discharge, and the reverse reactions occur during recharge. Note that water is formed during discharge in the positive electrode, and that $PbSO_4$ has a larger molar volume than either Pb or PbO_2.

4.2.1 The Governing Equations

The governing differential equations from Chapter 2 for the electrochemical cell show in figure (4.1) are:

Rate of porosity variation:

$$\frac{\partial \epsilon}{\partial t} - K_1 \frac{\partial i_{soln}}{\partial x} = 0 \tag{4.3}$$

Mass transport of the H_2SO_4 electrolyte:

$$\epsilon(x)\frac{\partial c}{\partial t} - \frac{\partial}{\partial x}\left(D_{eff}(x,c)\frac{\partial c}{\partial x}\right) + (K_2 + c(x)K_1)\frac{\partial i_{soln}}{\partial x} = 0 \tag{4.4}$$

A modified Ohm's law for the solution phase:

$$c(x)i_{soln}(x) + \kappa_{eff}(x,c)c(x)\frac{\partial \phi_{soln}}{\partial x} - \kappa_{eff}(x,c)(1-2t_+^0)\frac{RT}{F}\frac{\partial c}{\partial x} = 0 \tag{4.5}$$

Divergence of current of Ohm's law for the solid phase:

$$\frac{\partial i_{soln}}{\partial x} - \frac{\partial}{\partial x}\left(\sigma_{eff}(x)\frac{\partial \phi_{solid}}{\partial x}\right) = 0 \tag{4.6}$$

Butler-Volmer equation describes the electrode's kinetics:

$$\frac{\partial i_{soln}}{\partial x} - A_a i_0 \left[e^{\frac{\alpha_a F}{RT}\eta} - e^{-\frac{\alpha_c F}{RT}\eta}\right] = 0 \tag{4.7}$$

In these equations, K_1 and K_2 are defined separately for the positive and negative electrodes:

$$K_1^{pos} = \frac{1}{2F}\left(\frac{M_{PbSO_4}}{\rho_{PbSO_4}} - \frac{M_{PbO_2}}{\rho_{PbO_2}}\right) \tag{4.8}$$

$$K_1^{neg} = -\frac{1}{2F}\left(\frac{M_{PbSO_4}}{\rho_{PbSO_4}} - \frac{M_{PbO}}{\rho_{PbO}}\right) \tag{4.9}$$

and

$$K_2^{neg} = -\frac{1}{2F}\left(1-2t_-^0\right) \tag{4.10}$$

$$K_2^{pos} = \frac{1}{2F}\left(2t_+^0 - 3\right) \tag{4.11}$$

K_1 accounts for the volumetric change per mole of active material converted in each electrode and K_2 accounts for the volumetric ion production or consumption rate.

The electro-active interfacial area per unit volume, A_a, is electrode specific and is defined for discharge as:

$$A_a^{pos} = a_{max}^{pos}(1-U)^{\zeta pos} \qquad A_a^{neg} = a_{max}^{neg}(1-U)^{\zeta neg} \tag{4.12}$$

and for charge as:

$$A_a^{pos} = a_{max}^{pos}(U)^{\zeta pos} \qquad A_a^{neg} = a_{max}^{neg}(U)^{\zeta neg} \tag{4.13}$$

where ζi are exponents for the charge dependence of the specific active surface area.

U is the electrode utilisation and is defined by:

$$U = \frac{1}{Q_{max}} \int_0^1 j dt \tag{4.14}$$

The exchange current densities for the positive and negative electrodes are:

$$i_0^{pos} = i_0^{ref,pos} \left(\frac{c}{c_{ref}} \right)^{\gamma pos} \tag{4.15}$$

$$i_0^{neg} = i_0^{ref,neg} \left(\frac{c}{c_{ref}} \right)^{\gamma neg} \tag{4.16}$$

where γi are exponents for the concentration dependence of the exchange current density.

The electrode overpotential, η is defined for both electrodes as:

$$\eta_{pos} = \phi_{soln} - \phi_{soln} - \Delta U_{\mathrm{PbO_2}} \tag{4.17}$$

and

$$\eta_{neg} = \phi_{soln} - \phi_{soln} \tag{4.18}$$

ΔU is the thermodynamic open circuit cell potential. It can either be assumed to be a constant, or can be specified as a function of electrolyte concentration and temperature (Appendix A.6).

The parameters α_a and α_c are the anodic and cathodic transfer coefficients. Equation 4.7 is a Butler-Volmer type equation and determines the transfer current which drives the electrochemical reaction and determines the relationship between the solid and solution phases. Obviously the transfer current density equals zero in the reservoir and separator regions.

The conductivity of the electrolyte and the solid matrix, and the diffusivity of the electrolyte change with varying porosities. This is accounted for with the

following Bruggeman-type [Mer 62] relations, i.e.

$$\sigma_{eff}(x) = \sigma(x)\epsilon^{exm}(x), \quad \kappa_{eff}(x,c) = \kappa(x)\epsilon^{ex}(x), \tag{4.19}$$

$$\text{and} \qquad D_{eff}(x,c) = D(x,c)\epsilon^{ex}(x)$$

Note that the coefficients $\kappa(x,c)$, and $D(x,c)$ can depend on concentration. Refer to Appendix A.6 for their representative equations.

The porosity is calculated from the divergence of the solution current, $\frac{\partial i_{soln}}{\partial x}$, at each iteration.

The Reservoir and Separator Regions

In the reservoir and separator regions (see Figure 4.1), the divergence of current is zero, i.e.

$$\frac{\partial i_{soln}}{\partial x} = 0 \tag{4.20}$$

Equations (4.3) - (4.7) are modified in the following manner:

The porosity is obviously constant in these regions, i.e.

$$\epsilon = \epsilon_{sep} = 1 \quad \text{and} \quad \epsilon = \epsilon_{res} \tag{4.21}$$

Equation (4.4) still applies, but without the current divergence term $\frac{\partial i_{soln}}{\partial x}$.

The solid phase potential to zero, reflecting the physics of the system, i.e. equation (4.6) becomes:

$$\phi_{solid} = 0 \tag{4.22}$$

Obviously ions are not produced or used in these regions, hence in equations (4.20) to (4.7) we set:

$$\frac{\partial i_{soln}}{\partial x} = 0 \tag{4.23}$$

4.2.2 Initial and Boundary Conditions

The porosity, ϵ, of the system and the sulphuric acid concentration, c, are time dependent and require initial conditions, ϵ_0 and c_0.

In this section we use physical reasoning to arrive at the appropriate boundary conditions. Later we will see the boundary conditions evolve naturally from the weak formulation of the partial differential equations.

We take the external boundary conditions of the model to be the centres of the positive and negative electrodes. This allows us to exploit symmetry for two of the boundary conditions, i.e.

$$\frac{\partial c}{\partial x} = 0 \tag{4.24}$$

$$\frac{\partial \phi_{soln}}{\partial x} = 0 \tag{4.25}$$

At the centre of the electrodes all the current in the solution has been transferred into the solid phase, i.e.

$$i_{soln} = 0 \tag{4.26}$$

For constant current discharging and charging, the current enters and leaves the cell through the grid collectors. If we take the divergence of the solid current for the positive electrode we get at the centre of the electrode:

$$\sigma_{eff}^{pos} \frac{\partial \phi_{solid}}{\partial x} = I_{tot} \tag{4.27}$$

where I_{tot} is the total applied current density. Positive values of I_{tot} correspond to discharge conditions, and negative values to charging conditions.

Similarly we can use the same argument for the negative electrode, however, we need to assign the solid potential to zero to obtain a particular solution, thus:

$$\phi_{solid} = 0 \tag{4.28}$$

That is, we assign a reference potential of 0 volts to the negative electrode at $x = 0$.

For constant potential discharging and charging we set the solid potential a predetermined value at the centre of the positive electrode.

$$\phi_{solid} = V \tag{4.29}$$

4.3 Method of Solution

Equations (4.3) to (4.7) are a coupled set of nonlinear partial differential equations. As such we seek a numerical solution. Equations (4.4) to (4.7) are solved for c, i_{soln}, ϕ_{solid}, and ϕ_{soln} using finite elements in what is called, in computational fluid dynamics, the integrated method [Cuvelier 85]. The equations are linearised with a Newton-Raphson technique.

The boundary conditions (4.24) to (4.28) homogeneous, except for either equation (4.27) or (4.29) which are non-homogeneous Neuman and Dirchelet boundary conditions respectively. Equation (4.24) specifies either constant current discharging or charging, and is applied at the centre of the positive electrode. Equation (4.29) specifies either constant potential discharging or charging and is again applied at the centre of the positive electrode.

The porosity, ϵ, is solved from the solution of the coupled equations using equation (4.3) from the previous iteration. As such, it does not appear explicitly in the set of coupled equations, i.e. it is solved from the divergence of current from the previous iteration, and the porosity is updated for the model to be solved in the next step.

The general method as outlined in the previous chapter is the method of weighted residuals. The particular weighted residual method used is the Galerkin method (i.e., the basis functions of the approximation are the same as the test functions). It will have the following outline:

multiply the equations by arbitrary test functions. φ_i;

integrate over the domain Ω;

apply Green's formula if necessary;

substitute the boundary conditions.

4.3.1 Galerkin Formulation of the Residuals

Firstly, we multiply equations (4.4) to (4.7) by arbitrary test functions and integrate over the domain, and apply Green's formula.

The residual for material balance for H_2SO_4 (4.4) is:

$$\begin{aligned} R(x,t;a) &= \int^{(e)} \varphi_i^{(e)} \left[\epsilon(x) \frac{\partial \tilde{c}(x,t;a)}{\partial t} - \frac{\partial}{\partial x} \left(D_{eff}(x) \frac{\partial \tilde{c}(x,t;a)}{\partial x} \right) \right. \\ &\quad \left. + (K_2 + c(x)K_1) \frac{\partial \tilde{i}_{soln}(x,t;a)}{\partial x} \right] dx \\ &= 0 \end{aligned} \tag{4.30}$$

Integrating the second order term by parts gives:

$$\begin{aligned} R(x,t;a) &= \int^{(e)} \varphi_i^{(e)} \epsilon(x) \frac{\partial \tilde{c}(x,t;a)}{\partial t} dx + \int^{(e)} \frac{\partial \varphi_i^{(e)}}{\partial x} D_{eff}(x) \frac{\partial \tilde{c}(x,t;a)}{\partial x} dx \\ &\quad + \left[\varphi_i \left(-D_{eff} \frac{\partial \tilde{c}(x,t;a)}{\partial x} \right) \right]_{x_a}^{x_b} + \int^{(e)} \varphi_i^{(e)} (K_2 + c(x)K_1) \frac{\partial \tilde{i}_{soln}(x,t;a)}{\partial x} \\ &= 0 \end{aligned} \tag{4.31}$$

The residual for ohm's law in solution (4.5) is:

$$\begin{aligned} R(x,t;a) &= \int^{(e)} \varphi_i^{(e)} \left[\tilde{i}_{soln}(x,t;a) c(x) + c(x) \kappa_{eff}(x,c) \frac{\partial \tilde{\phi}_{soln}(x,t;a)}{\partial x} \right. \\ &\quad \left. - \kappa_{eff}(x,c) \frac{RT}{F} (1 - 2t_+^0) \frac{\partial (\tilde{c}(x,t;a))}{\partial x} \right] dx \\ &= 0 \end{aligned} \tag{4.32}$$

The residual for the divergence of current (4.6) is:

$$R(x,t;a) = \int^{(e)} \varphi_i^{(e)} \left[\frac{\partial \tilde{i}_{soln}(x,t;a)}{\partial x} - \frac{\partial}{\partial x} \left(\sigma_{eff}(x) \frac{\partial \phi_{solid}(x,t;a)}{\partial x} \right) \right] dx = 0 \tag{4.33}$$

Integrating the second order term by parts gives:

$$\begin{aligned} R(x,t;a) &= \int^{(e)} \varphi_i^{(e)} \frac{\partial \tilde{i}_{soln}(x,t;a)}{\partial x} dx + \int^{(e)} \frac{\partial \varphi_i^{(e)}(x)}{\partial x} \sigma_{eff}(x) \frac{\partial \tilde{\phi}_{solid}(x,t;a)}{\partial x} dx \\ &\quad + \left[\varphi_i \left(-\sigma_{eff} \frac{\partial \tilde{\phi}_{solid}(x,t;a)}{\partial x} \right) \right]_{x_a}^{x_b} \\ &= 0 \end{aligned} \tag{4.34}$$

The residual for electrode kinetics (4.7) is:

$$R(x,t;a) = \int^{(e)} \varphi_i^{(e)} \left[\frac{\partial \tilde{i}_{soln}(x,t;a)}{\partial x} - A_a i_0 \left(e^{\frac{\alpha_a F}{RT}\eta} - e^{-\frac{\alpha_a F}{RT}\eta} \right) \right] dx = 0 \tag{4.35}$$

This forms the set of the weak formulation of equations (4.4) to (4.7).

4.3.2 Trial Functions for the Governing Equations

We seek trial solutions for the previously defined unknowns which can be composed of any of the one-dimensional basis functions defined in Chapter 3. Note that for the respective basis function derivatives, the partial derivatives of the trial functions with respect to both x and t, revert to ordinary derivatives.

$$\tilde{c}^{(e)}(x,t;a) = \sum_{j=1}^{n} c_j(t) \varphi_j^{(e)}(x) \tag{4.36}$$

$$\tilde{i}_{soln}^{(e)}(x,t;a) = \sum_{j=1}^{n} i_{soln,j}(t) \varphi_j^{(e)}(x) \tag{4.37}$$

$$\tilde{\phi}_{soln}^{(e)}(x,t;a) = \sum_{j=1}^{n} \phi_{soln,j}(t) \varphi_j^{(e)}(x) \tag{4.38}$$

$$\tilde{\phi}_{solid}^{(e)}(x,t;a) = \sum_{j=1}^{n} \phi_{solid,j}(t) \varphi_j^{(e)}(x) \tag{4.39}$$

We can also define basis functions for our other variables, ϵ, κ, σ:

$$\tilde{\epsilon}^{(e)}(x,t;a) = \sum_{j=1}^{n} \epsilon_j(t) \varphi_j^{(e)}(x) \tag{4.40}$$

$$\tilde{\kappa}^{(e)}_{soln}(x,t;a) = \sum_{j=1}^{n} \kappa_{soln,j}(t)\varphi^{(e)}_j(x) \tag{4.41}$$

$$\tilde{\sigma}^{(e)}_{soln}(x,t;a) = \sum_{j=1}^{n} \sigma_{soln,j}(t)\varphi^{(e)}_j(x) \tag{4.42}$$

Substituting the respective trial functions and derivatives of the trial functions into their residual equations gives:

Material balance:

$$\begin{aligned}
&\sum_{j=1}^{n} \int^{(e)} \varphi^{(e)}_i(x)\varphi^{(e)}_j(x)\epsilon_j(t)\varphi^{(e)}_j(x)\frac{dc_j(t)}{dt}dx \\
&+\sum_{j=1}^{n} \int^{(e)} \frac{d\varphi^{e}_i(x)}{dx}\varphi^{(e)}_j(x)D_{eff,j}(t)\frac{d\varphi^{(e)}_j(x)}{dx}c_j(t)dx \\
&+\sum_{j=1}^{n} \int^{(e)} \varphi^{(e)}_i(x)\left(K_2 + \varphi^{(e)}_i(x)\varphi^{(e)}_j(x)c_j(t)K_1\right)\frac{d\varphi^{(e)}_j(x)}{dx}i_{soln,j}(t)dx \\
&+\left[\left(-D_{eff}\frac{\partial\tilde{c}(x,t;a)}{\partial x}\right)\varphi_i\right]_{x_a}^{x_b} \\
&= 0
\end{aligned} \tag{4.43}$$

Ohm's law in solution:

$$\begin{aligned}
&\sum_{j=1}^{n} \int^{(e)} \varphi^{(e)}_j(x)c_j(t)\varphi^{(e)}_j(x)i_{soln}(x,t)dx \\
&+\sum_{j=1}^{n} \int^{(e)} \varphi^{(e)}_j(x)c_j(t)\varphi^{(e)}_j(x)\kappa_{eff,j}(t)\frac{d\varphi^{(e)}_i(x)}{dx}\varphi^{(e)}_j(x)\phi_{soln,j}(t)dx \\
&-\sum_{j=1}^{n} \int^{(e)} \varphi^{(e)}_j(x)\kappa_{eff,j}(t)(1-2t^0_+)\frac{RT}{F}\frac{d\varphi^{(e)}_i(x)}{dx}\varphi^{(e)}_j(x)c_j(t)dx \\
&= 0
\end{aligned} \tag{4.44}$$

Divergence of current:

$$\sum_{j=1}^{n} \int^{(e)} \varphi^{(e)}_i(x)\frac{d\varphi_j(x)}{dx}i_{soln,j}(t)dx$$

$$+\sum_{j=1}^{n}\int^{(e)}\frac{d\varphi_i^{(e)}(x)}{dx}\varphi_j^{(e)}(x)\sigma_{eff,j}(t)\frac{d\varphi_j(x)}{dx}\phi_{solid,j}(t)dx$$
$$+\left[\left(-\sigma_{eff}\frac{\partial\tilde{\phi}_{solid}(x,t;a)}{\partial x}\right)\varphi_i\right]_{x_a}^{x_b}=0 \tag{4.45}$$

Electrode kinetics:

$$\int^{(e)}\sum_{j=1}^{n}\frac{d\varphi_j^{(e)}(x)}{dx}\varphi_i^{(e)}(x)i_{soln,j}(t)dx-\int^{(e)}A_a i_0\left(e^{\frac{\alpha_a F}{RT}\eta}-e^{-\frac{\alpha_a F}{RT}\eta}\right)\varphi_i^{(e)}dx=0 \tag{4.46}$$

Rewriting the coupled equations (4.43) to (4.46) in a matrix system of nonlinear algebraic equations gives:

$$\begin{bmatrix} C_{1,1} & 0 & 0 & 0\\ 0 & 0 & 0 & 0\\ 0 & 0 & 0 & 0\\ 0 & 0 & 0 & 0\end{bmatrix}\begin{Bmatrix}\dot{c}\\ \dot{i}_{soln}\\ \dot{\phi}_{solid}\\ \dot{\phi}_{soln}\end{Bmatrix}+\begin{bmatrix} K_{1,1} & U_{1,2} & 0 & 0\\ U_{2,1} & 0 & 0 & U_{2,4}\\ 0 & U_{3,2} & K_{3,3} & 0\\ 0 & U_{4,2} & 0 & 0\end{bmatrix}\begin{Bmatrix}c\\ i_{soln}\\ \phi_{solid}\\ \phi_{soln}\end{Bmatrix}=\begin{Bmatrix}F_1(t)\\ F_2(c,i_{soln},t)\\ F_3(t)\\ F_4(\phi_{sold},\phi_{soln},t)\end{Bmatrix} \tag{4.47}$$

where the subscript notation refers to the row and column number in the $[K]$ and $[U]$ matrices. This can be further reduced and put into a single equation for the residual:

$$\{r^k(x,t;a)\}=[C]^{(e)}\left\{\frac{dw(t)}{dt}\right\}+([K]^{(e)}+[U]^{(e)})\{w(t)\}-\{F(t)\}^{(e)}=0 \tag{4.48}$$

where

$$[C_{ij}]=\sum_e\int^{(e)}\begin{bmatrix}\epsilon(t)\varphi_i^{(e)}\varphi_j^{(e)} & 0 & 0 & 0\\ 0 & 0 & 0 & 0\\ 0 & 0 & 0 & 0\\ 0 & 0 & 0 & 0\end{bmatrix} \tag{4.49}$$

$$[K_{ij}]=\sum_e\int^{(e)}\begin{bmatrix}\frac{d\varphi_i^{(e)}}{dx}\varphi_j^{(e)}D_{eff,j}(t)\frac{d\varphi_j^{(e)}}{dx} & 0 & 0 & 0\\ 0 & 0 & 0 & 0\\ 0 & 0 & \frac{d\varphi_i^{(e)}}{dx}\varphi_j^{(e)}\sigma_{eff,j}(t)\frac{d\varphi_j}{dx} & 0\\ 0 & 0 & 0 & 0\end{bmatrix} \tag{4.50}$$

$$[U_{ij}]=\sum_e \int^{(e)} \begin{bmatrix} 0 & \left(K_2+\varphi_j^{(e)} c_j(t) K_1\right) \frac{d\varphi_j^{(e)}}{dx} \varphi_i^{(e)} & 0 & 0 \\ -\varphi_j^{(e)} \kappa_{eff,j}(t)(1-2t_+^0) \frac{RT}{F} \frac{d\varphi_j^{(e)}}{dx} \varphi_j^{(e)} & 0 & 0 & \varphi_j^{(e)} c_j(t) \varphi_j^{(e)} \kappa_{eff,j}(t) \frac{d\varphi_j^{(e)}}{dx} \varphi_j^{(e)} \\ 0 & \frac{d\varphi_j^{(e)}}{dx} \varphi_i^{(e)} & 0 & 0 \\ 0 & \frac{d\varphi_j^{(e)}}{dx} \varphi_i^{(e)} & 0 & 0 \end{bmatrix}$$

(4.51)

$$\{F_i(t)\} = \{F(t)_\Omega^i\} + \{F_i(t)_{\Gamma,1}\} + \{F_i(t)_{\Gamma,2}\} \tag{4.52}$$

where the subscript Γ_1 denotes terms arising from the Dirichlet boundary conditions, and the subscript Γ_2, are those terms arising from Neuman boundary conditions.

$$\{F_i(t)_\Omega\} = \sum_e \int^{(e)} \begin{Bmatrix} 0 \\ \varphi_j^{(e)} c_j(t) i_{soln}(x,t;a) \varphi_i^{(e)} \\ 0 \\ -A_a i_0 \left(e^{\frac{\alpha_a F}{RT}\eta} - e^{-\frac{\alpha_a F}{RT}\eta}\right) \varphi_i^{(e)} \end{Bmatrix} \tag{4.53}$$

$$\{F_i(t)_\Gamma\} = \begin{Bmatrix} f_{mat\ bal,\Gamma} \\ f_{ohm\ sol,\Gamma} \\ f_{\nabla i_{soln},\Gamma} \\ f_{kin,\Gamma} \end{Bmatrix} \tag{4.54}$$

$$\{w(t)_j\} = \begin{Bmatrix} c_j(t) \\ i_{soln,j}(t) \\ \phi_{solid,j}(t) \\ \phi_{soln,j}(t) \end{Bmatrix} \tag{4.55}$$

The Jacobian matrix of the matrix equation (4.48) is calculated from:

$$[J^k(w)] = \frac{\partial\{r^k(w)\}}{\partial\{w\}} \tag{4.56}$$

and is relatively straight forward for the set of equations. The Jacobian matrix is:

$$[J(w)] = \sum_e \int^{(e)} \begin{bmatrix} K_{1,2} & U_{1,2} & 0 & 0 \\ U_{1,1} - \frac{dF_2}{dc} & -\frac{dF_2}{di_{soln}} & 0 & U_{2,2} \\ 0 & 0 & \frac{d\varphi_i^{(e)}}{dx} & 0 \\ 0 & 0 & -\frac{dF_2}{d\phi_{solid}} & -\frac{dF_2}{d\phi_{soln}} \end{bmatrix} \tag{4.57}$$

The non-linear algebraic equations can now be linearised with standard or modified Newton iteration, as explained in Chapter 3. The standard Newton-Raphson linearisation iteration has the form:

$$[J^k(w)]\ \left(\{w^{k+1}\} - \{w^k\}\right)\ =\ -\{r^k(w)\} \tag{4.58}$$

where k denotes the number of the iteration.

In summary, the model incorporates all the material properties and functions. The non-linear equations are linearised with a Newton-Raphson algorithm.

4.4 Remarks

4.4.1 Necessary Conditions for the Elements

We are solving for four functions, c, i_{soln}, ϕ_{solid}, and ϕ_{soln} using the finite element technique. The porosity, ϵ, is solved from the previous iteration from equation (4.3).

In the Galerkin equations, c and ϕ_{solid} appear as first order derivatives. This means that the basis functions must be continuously differentiable in each element and continuous in the whole domain, Ω.

The basis functions for i_{soln} and ϕ_{soln} are not differentiated in the Galerkin equations. These basis functions have to be continuous in each element, but in the domain Ω they are allowed to be discontinuous. They must be integrable. Once again this poses no problems as ϕ_{soln} is continuous throughout the domain.

The conditions for the basis functions of i_{soln} and ϕ_{soln} are weaker than the conditions for the basis functions of c and ϕ_{solid}. An element which satisfies the above requirements is said to be conforming.

4.4.2 External Boundary Conditions

All the external boundary conditions are homogeneous, except for the solid phase potential which has a non-homogeneous boundary condition at the centre of

the positive electrode. This term occurs naturally in the formulation of the weak statement and lets the model be charged or discharged at constant current.

4.4.3 Interfacial Boundary Conditions

The interfaces of concern are between the electrode/separator, the separator/electrolyte and the /electrolyte/electrode. The separator/electrolyte interface poses no problems; we simply adjust the porosities for each region and make sure the interface exists on adjoining nodes.

For the electrode/separator interface and electrode/electrolyte regions we need to check the continuity of first order terms for ϕ_{solid} and c. Both i_{soln} and ϕ_{soln} are weaker and we only require continuity inside the element and integrability. This poses no problems at the interfaces whatsoever.

The boundary term for the weak statement of the solid phase potential laplacian, $\frac{\partial}{\partial x}(\kappa(x)\frac{\partial \phi_{solid}}{\partial x})$, needs to be satisfied for the electrode separator/electrolyte interfaces. Fortunately the boundary term is naturally satisfied with the homogeneous boundary term, $\frac{\partial \phi_{solid}}{\partial x} = 0$, arising from the electrode regions, and $\phi_{solid} = 0$ in the separator and electrolyte regions. Whence the boundary term in the electrode region is satisfied.

The concentration c is continuous throughout the model and Inter-element continuity is naturally satisfied.

4.5 Numerical Results

In this section we compare results generated by the one-dimensional finite element model with published data from the finite difference models of Gu [Gu 87] and Nguyen [Nguyen *et al* 90]. Gu's model has data for high rate discharges at both 25C and -18C, and low rate charging at 25C and -18C. It is a particularly rigorous test as it gives data for a discharge/rest/charge cycle. Nguyen's model is concerned with

a starved lead-acid cell at high rates of discharge. It uses concentration dependent coefficients.

The results presented used 60 linear elements evenly spaced over the modeled region. Mesh grading yielded some improvement in solution accuracy and hence time of solution (for less elements). However judicial care was needed as this caused spurious oscillations in the solution.

Parabolic elements yielded identical results for less elements in all cases, however the computational time was approximately the same for the utilised code. The time-stepping method utilised was the backward difference method, due to its stability, and hence ease of use. In all cases, extensive testing was conducted on the mesh and time interval in order to make sure that solution was not controlled by either. Linearisation for each time interval was deemed finished when the difference between two iterations was less than 10^{-6}.

4.5.1 Comparison with the Gu *et al* Model

Although Gu *et al*'s model incorporated convective flow in their model, they concluded that movement of electrolyte due to this mechanism does not usually represent a significant contribution to the net flux of sulphuric acid in the cell [Gu 87]. According to W. B. Gu, [Gu 97] Gu *et al*'s [Gu 87], model showed good agreement with General Motors' experimental data. The material properties used for the base conditions in the present finite element model are identical to Gu *et al*, and are summarised in Appendix A.2. Some of the individual input parameters are not physically realistic, but collectively produce realistic cell voltages. Gu *et al* assumed a constant concentration independent, reference lead electrode and a concentration independent conductivity, κ, and diffusion, D, coefficients. The electrodes do, however, exhibit temperature dependence.

Gu *et al* [Gu 87] modeled a one-dimensional lead-acid cell and studied the dynamic behavior of acid concentration, porosity, and state of charge of the cell

during discharge, rest and charge at -18C and 25C. Subsequently, Gu *et al* [Gu 97] published a more complex model that included a comparison of numerical results to validate their techniques. Data from both models are used to evaluate the accuracy of the finite element model.

Discharge

Figure 4.2 shows voltage profiles at -18C and 25C for a discharge of 340 $mAcm^{-2}$. The finite element results show excellent agreement with Gu *el al*'s model, [Gu 87] up to 90 seconds at 25C and throughout the discharge at -18C. The more rapid drop off of cell voltage in the finite element model can probably be attributed to the different methods used to calculate the coefficients for the kinetic term in the models. The finite element model calculates the state of charge at each time interval and adjusts the kinetics, in much the same way as Gu *et al* [Gu 97]. In fact the drop of cell voltage after 90 seconds seems to follow Gu *et al*'s model closely

Figure 4.3 shows the acid concentration profiles during a 340 $mAcm^{-2}$ discharge at both -18C and 25C. Again the results agree well with Gu *et al*'s model [Gu 87], at -18C. At 25C, the finite element model predicts a slightly higher acid concentration in the anode region. The predictions are very close to Gu *et al*'s model [Gu 97]. It is seen that all the electrolyte is used up in the cathode at 25C, this is responsible for the drop off in cell voltage as exhibited in Figure 4.2.

Figure 4.4 shows the electrode capacity profiles. Good agreement is seen between the models. As the capacity of the electrodes are calculated from the gradient solution current, this also implies that the present model reaction rates are almost identical to those of Gu *et al* [Gu 87].

Note, the profiles indicate that the electrodes are not very well utilised during high rate discharges at both -18C and 25C.

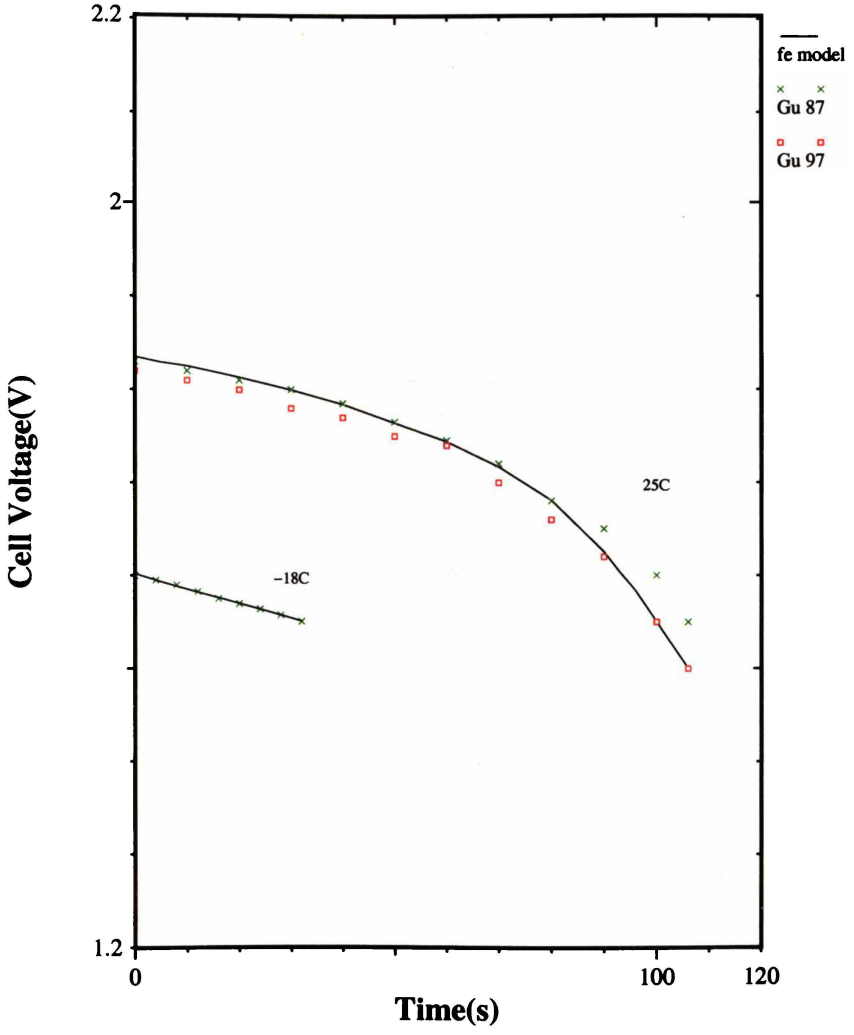

Figure 4.2: A comparison of predicted cell voltages vs time between the current model and previously published data for a 340 $mAcm^{-2}$.

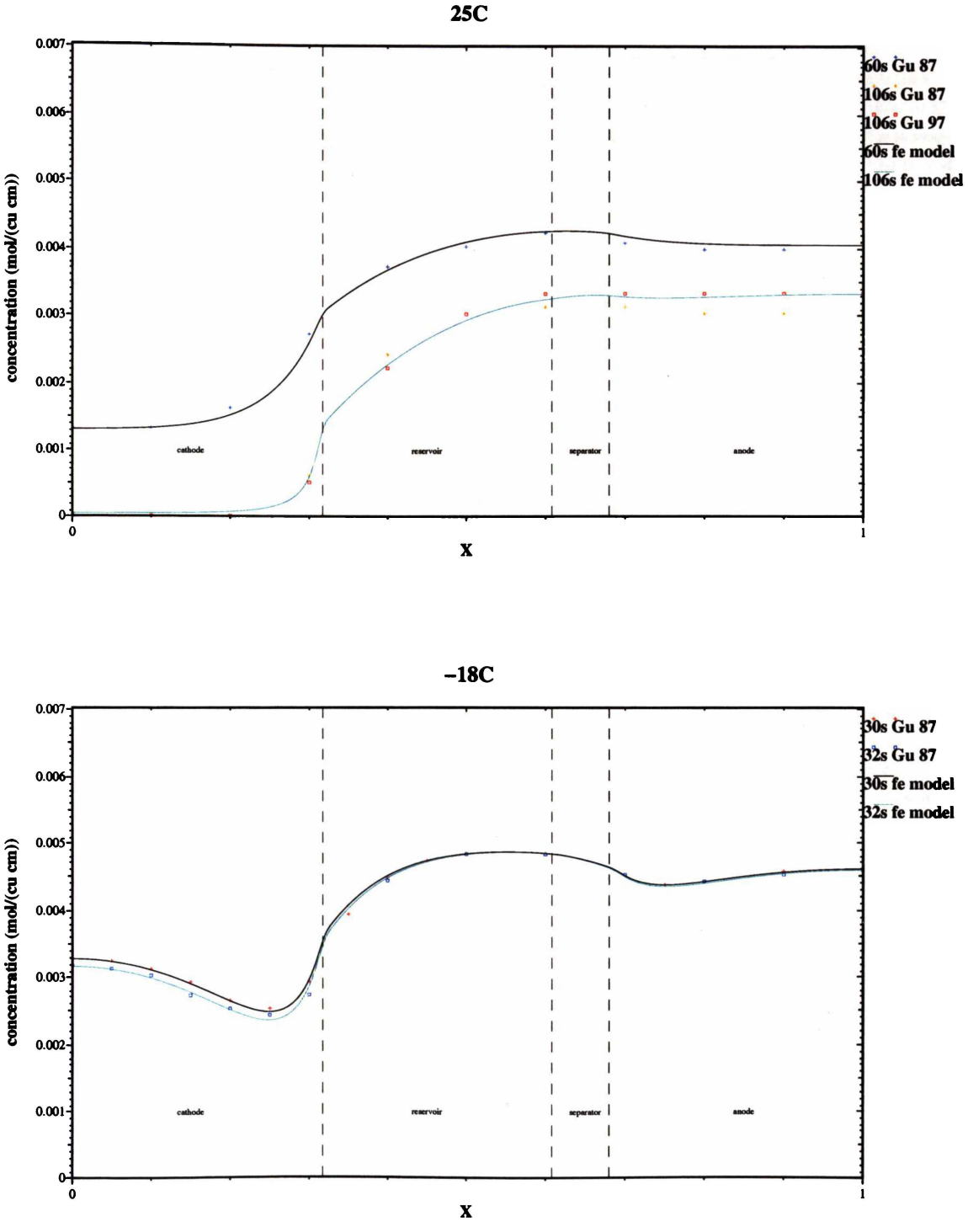

Figure 4.3: Acid concentration profiles for a 340 $mAcm^{-2}$ discharge at -18C and 25C.

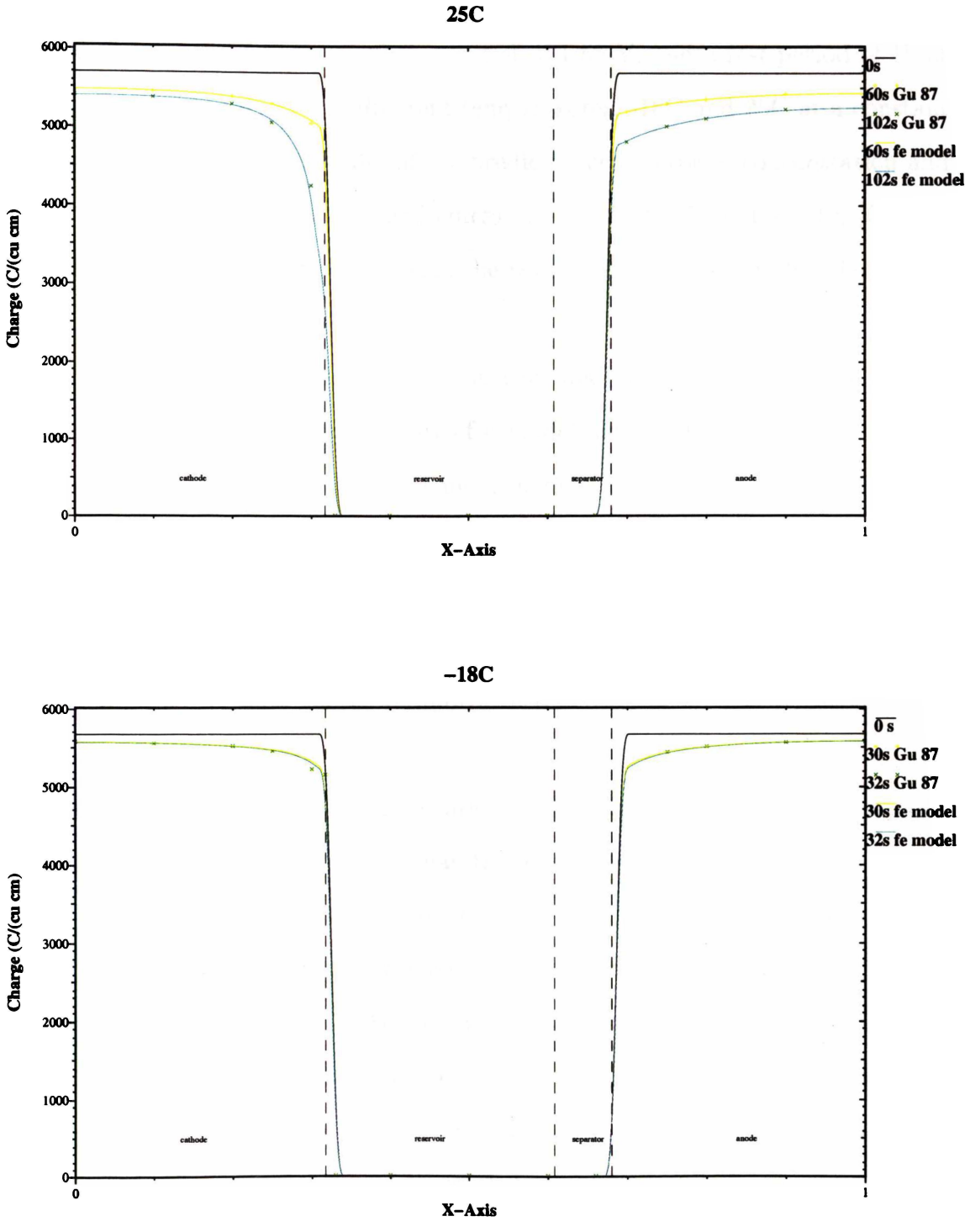

Figure 4.4: Profiles over time of the electrode capacity during a discharge at 340 $mAcm^{-2}$.

Charge

Charging is simulated according to the Gu *et al*'s model, [Gu 87]. Following a discharge at -18C and 340 $mAcm^{-2}$ to a cutoff of 1.55 V, and a rest period of 1h at -18C. The cell is charged at two different temperatures, -18C and 25C at a constant current of 20 $mAcm^{-2}$. The results of the predicted cell voltages, concentration and state of charge profiles are shown in Figures 4.5, 4.6 and 4.7. Gu *et al*'s, [Gu 87], data are plotted overtop. As can be seen, the results compare very well to Gu *et al*'s [Gu 87], and *et al*'s [Gu 97].

The high constant current discharge, rest, and slow constant current charge cycle is a stringent test on the accuracy of a model, and is thus a good test for the validity of the one-dimensional finite element model

Note in Figure 4.6 that the concentration of sulphuric acid is much more uniform after the 1 hour rest following discharge (refer Figure 4.3). This indicates that it is much more efficient to rest the cell before recharging.

In Figure 4.7, note the non-uniform distribution of charge across the electrodes.

Lead-acid batteries are usually charged under a constant potential with a current limit. Gu *et al* [Gu 87], stated that this could be achieved in their model by iterating on the applied charging current. Gu *et al* [Gu 97] were able to include a constant solid phase potential into their boundary conditions. This greatly simplifies and increases the speed of solution of the model. For the current finite element model, the constant current charge/discharge is included as a natural boundary condition of the finite element formulation, and a constant potential for charge/discharge is achieved readily by enforcing essential boundary conditions for the solid phase potential.

4.5.2 Comparison with the Nguyen *et al* Model

Nguyen *et al* [Nguyen *et al* 90] developed a one-dimensional macrohomogeneous model of the solid/liquid phases for a starved lead-acid battery. The model

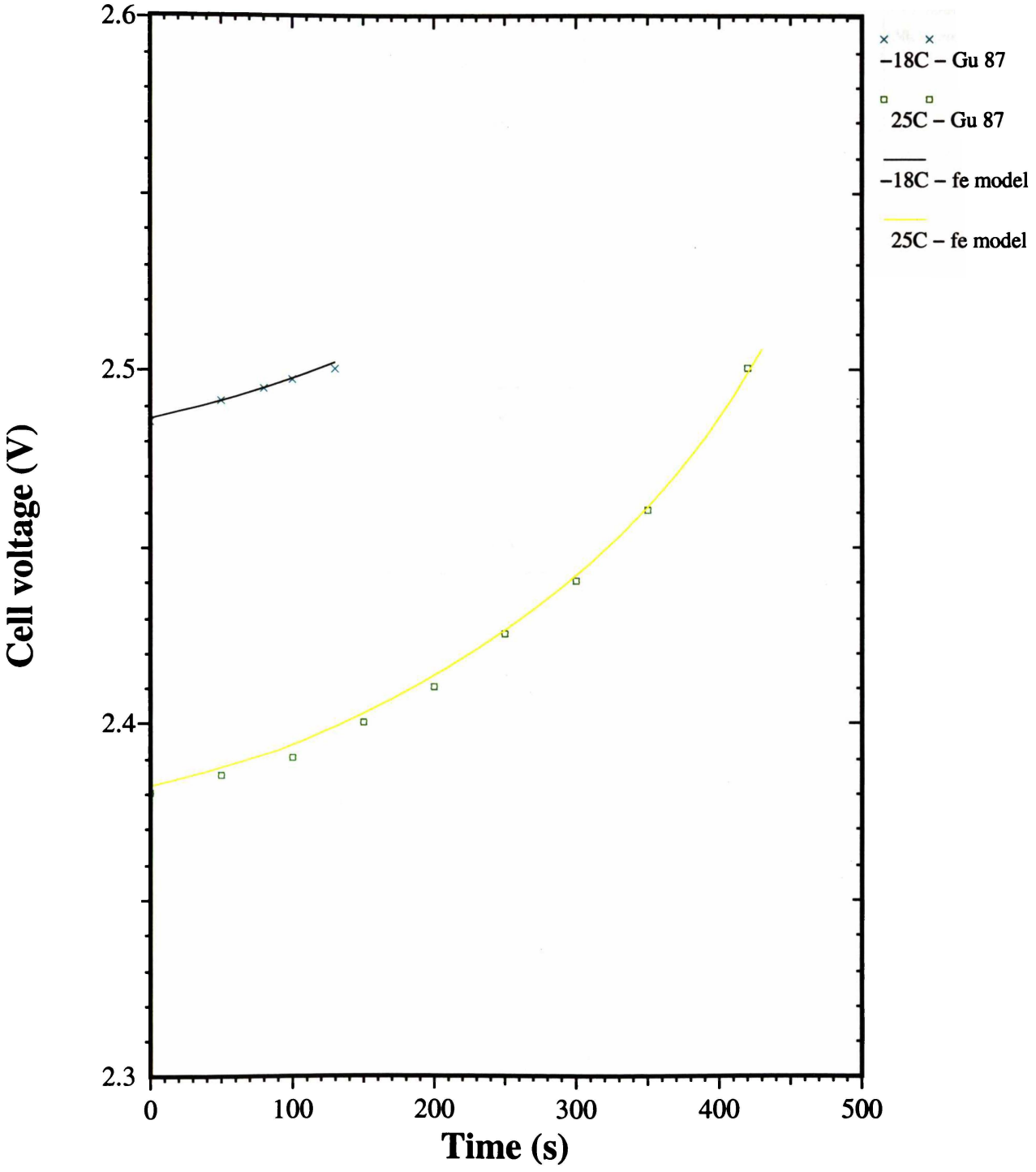

Figure 4.5: The cell voltage curves for a 20 $mAcm^{-2}$ charge at both -18C and 25C.

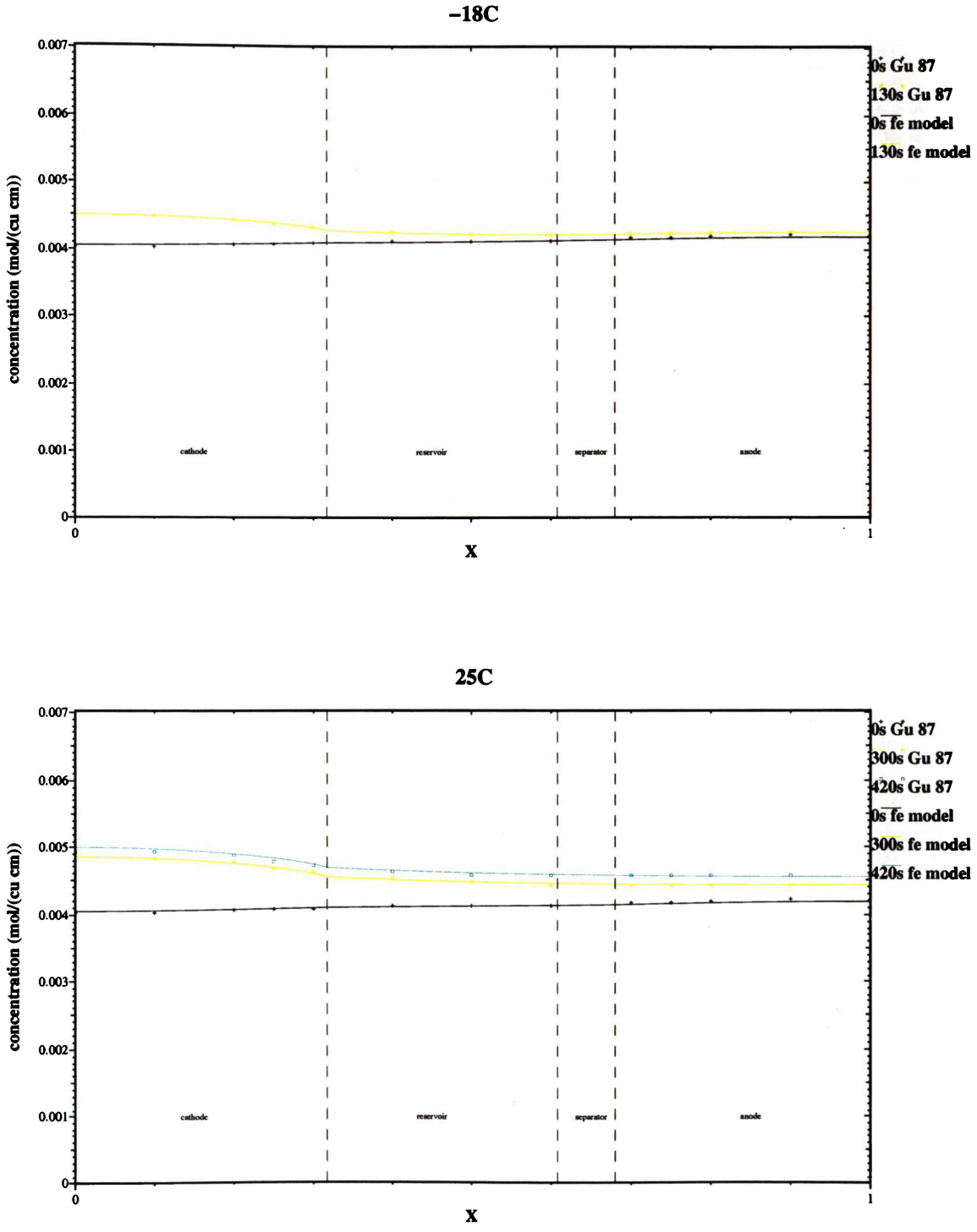

Figure 4.6: Acid concentration profiles for a 20 $mAcm^{-2}$ charge at -18C and 25C.

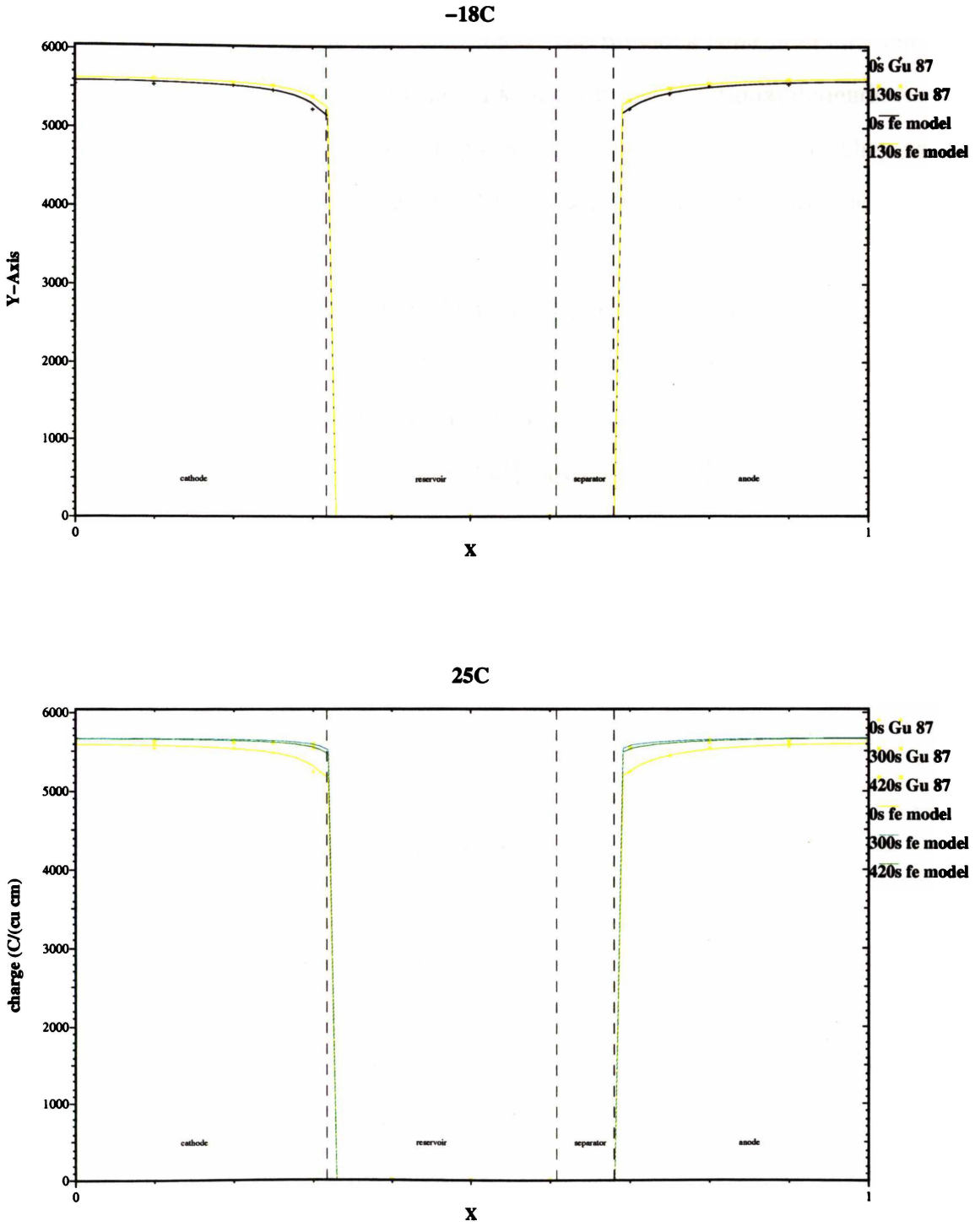

Figure 4.7: Profiles of the electrode capacity during a charge at 20 $mAcm^{-2}$ with time

assumes negligible convection and has a high rate of discharge. The coefficients D, κ, and ΔU_{PbO_2} depend on c, but are not explicitly formulated in terms of c. That is, they are calculated from the concentration at the previous time interval. This is modified in the current finite element model to include the functional dependence of these coefficients at each iteration as shown in equations (5.40) to (5.45) They were primarily concerned with the significance of the separator on the performance of the battery.

Nguyen *et al* modeled an equivalent battery at a high cold-cranking rate of 728 Amps at -18C on a battery with thirteen 13.9cm by 10.7cm plates in each cell. This equates to a discharge density of 408 $mAcm^{-2}$ per plate for the model. The material properties used are from Nguyen *et al* [Nguyen *et al* 90], and are summarised in Appendix A.3.

Figure 4.8 compares the results of the current finite element model with those of Nguyen *et al* for the electrolyte concentration profile. The results agree well for each time interval. The acid concentration is not limiting the electrochemical reaction for this set of conditions, however, the electrolyte consumption is more pronounced for the cathode.

Figure 4.9 compares the polarisation curves for the present model with that of Nguyen *et al.*

Figure 4.10 shows that the reaction rates from both models agree well. Note that the reaction profile is highly non-uniform (non-optimal) through both plates. The anode has the higher rate of reaction at the surface, but the cathode has the more uniform rate of reaction throughout the electrode. The reaction rate in the cathode varies more with time than in the anode, which is consistent with the polarisation curves.

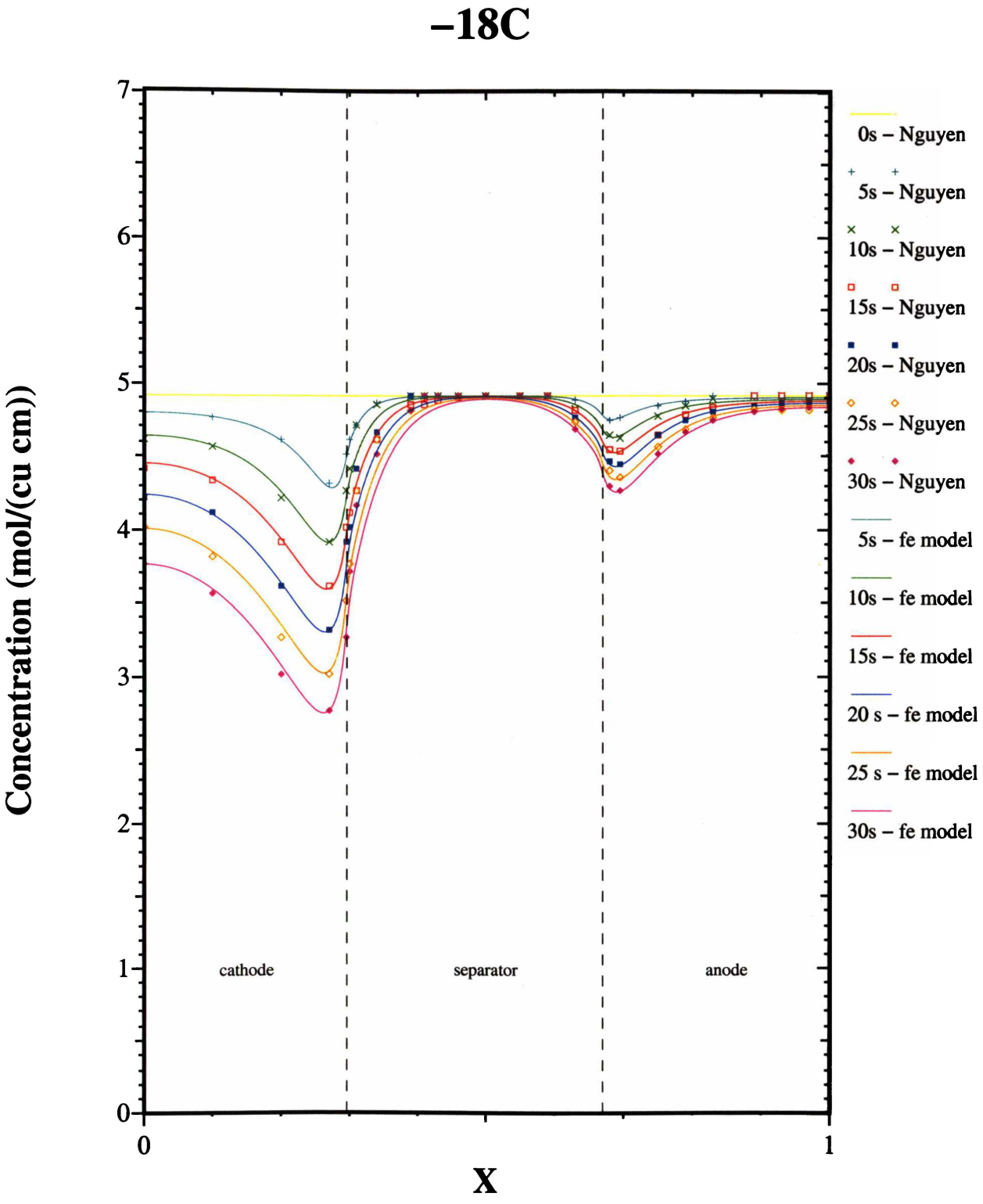

Figure 4.8: Electrolyte concentration profiles for 408 $mAcm^{-2}$ discharge at -18C. Profiles are at 5 second intervals. The comparison is between present finite element model and the Nguyen *et al* model [Nguyen *et al* 90].

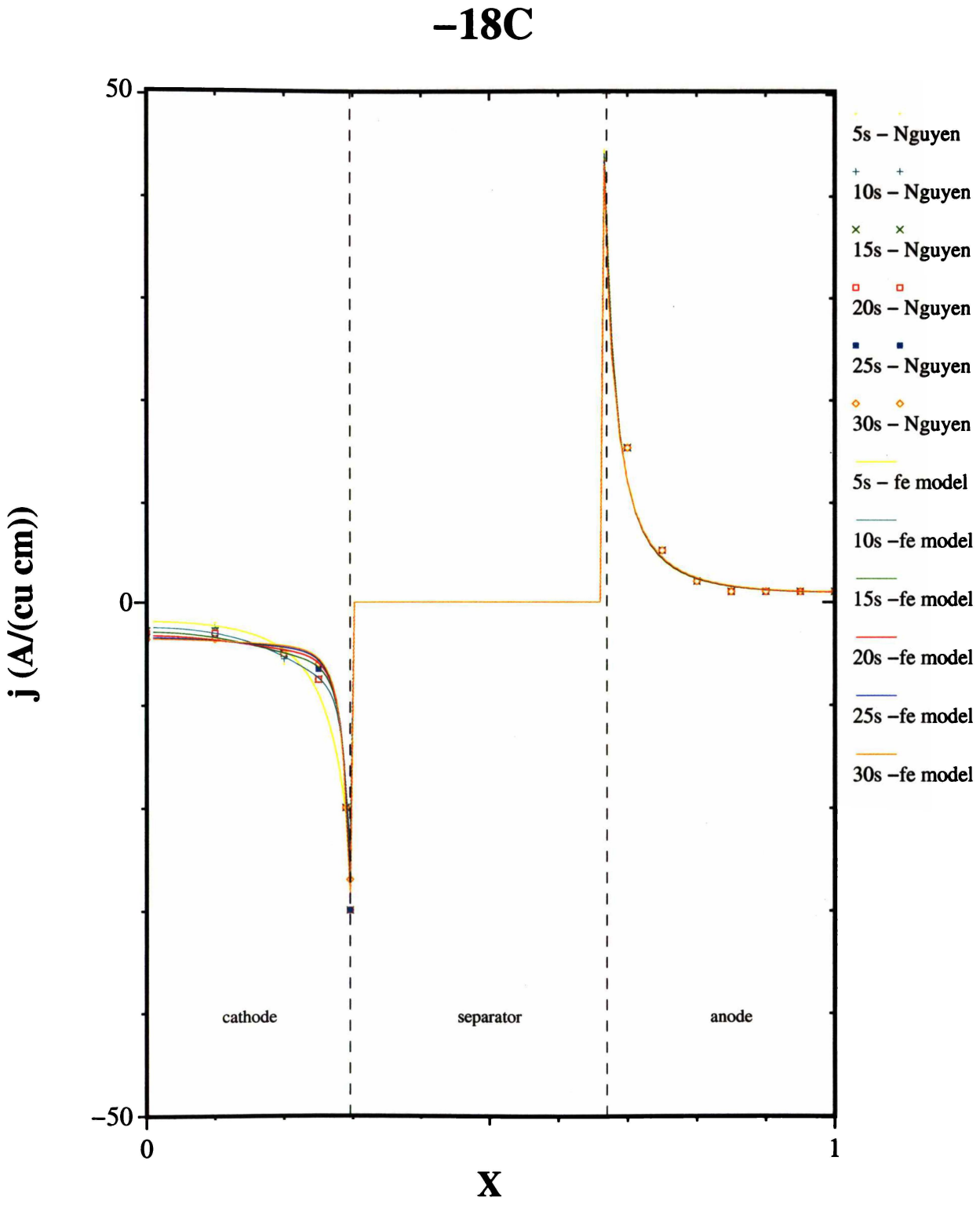

Figure 4.9: Electrode polarisation profiles for a 408 $mAcm^{-2}$ at -18C.

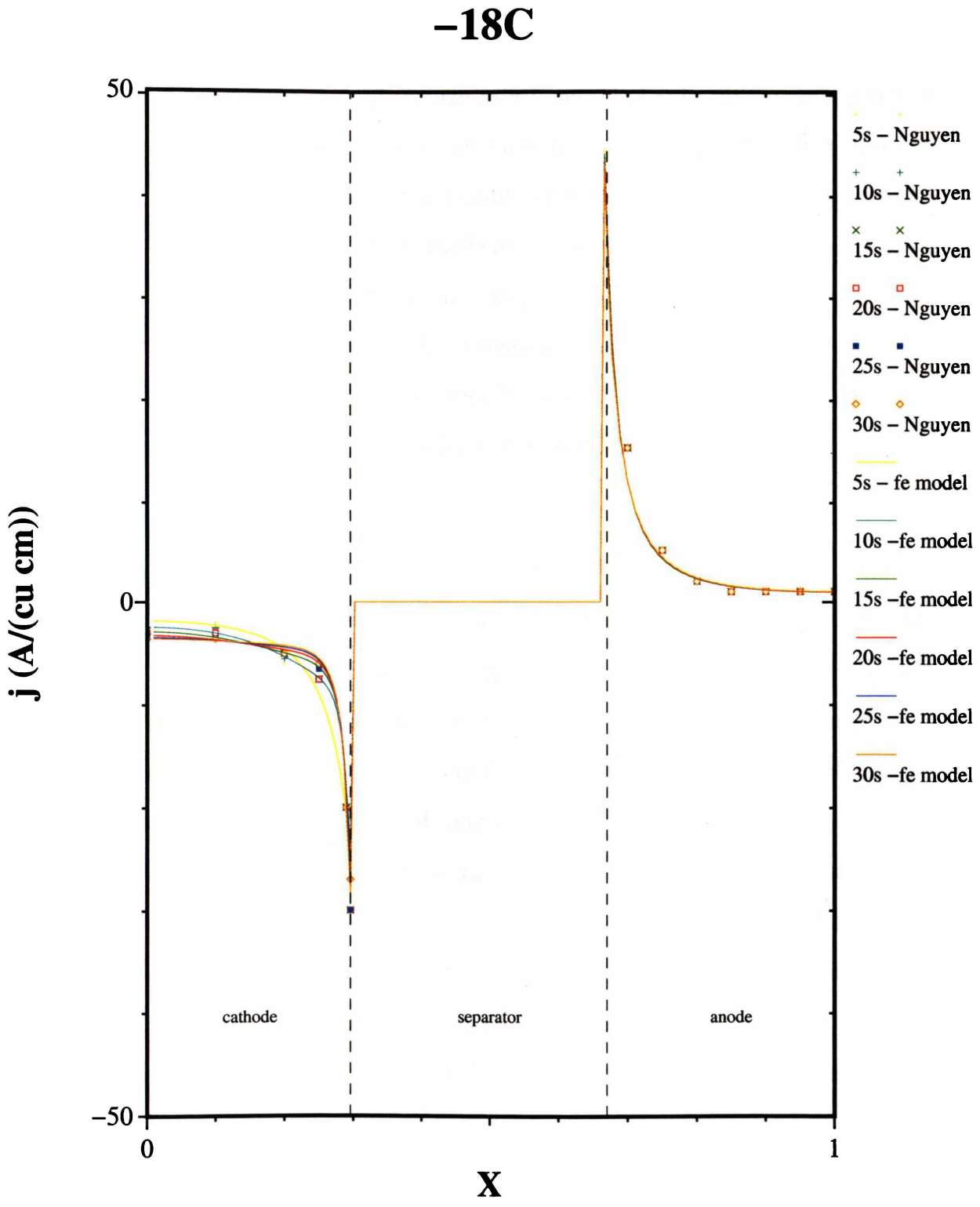

Figure 4.10: Reaction rate profiles for 408 $mAcm^{-2}$ with time.

Figure 4.11 shows the finite element results for the porosity profiles with Nguyen's data superimposed. The results are in good agreement. The high non-uniform reaction rates at the front of the negative electrode cause a rapid drop off of porosity with time at the surface of the negative electrode.

Figure 4.12 shows the cell voltage as a function of time for the 408 $mAcm^{-2}$ discharge at -18C. The finite element data are approximately 0.1V higher over the discharge. This could be caused by a number of reasons, but possibly it is because the functional dependence of the coefficients (5.40) to (5.45) are included at each iteration and not from the previous time step as in Nguyen *et al.* Also a natural boundary condition was used in the finite element model for the solid phase potential while the Nguyen *et al* model used an iterative algorithm to determine the discharge regime. Overall, however, the two discharge curves follow the same path through the discharge.

4.6 Conclusion

The finite element method has been investigated as a method of numerically solving the non-linear coupled macrohomogeneous equations of a complete lead-acid battery system. The one-dimensional finite element battery model developed model uses the "standard" set of Newman's macrohomogeneous flooded porous electrochemical equations [Newman *et al* 62], and simulates the dynamic behaviour of a complete lead-acid battery during cycles of discharge, rest, and charge. The results were carefully analysed with the previously published works of Gu *et al* [Gu 87], and Nguyen *et al* [Nguyen *et al* 90]. The results of Gu *et al*, [Gu 97] were also studied in order to validate the methods used. The results agree well with published data.

The equations are equally applicable in each region, this means that matching conditions between different regions is not necessary. Thus the finite element algorithm is computationally more efficient than Gu *el al* [Gu 87], Nguyen *et al*

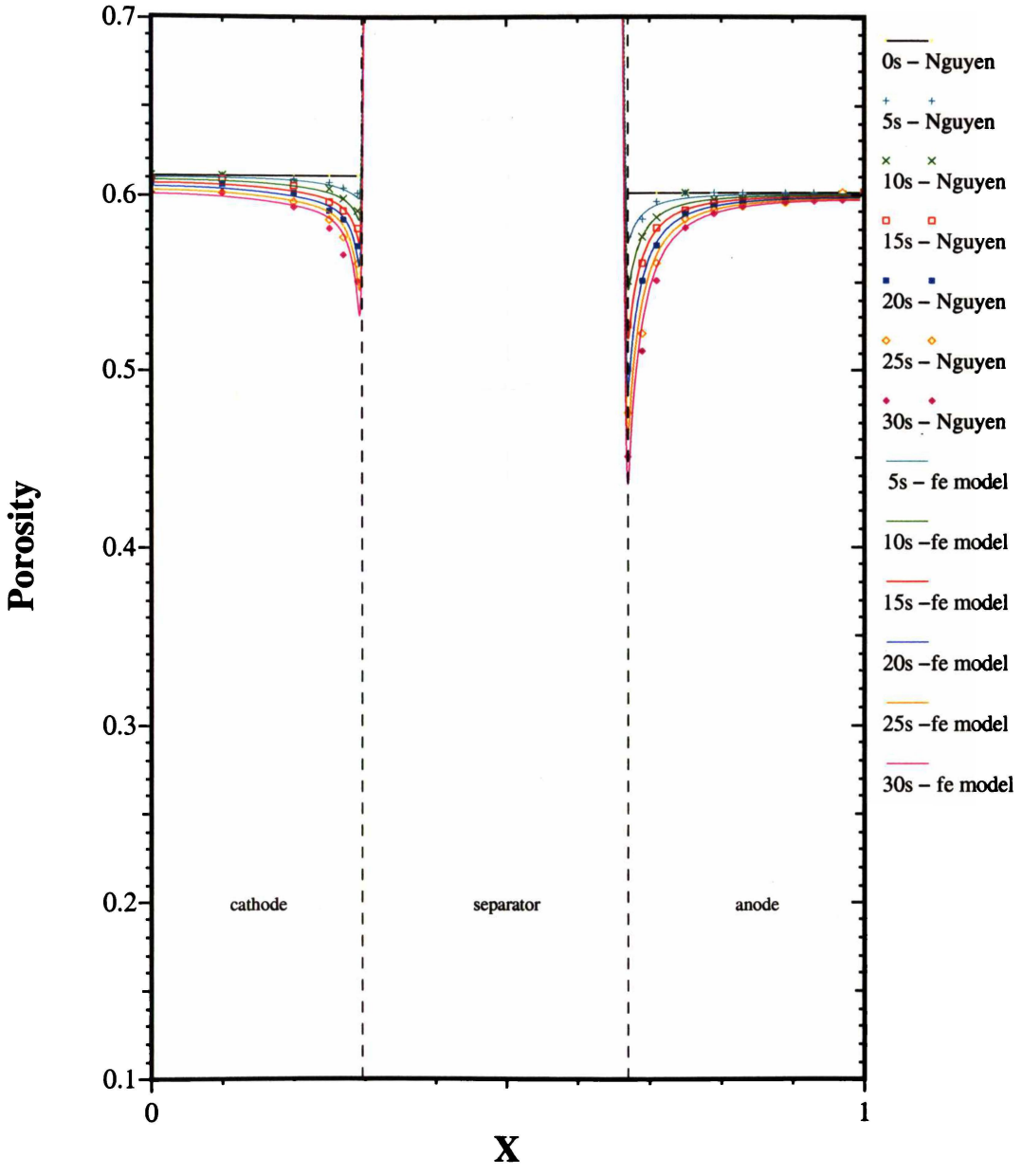

Figure 4.11: Electrode porosity profiles for 408 $mAcm^{-2}$ with time.

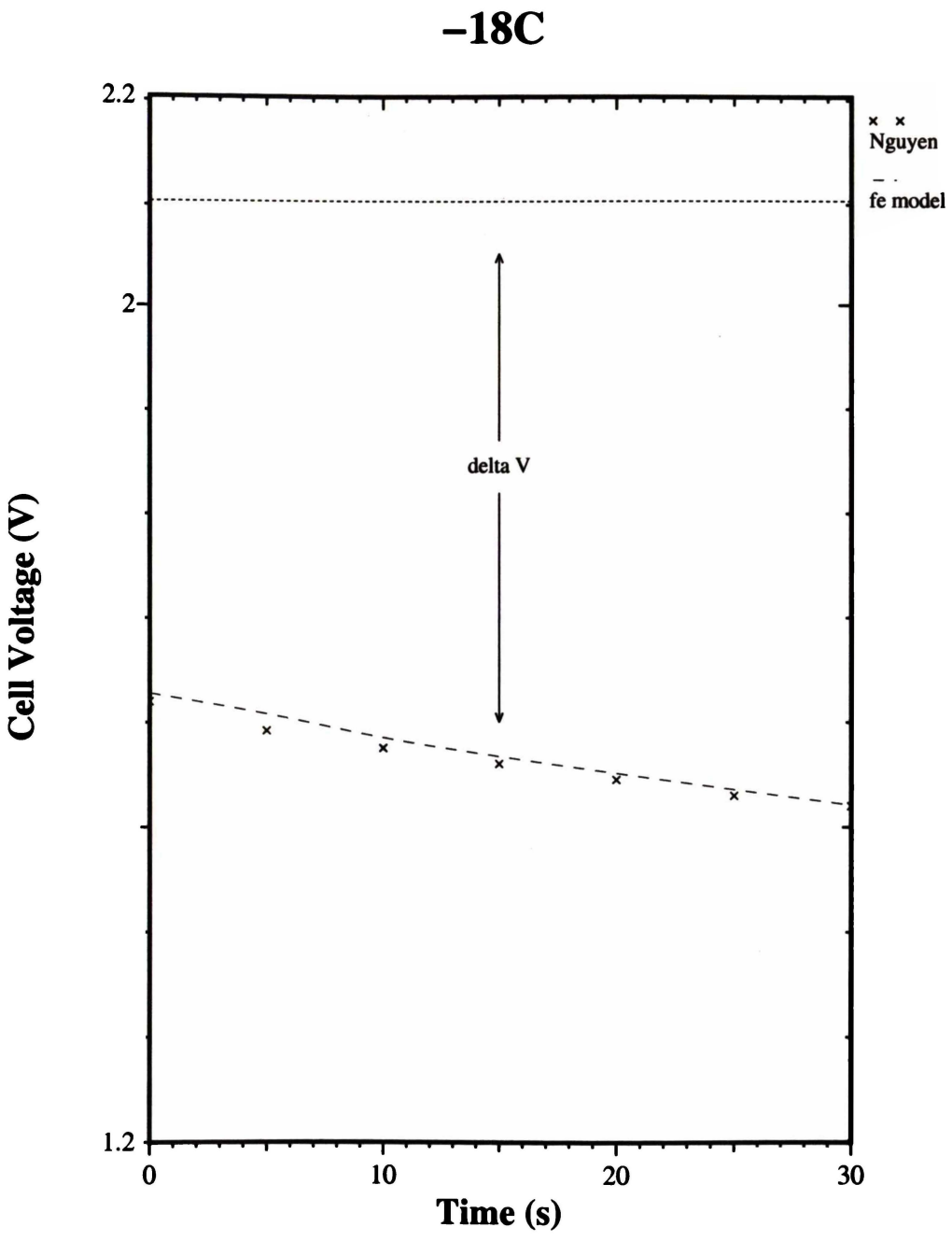

Figure 4.12: Cell voltage as a function of time for 408 $mAcm^{-2}$ at -18C.

[Nguyen *et al* 90]. Typical solution times for each time interval is a few seconds on a 133Mhz Pentium processor personal computer.

CHAPTER 5
2-D Finite Element Model

5.1 Introduction

In this chapter we extend the same formulation of the one dimensional equations to two dimensions, utilising the same numerical techniques developed in Chapter 4. The models become more complex in terms of the amount of computer resources they use and the geometry that they can describe. Finite difference methods are effectively limited to structured meshes in rectangular geometry unless complicated interpolation formulae are used. Finite elements, however, can model essentially any geometry. This, coupled with the boundary conditions arising more naturally than those associated with finite differences, means that the finite element method produces more generally applicable models.

This chapter is split into two parts: First, we define the governing equations and general boundary conditions that will be applied later. The Galerkin Weak Statement is applied, and the domain to which the equations apply are put in a discretised form suitable for numerical solution. The set of nonlinear equations are linearised with a Newton-Raphson method and solved at each time step. Secondly, the method is verified by comparing its results to those of the previously published finite difference model [Bern *et al* 93], and of a much simpler finite element model [Mao 91].

5.2 The Governing Equations

As noted previously, the overall discharge reaction of the lead-dioxide electrode is:

$$PbO_{2(solid)} + 3H^+ + HSO_4^- + 2e^- \rightarrow PbSO_{4(solid)} + 2H_2O \tag{5.1}$$

The overall discharge reaction of the lead electrode is:

$$Pb_{(solid)} + HSO_4^- \rightarrow PbSO_{4(solid)} + H^+ + 2e^- \tag{5.2}$$

The governing equations are a continuation from Chapter 4, i.e.:

Porosity Variation:

$$\frac{\partial \epsilon}{\partial t} - K_1 \left(\nabla \cdot \mathbf{i}_{soln}\right) = 0 \tag{5.3}$$

Mass transport for the H_2SO_4 electrolyte:

$$\epsilon \frac{\partial c}{\partial t} - \nabla \cdot \left(D_{eff}(x,y,c)\nabla c\right) + \left(K_2 + c(x,y)K_1\right) \nabla \cdot \mathbf{i}_{soln} = 0 \tag{5.4}$$

Ohm's law for the solution phase:

$$c(x,y)\mathbf{i}_{soln} + \kappa(x,y,c)\nabla\phi_{soln} - \kappa(x,y,c)(1-2t_+^0)\frac{RT}{F}\nabla c = 0 \tag{5.5}$$

Divergence of current of Ohm's law for the solid phase :

$$\nabla \cdot \mathbf{i}_{soln} - \nabla \cdot \left(\sigma_{eff}(x,y)\nabla\phi_{solid}\right) = 0 \tag{5.6}$$

Electrode Kinetics:

$$\nabla \cdot \mathbf{i}_{soln} - A_a i_0 \left[e^{\frac{\alpha_a F}{RT}\eta} - e^{-\frac{\alpha_c F}{RT}\eta}\right] = 0 \tag{5.7}$$

Note that $\mathbf{i}_{soln}$ is now a vector and hence, for two dimensions, we now have six equations to solve, as Ohm's law in solution needs to be solved for its x and y components.

In the reservoir and separator regions (see Figure 5.1), equations (5.5), (5.6), (5.4), and (5.3), along with the divergence of solution current density

$$\nabla \cdot \mathbf{i}_{soln} = 0 \tag{5.8}$$

apply.

The coefficients again follow from Chapter 4: The quantities K_1 and K_2 in the above equations for the positive and negative electrodes are defined as:

$$K_1^{pos} = \frac{1}{2F}\left(\frac{M_{PbSO_4}}{\rho_{PbSO_4}} - \frac{M_{PbO_2}}{\rho_{PbO_2}}\right) \tag{5.9}$$

$$K_1^{neg} = -\frac{1}{2F}\left(\frac{M_{PbSO_4}}{\rho_{PbSO_4}} - \frac{M_{PbO}}{\rho_{PbO}}\right) \tag{5.10}$$

$$K_2^{neg} = -\frac{1}{2F}\left(1 - 2t_-^0\right) \tag{5.11}$$

and

$$K_2^{pos} = \frac{1}{2F}\left(2t_+^0 - 3\right) \tag{5.12}$$

The quantities A_a and i_0 are also electrode specific:

$$A_a^{pos} = a_{max}^{pos}(1-U)^{\zeta pos} \tag{5.13}$$

$$A_a^{neg} = a_{max}^{neg}(1-U)^{\zeta neg} \tag{5.14}$$

where ζi are exponents for the charge dependence of the specific active surface area.

Also, the exchange current densities are defined for the positive and negative electrodes as:

$$i_0^{pos} = i_0^{ref,pos}\left(\frac{c}{c_{ref}}\right)^{\gamma pos} \tag{5.15}$$

$$i_0^{neg} = i_0^{ref,neg}\left(\frac{c}{c_{ref}}\right)^{\gamma neg} \tag{5.16}$$

where γi are exponents for the concentration dependence of the exchange current density.

The effect of the porous media on transport is accounted for with Bruggeman-type relations:

$$\sigma_{eff}(x,y) = \sigma(x,y)\epsilon^{exm}(x,y), \quad \kappa_{eff}(x,y,c) = \kappa(x,y,c)\epsilon^{ex}(x,y), \quad (5.17)$$

and $$D_{eff}(x,y,c) = D(x,y,c)\epsilon^{ex}(x,y)$$

Note, that the coefficients $\kappa(x,y,c)$, and $D(x,y,c)$ can depend on concentration (Appendix A.6).

The porosity is calculated from the divergence of the solution current, $\nabla \cdot \mathbf{i}_{soln}$, at each iteration.

5.2.1 Boundary and Initial Conditions

To model an electrochemical cell in two dimensions requires careful placement of the appropriate boundary conditions. As the solution current, $\mathbf{i}_{soln}$, is a vector, we have to consider which component is significant. Also, as the solution current is first order in the governing equations, we prescribe the solution current density at the boundaries. The initial conditions are the same as in the one dimensional model.

We will treat here the general case for the application of the boundary conditions; the exact boundary conditions will be detailed for their respective models later in the chapter.

Initial Conditions

The initial conditions are the same as for the one-dimensional model. We prescribe an initial porosity, ϵ_0, and initial sulphuric acid concentration, c_0. Equations (5.5), (5.6), and (5.7) are then solved for $\mathbf{i}_{soln}$, ϕ_{solid}, and ϕ_{soln}.

Boundary Conditions

If we consider the battery cell as a whole, it is a closed system and as such the concentration at the boundaries is given by:

$$\frac{\partial c}{\partial \mathbf{n}} = 0 \tag{5.18}$$

where $\mathbf{n}$ represents the normal vector to the boundary surface. Similarly, we can apply the same homogeneous boundary condition at positions of symmetry.

We can apply homogeneous Neuman conditions at positions of symmetry and on current collector surfaces, where:

$$\frac{\partial \phi_{soln}}{\partial \mathbf{n}} = 0 \tag{5.19}$$

For the solid potential we can again apply homogeneous Neuman boundary conditions at positions of symmetry.:

$$\frac{\partial \phi_{solid}}{\partial \mathbf{n}} = 0 \tag{5.20}$$

Where current is collected, we can apply either of the following prescribed boundary conditions:

$$\phi_{solid} = 0 \quad \text{or} \quad V \tag{5.21}$$

for a constant voltage discharge/charge; or we can apply the following Neuman boundary condition:

$$-\sigma_{eff} \frac{\partial \phi_{solid}}{\partial \mathbf{n}} = I \tag{5.22}$$

for a constant current discharge/charge.

To obtain a particular solution for the non-homogeneous Neuman boundary condition, we must set the solid potential, ϕ_{solid}, to a constant at a point in one of the electrodes.

The solution current, $\mathbf{i}_{soln}$, must be prescribed for its respective components at the boundary in the present formulation. Fortunately, as long as some thought is given to the modeled region, this poses few problems. For appropriately modeled regions we may specify that $\mathbf{i}_{soln,\mathbf{n}} = 0$; that is, the solution current normal to the surface is zero.

5.3 Method of Solution

The governing equations are coupled and nonlinear. They are put into Galerkin finite element form and solved using a modified Newton-Raphson method, as discussed in Chapter 2.

5.3.1 Galerkin formulation of the residuals

First, we put the five equations into Galerkin residual equation form.

We use the divergence of solution current density to calculate the porosity at each time step. The porosity has spatial but no temporal component in the finite element formulation. It is calculated for each time step and subtracted from the value for porosity at the previous time step. The residual is written as:

$$\begin{aligned} R(x,y,t;a) &= \int^{\Omega(e)} \epsilon(x,y,t;a)\varphi_i^{(e)} d\Omega - \int^{\Omega(e)} K_1 \frac{\partial \tilde{i}_{x,soln}(x,y,t;a)}{\partial x}\varphi_i^{(e)} d\Omega \\ &- \int^{\Omega(e)} K_1 \frac{\partial \tilde{i}_{y,soln}(x,y,t;a)}{\partial y}\varphi_i^{(e)} d\Omega \\ &= 0 \end{aligned} \tag{5.23}$$

The residual for material balance for H_2SO_4 from equation (5.4) is:

$$\begin{aligned} R(x,y,t;a) &= \int^{\Omega(e)} \varphi_i^{(e)} \left[\epsilon(x,y)\frac{\partial \tilde{c}(x,y,t;a)}{\partial t} - \frac{\partial}{\partial x}\left(D_{eff}(x,y)\,\frac{\partial \tilde{c}(x,y,t;a)}{\partial x}\right) \right. \\ &- \frac{\partial}{\partial y}\left(D_{eff}(x,y)\frac{\partial \tilde{c}(x,y,t;a)}{\partial y}\right) \\ &+ \left. (K_2 + c(x,y)K_1)\left(\frac{\partial \tilde{i}_{x,soln}(x,y,t;a)}{\partial x} + \frac{\partial \tilde{i}_{y,soln}(x,y,t;a)}{\partial y}\right)\right] d\Omega \\ &= 0 \end{aligned} \tag{5.24}$$

Integrating the second-order derivative by parts gives:

$$\begin{aligned} R(x,y,t;a) &= \int^{\Omega(e)} \varphi_i^{(e)} \epsilon \frac{\partial \tilde{c}(x,y,t;a)}{\partial t} d\Omega + \int^{\Omega(e)} \frac{\partial \varphi_i^{(e)}(x)}{\partial x} D_{eff} \frac{\partial \tilde{c}(x,y,t;a)}{\partial x} d\Omega \\ &+ \int^{\Omega(e)} \frac{\partial \varphi_i^{(e)}(x)}{\partial y} D_{eff} \frac{\partial \tilde{c}(x,y,t;a)}{\partial y} d\Omega \\ &+ \int^{\Omega(e)} \varphi_i^{(e)} \left(K_2 + cK_1\right) \frac{\partial \tilde{i}_{x,soln}(x,y,t;a)}{\partial x} + \frac{\partial \tilde{i}_{y,soln}(x,y,t;a)}{\partial y} d\Omega \\ &+ \int^{\Gamma(e)} \left(-D_{eff} \frac{\partial \tilde{c}(x,y,t;a)}{\partial \mathbf{n}}\right) \varphi_i d\Gamma \\ &= 0 \end{aligned} \tag{5.25}$$

We create two equations for Ohm's law in solution, (5.5), for the x and y components:

The residual for Ohm's law in solution in the x-direction is:

$$\begin{aligned} R(x,y,t;a) &= \int^{\Omega(e)} \varphi_i^{(e)} \left[\tilde{i}_{x,soln}(x,y,t;a) c(x,y) + c(x,y) \kappa_{eff}(x,y,c) \frac{\partial \tilde{\phi}_{soln}(x,y,t;a)}{\partial x} \right. \\ &\left. - \kappa_{eff}(x,y,c)(1-2t_+^0) \frac{RT}{F} \frac{\partial \tilde{c}(x,y,t;a)}{\partial x} \right] d\Omega \\ &= 0 \end{aligned} \tag{5.26}$$

The residual for Ohm's law in solution in the y-direction is:

$$\begin{aligned} R(x,y,t;a) &= \int^{\Omega(e)} \varphi_i^{(e)} \left[\tilde{i}_{y,soln}(x,y,t;a) c(x,y) + c(x,y) \kappa_{eff}(x,y,c) \frac{\partial \tilde{\phi}_{soln}(x,y,t;a)}{\partial y} \right. \\ &\left. - \kappa_{eff}(x,y,c)(1-2t_+^0) \frac{RT}{F} \frac{\partial \tilde{c}(x,y,t;a)}{\partial y} \right] d\Omega \\ &= 0 \end{aligned} \tag{5.27}$$

The residual for the divergence of current,(5.6), is:

$$\begin{aligned} R(x,y.t;a) &= \int^{\Omega(e)} \varphi_i^{(e)} \left[\frac{\partial \tilde{i}_{x,soln}(x,y,t;a)}{\partial x} + \frac{\partial \tilde{i}_{y,soln}(x,y,t;a)}{\partial y} \right. \\ &\left. - \frac{\partial}{\partial x}\left(\sigma_{eff}(x,y) \frac{\partial \phi_{solid}(x,y,t;a)}{\partial x}\right) - \frac{\partial}{\partial y}\left(\sigma_{eff}(x,y) \frac{\partial \phi_{solid}(x,y,t;a)}{\partial y}\right) \right] d\Omega \\ &= 0 \end{aligned} \tag{5.28}$$

Integrating the second-order derivative by parts gives:

$$\begin{aligned} R(x,y,t;a) &= \int^{\Omega(e)} \varphi_i^{(e)} \frac{\partial \tilde{i}_{x,soln}(x,y,t;a)}{\partial x} d\Omega + \int^{\Omega(e)} \varphi_i^{(e)} \frac{\partial \tilde{i}_{y,soln}(x,y,t;a)}{\partial y} d\Omega \\ &+ \int^{\Omega(e)} \frac{\partial \varphi_i^{(e)}(x)}{\partial x} \sigma_{eff}(x,y) \frac{\partial \tilde{\phi}_{solid}(x,y,t;a)}{\partial x} d\Omega \\ &+ \int^{\Omega(e)} \frac{\partial \varphi_i^{(e)}(x)}{\partial y} \sigma_{eff}(x,y) \frac{\partial \tilde{\phi}_{solid}(x,y,t;a)}{\partial y} d\Omega \\ &+ \int^{\Gamma(e)} \left(-\sigma_{eff} \frac{\partial \tilde{\phi}_{solid}(x,y,t;a)}{\partial \mathbf{n}} \right) \varphi_i d\Gamma \\ &= 0 \end{aligned} \tag{5.29}$$

The residual for electrode kinetics (5.7) is:

$$\begin{aligned} R(x,y,t;a) &= \int^{\Omega(e)} \varphi_i^{(e)} \left[\frac{\partial \tilde{i}_{x,soln}(x,y,t;a)}{\partial x} + \int^{\Omega(e)} \frac{\partial \tilde{i}_{y,soln}(x,y,t;a)}{\partial y} \right. \\ &- \left. \int^{\Omega(e)} A_a i_0 \left(e^{\frac{\alpha_a F}{RT}\eta} - e^{-\frac{\alpha_a F}{RT}\eta} \right) \right] d\Omega \\ &= 0 \end{aligned} \tag{5.30}$$

5.3.2 Trial Functions for the Governing Equations

The trial solutions follow directly from the one-dimensional case. We can use the two-dimensional basis functions defined in Chapter 3 to support approximate solutions of the following:

$$\tilde{\epsilon}^{(e)}(x,y,t;a) = \sum_{j=1}^{n} \epsilon_j(t) \varphi_j^{(e)}(x,y) \tag{5.31}$$

$$\tilde{c}^{(e)}(x,y,t;a) = \sum_{j=1}^{n} c_j(t) \varphi_j^{(e)}(x,y) \tag{5.32}$$

$$\tilde{i}_{x,soln}^{(e)}(x,y,t;a) = \sum_{j=1}^{n} i_{x,soln,j}(t) \varphi_j^{(e)}(x,y) \tag{5.33}$$

$$\tilde{i}_{y,soln}^{(e)}(x,y,t;a) = \sum_{j=1}^{n} i_{y,soln,j}(t) \varphi_j^{(e)}(x,y) \tag{5.34}$$

$$\tilde{\phi}^{(e)}_{solid}(x,y,t;a) = \sum_{j=1}^{n} \phi_{solid,j}(t)\varphi^{(e)}_j(x,y) \tag{5.35}$$

$$\tilde{\phi}^{(e)}_{soln}(x,y,t;a) = \sum_{j=1}^{n} \phi_{soln,j}(t)\varphi^{(e)}_j(x,y) \tag{5.36}$$

We can also use basis functions to interpolate the following variables, ϵ, κ, σ:

$$\tilde{\epsilon}^{(e)}(x,y,t;a) = \sum_{j=1}^{n} \epsilon_j(t)\varphi^{(e)}_j(x,y) \tag{5.37}$$

$$\tilde{\kappa}^{(e)}_{soln}(x,y,t;a) = \sum_{j=1}^{n} \kappa_{soln,j}(t)\varphi^{(e)}_j(x,y) \tag{5.38}$$

$$\tilde{\sigma}^{(e)}_{soln}(x,y,t;a) = \sum_{j=1}^{n} \sigma_{soln,j}(t)\varphi^{(e)}_j(x,y) \tag{5.39}$$

Substituting the respective trial functions and derivatives of the trial functions into their residual equations gives:

Porosity variation:

$$\sum_{j=1}^{n} \int^{\Omega(e)} \varphi^{(e)}_i(x,y)\varphi^{(e)}_j(x,y)\frac{d\epsilon_{soln,j}(t)}{dt}d\Omega - \sum_{j=1}^{n} \int^{\Omega(e)} K_1 \frac{d\varphi^{(e)}_j(x,y)}{dx}\varphi^{(e)}_i(x,y)\phi_{solid,j}(t)d\Omega$$
$$- \sum_{j=1}^{n} \int^{\Omega(e)} K_1 \frac{d\varphi^{(e)}_j(x,y)}{dy}\varphi^{(e)}_i(x,y)\phi_{solid,j}(t)d\Omega = 0 \tag{5.40}$$

Material balance:

$$\sum_{j=1}^{n} \int^{\Omega(e)} \varphi^{(e)}_i(x,y)\varphi^{(e)}_j(x,y)\epsilon(t)\varphi^{(e)}_j(x,y)\frac{dc_j(t)}{dt}d\Omega$$
$$+ \sum_{j=1}^{n} \int^{\Omega(e)} \frac{d\varphi^{(e)}_i(x,y)}{dx}\varphi^{(e)}_j(x,y)D_{eff}(t)\frac{d\varphi^{(e)}_j(x,y)}{dx}c_j(t)d\Omega$$
$$+ \sum_{j=1}^{n} \int^{\Omega(e)} \frac{d\varphi^{(e)}_i(x,y)}{dy}\varphi^{(e)}_j(x,y)D_{eff}(t)\frac{d\varphi^{(e)}_j(x,y)}{dy}c_j(t)d\Omega$$

$$+ \sum_{j=1}^{n} \int^{\Omega(e)} \varphi_i^{(e)}(x,y) \left(K_2 + \varphi_i^{(e)}(x,y)\varphi_j^{(e)}(x,y)c_j(t)K_1 \right) \frac{d\varphi_j^{(e)}(x,y)}{dx} i_{soln,j}(t)d\Omega$$

$$+ \sum_{j=1}^{n} \int^{\Omega(e)} \varphi_i^{(e)}(x,y) \left(K_2 + \varphi_i^{(e)}(x,y)\varphi_j^{(e)}(x,y)c_j(t)K_1 \right) \frac{d\varphi_j^{(e)}(x,y)}{dy} i_{soln,j}(t)d\Omega$$

$$+ \int^{\Gamma(e)} \left(-D_{eff} \frac{\partial c(x,\tilde{y},t;a)}{\partial \mathbf{n}} \right) \varphi_i d\Gamma = 0 \tag{5.41}$$

Ohm's law in solution in the x-direction:

$$\sum_{j=1}^{n} \int^{\Omega(e)} \varphi_j^{(e)}(x,y)c_j(t)\varphi_j^{(e)}(x,y)i_{x,soln,j}(x,y,t)d\Omega$$

$$+ \sum_{j=1}^{n} \int^{\Omega(e)} \varphi_j^{(e)}(x,y)c(t)\varphi_i^{(e)}(x,y)\kappa_{eff,j}(t)\varphi_j^{(e)}(x,y)\frac{d\varphi_j^{(e)}(x,y)}{dx}\phi_{soln,j}(t)d\Omega$$

$$- \sum_{j=1}^{n} \int^{\Omega(e)} \varphi_j^{(e)}(x,y)\kappa_{eff,j}(t)(1-2t_+^0)\frac{RT}{F}\varphi_i^{(e)}(x,y)\frac{d\varphi_j^{(e)}(x,y)}{dx}c_j(t)d\Omega = 0 \tag{5.42}$$

Ohm's law in solution in the y-direction:

$$\sum_{j=1}^{n} \int^{\Omega(e)} \varphi_j^{(e)}(x,y)c_j(t)\varphi_j^{(e)}(x,y)i_{y,soln,j}(x,y,t)d\Omega$$

$$+ \sum_{j=1}^{n} \int^{\Omega(e)} \varphi_j^{(e)}(x,y)c(t)\varphi_i^{(e)}(x,y)\kappa_{eff,j}(t)\varphi_j^{(e)}(x,y)\frac{d\varphi_j^{(e)}(x,y)}{dy}\phi_{soln,j}(t)d\Omega$$

$$- \sum_{j=1}^{n} \int^{\Omega(e)} \varphi_j^{(e)}(x,y)\kappa_{eff,j}(t)(1-2t_+^0)\frac{RT}{F}\varphi_i^{(e)}(x,y)\frac{d\varphi_j^{(e)}(x,y)}{dy}c_j(t)d\Omega = 0 \tag{5.43}$$

Divergence of current:

$$\sum_{j=1}^{n} \int^{\Omega(e)} \varphi_i^{(e)}(x,y)\frac{d\varphi_j(x,y)}{dx}i_{x,soln,j}(t)d\Omega$$

$$+ \sum_{j=1}^{n} \int^{\Omega(e)} \varphi_i^{(e)}(x)\frac{d\varphi_j(x,y)}{dy}i_{y,soln,j}(t)d\Omega$$

$$+ \sum_{j=1}^{n} \int^{\Omega(e)} \frac{d\varphi_i^{(e)}(x,y)}{dx}\sigma_{eff}(x,y)\frac{d\varphi_j(x,y)}{dx}\phi_{solid,j}(t)d\Omega$$

$$+ \sum_{j=1}^{n} \int^{\Omega(e)} \frac{d\varphi_i^{(e)}(x,y)}{dy} \sigma_{eff}(x,y) \frac{d\varphi_j(x,y)}{dy} \phi_{solid,j}(t) d\Omega$$
$$+ \int^{\Gamma(e)} \left(-\sigma_{eff} \frac{\partial \tilde{\phi}_{solid}(x,y,t;a)}{\partial \mathbf{n}} \right) \varphi_i d\Gamma \tag{5.44}$$

Electrode kinetics:

$$\sum_{j=1}^{n} \int^{\Omega(e)} \frac{d\varphi_j^{(e)}(x,y)}{dx} \varphi_i^{(e)}(x,y) i_{x,soln,j}(t) d\Omega + \sum_{j=1}^{n} \int^{\Omega(e)} \frac{d\varphi_j^{(e)}(x,y)}{dy} \varphi_i^{(e)}(x,y) i_{y,soln,j}(t) d\Omega$$
$$- \int^{\Omega(e)} A_a i_0 \left(e^{\frac{\alpha_a F}{RT}\eta} - e^{-\frac{\alpha_a F}{RT}\eta} \right) \varphi_i^{(e)} d\Omega = 0 \tag{5.45}$$

Rewriting the coupled equations (5.40) to (5.45) as a residual r^k in terms of a matrix-type equation:

$$\{r^k(x,t;a)\} = [C]^{(e)} \left\{ \frac{dw(t)}{dt} \right\} + ([K]^{(e)} + [U]^{(e)})\{w(t)\} - \{F(t)\}^{(e)} = 0 \tag{5.46}$$

where

$$[C_{ij}] = \sum_e \int^{\Omega(e)} \begin{bmatrix} \varphi_i^{(e)}\varphi_j^{(e)} & 0 & 0 & 0 & & \\ 0 & \epsilon(t)\varphi_i^{(e)}\varphi_j^{(e)} & 0 & 0 & & \\ 0 & 0 & 0 & 0 & 0 & 0 \\ 0 & 0 & 0 & 0 & 0 & 0 \\ 0 & 0 & 0 & 0 & 0 & 0 \\ 0 & 0 & 0 & 0 & 0 & 0 \end{bmatrix} \tag{5.47}$$

and:

$$[K_{ij}] = \sum_e \int^{(e)}$$

$$\begin{bmatrix} 0 & 0 & 0 & 0 & 0 & 0 \\ 0 & \frac{d\varphi_i^{(e)}}{dx}\varphi_j^{(e)} D_{eff,j}(t) \frac{d\varphi_j^{(e)}}{dx} + \frac{d\varphi_i^{(e)}}{dy}\varphi_j^{(e)} D_{eff,j}(t) \frac{d\varphi_j^{(e)}}{dy} & 0 & 0 & 0 & 0 \\ 0 & 0 & 0 & 0 & 0 & 0 \\ 0 & 0 & 0 & 0 & 0 & 0 \\ 0 & 0 & \frac{d\varphi_i^{(e)}}{dx}\varphi_j^{(e)} \sigma_{eff,j}(t) \frac{d\varphi_j}{dx} + \frac{d\varphi_i^{(e)}}{dx}\varphi_j^{(e)} \sigma_{eff,j}(t) \frac{d\varphi_j}{dx} & 0 & 0 & 0 \\ 0 & 0 & 0 & 0 & 0 & 0 \end{bmatrix} \tag{5.48}$$

and:

$$[U_{ij}] = \sum_e \int^{(e)}$$

$$\begin{bmatrix}
0 & 0 & -\frac{d\varphi_j^{(e)}}{dx}\varphi_i^{(e)} & -\frac{d\varphi_j^{(e)}}{dx}\varphi_i^{(e)} & 0 & 0 \\
0 & 0 & \left(K_2+\varphi_j^{(e)}c_j(t)K_1\right)\frac{d\varphi_j^{(e)}}{dx}\varphi_i^{(e)} & \frac{d\varphi_j^{(e)}}{dy}\varphi_i^{(e)} & 0 & 0 \\
0 & -\varphi_j^{(e)}\kappa_{eff,j}(t)(1-2t_+^0)\frac{RT}{F}\frac{d\varphi_i^{(e)}}{dx}\varphi_j^{(e)} & 0 & 0 & 0 & \varphi_j^{(e)}c_j(t)\varphi_j^{(e)}\kappa_{eff,j}(t)\frac{d\varphi_i^{(e)}}{dx}\varphi_j^{(e)} \\
0 & -\varphi_j^{(e)}\kappa_{eff,j}(t)(1-2t_+^0)\frac{RT}{F}\frac{d\varphi_i^{(e)}}{dy}\varphi_j^{(e)} & 0 & 0 & 0 & \varphi_j^{(e)}c_j(t)\varphi_j^{(e)}\kappa_{eff,j}(t)\frac{d\varphi_i^{(e)}}{dy}\varphi_j^{(e)} \\
0 & 0 & \frac{d\varphi_j^{(e)}}{dx}\varphi_i^{(e)} & \frac{d\varphi_j^{(e)}}{dy}\varphi_i^{(e)} & 0 & 0 \\
0 & 0 & \frac{d\varphi_j^{(e)}}{dx}\varphi_i^{(e)} & \frac{d\varphi_j^{(e)}}{dx}\varphi_i^{(e)} & 0 & 0
\end{bmatrix} \tag{5.49}$$

and:

$$\{F_i(t)\} = \{F(t)_\Omega^i\} + \{F_i(t)_{\Gamma,1}\} + \{F_i(t)_{\Gamma,2}\} \tag{5.50}$$

where the subscript Γ_1 denotes terms arising from the Dirichlet boundary conditions, the subscript Γ_2 are those terms arising from Neuman boundary conditions. The components of equation (5.50) are:

$$\{F_i(t)_\Omega\} = \sum_e \int^{\Omega(e)} \begin{Bmatrix} 0 \\ 0 \\ \varphi_j^{(e)}c_j(t)i_{x,soln}(x,y,t;a)\varphi_i^{(e)} \\ \varphi_j^{(e)}c_j(t)i_{y,soln}(x,y,t;a)\varphi_i^{(e)} \\ 0 \\ -A_a i_0\left(e^{\frac{\alpha_a F}{RT}\eta} - e^{-\frac{\alpha_a F}{RT}\eta}\right)\varphi_i^{(e)} \end{Bmatrix} \tag{5.51}$$

and :

$$\{F_i(t)_\Gamma\} = \begin{Bmatrix} f_{por,\Gamma} \\ f_{mat\ bal,\Gamma} \\ f_{ohm_x\ sol,\Gamma} \\ f_{ohm_y\ sol,\Gamma} \\ f_{\nabla i_{soln},\Gamma} \\ f_{kin,\Gamma} \end{Bmatrix} \tag{5.52}$$

The degrees of freedom may be represented as:

$$\{w(t)_j\} = \begin{Bmatrix} \epsilon_j(t) \\ c_j(t) \\ i_{x,soln,j}(t) \\ i_{y,soln,j}(t) \\ \phi_{solid,j}(t) \\ \phi_{soln,j}(t) \end{Bmatrix} \tag{5.53}$$

We calculate the Jacobian matrix for the matrix equation (5.46) from:

$$[J^k(w)] = \frac{\partial\{r^k(w)\}}{\partial\{w\}} \tag{5.54}$$

Hence the Jacobian matrix for (5.46) is:

$$[J(w)] = \sum_e \int^{(e)} \begin{bmatrix} 0 & 0 & \frac{dU_{1,3}}{di_{x,soln}} & \frac{dU_{1,4}}{di_{y,soln}} & 0 & 0 \\ 0 & \frac{dK_{2,2}}{dc} & \frac{dU_{2,3}}{di_{x,soln}} & \frac{dU_{2,4}}{di_{y,soln}} & 0 & 0 \\ 0 & \frac{dU_{3,2}}{dc} - \frac{dF_3}{dc} & -\frac{dF_3}{di_{x,soln}} & 0 & 0 & \frac{dU_{3,6}}{d\phi_{soln}} \\ 0 & \frac{dU_{4,2}}{dc} - \frac{dF_4}{dc} & 0 & -\frac{dF_4}{di_{y,soln}} & 0 & \frac{dU_{4,6}}{d\phi_{soln}} \\ 0 & \frac{dU_{5,3}}{di_{y,soln}} & \frac{dU_{5,4}}{di_{x,soln}} & 0 & \frac{dK_{5,5}}{d\phi_{solid}} & 0 \\ 0 & 0 & \frac{dU_{6,3}}{di_{x,soln}} & \frac{dU_{6,4}}{di_{y,soln}} & -\frac{dF_2}{d\phi_{solid}} & -\frac{dF_2}{d\phi_{soln}} \end{bmatrix} \tag{5.55}$$

where the subscript terminology represents the row and column of the respective $[K]$, $[U]$, and $\{F\}$ matrices.

The set of non-linear algebraic equations (5.46) is linearised with a Newton-Raphson iteration technique as detailed in Chapter 3. It has the form:

$$[J^k(w)]\ \left(\{w^{k+1}\} - \{w^k\}\right)\ =\ -\{r^k(w)\}, \tag{5.56}$$

where k denotes the number of the iteration.

5.4 Model Discussion

We are solving for six unknowns, ϵ, c, $i_{x,soln}$, $i_{y,soln}$, ϕ_{solid}, and ϕ_{soln}. The governing differential equations are strongly coupled and nonlinear. The model differs from the one-dimensional case in that the divergence of current is solved in the coupled set of equations and is used to calculate the volume fraction of electrolyte (porosity), ϵ, and the state of charge, SOC, at each interval. In the one dimensional model, we calculated the divergence of solution current density once the solution current had been solved.

A fully integrated finite element method is used to solve the whole electrochemical cell. This offers considerable simplifications to the numerical simulations, as there is no need for matching boundary conditions between the different regions as in previous models, for example [Bern *et al* 93], [Gu 87], [Nguyen *et al* 90]. One exception is the model of Gu *et al*, [Gu 97], which used a computational fluid dynamics

finite difference method. They were also able to apply the same governing equations over all the regions.

Virtually any geometry of an electrochemical cell can be modeled with ease using this technique.

5.4.1 Necessary Conditions for the Elements

The conditions for the elements follow directly from Chapter 4. From the Galerkin weak statement, c and ϕ_{solid} appear as first order differentials, thus requiring that the basis functions be continuously differentiable in each element and continuous in the whole domain Ω. The functions, $i_{x,soln}$, $i_{y,soln}$ and ϕ_{soln}, are not differentiated in the Galerkin equations. The basis functions are required to be continuous in each element, but can be discontinuous in the domain Ω. They must be integrable.

The conditions for the basis functions for i_{soln} and ϕ_{soln} are weaker than the conditions for the basis functions of c and ϕ_{solid}. As previously noted, a finite element which satisfies the above is said to be conforming.

5.4.2 External Boundary Conditions

The external boundary conditions are the two-dimensional equivalent of the one-dimensional model. They are all homogeneous except for the solid phase potential, ϕ_{solid}, which can be non-homogeneous for prescribed regions. The boundary condition for ϕ_{solid} arises naturally in the formulation of the weak statement.

5.5 Numerical Results

5.5.1 Overview

In this section we firstly benchmark the two-dimensional finite element model with those of Bernardi *el al* [Bern *et al* 93] and the simple finite element model of Mao *et al* [Mao 91]. The Bernardi *et al* model is a two-dimensional model that is concerned with the mass transport processes and the variations that occur through the height of the cell. Mao *et al*'s model, on the other hand, is concerned with the

effects of grid design, plate separation and geometry on the potential and current density distributions on an "advanced" lead-acid battery.

The present model is not compared to that of Gu's [Gu 97]. Movement of electrolyte does not usually represent a significant contribution to the net flux of sulphuric acid in the cell, hence convective flow has been neglected in the governing equations. Gu's two-dimensional model results are concerned with stratification and are compared with Alavyoon's experimental results, [Alav *et al* 91], for this phenomena. The inclusion of fluid dynamics equations into the set of governing equations in principle offers no more difficulties other than an increase in computational resources. An important aspect of the present work is to investigate the applicability of finite elements to electrochemical transport equations.

In the second part of this section several model results are presented for a variety of geometries to show the flexibility of the finite element method when applied to electrochemical systems. This demonstrates the generality of the numerical method and its ability to be used to design and optimise lead-acid batteries.

5.5.2 Comparison with the Bernardi *et al* Model

Bernardi *et al*, [Bern *et al* 93] modeled a two-dimensional lead-acid cell using Newman's macrohomogeneous equations [Newman *et al* 62]. They assumed negligible convective flow and adopted concentrated electrolyte theory. The equations are identical to those of equations (5.4) to (5.7). The cell setup is shown in Figure 5.1. The cell is composed of four regions, a negative Pb electrode, a porous separator, a reservoir of electrolyte, and a positive PbO_2 electrode. The electrode's active material porous matrix is filled with sulphuric acid which occupies the free space within the current collector grid.

The positive and negative electrodes in Figure 5.1 are modeled as one half of a plate, i.e., the left and right boundaries are the centres of the respective electrodes

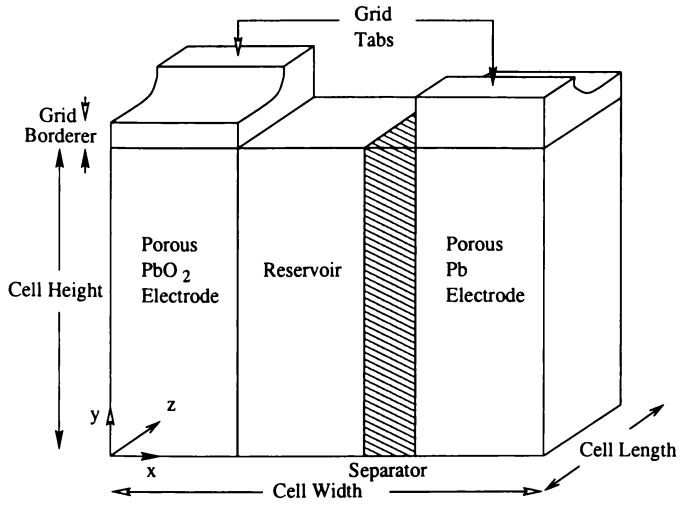

Figure 5.1: Schematic of Bernardi's two-dimensional model for a lead-acid cell

and represent planes of symmetry. The unit cell shown is repeated to form a stack of cells. Electrical current is drawn from grid tabs at the top of the electrodes.

As illustrated in Figure 5.1, the x-direction represents the width of the unit cell modeled. The y-direction represents the height of the cell. The z-direction, which is not modeled, represents the cells length. As previously stated, natural convection effects are not included. Hence the model is applicable for conditions where the stratification is intrinsically stable. An example would be where the electrolyte density increases towards the bottom of the cell. The set of equations is not strictly valid for the charging of lead-acid batteries, where unstable forms of stratification occur.

Finally, in order to satisfactorily model a cell in two-dimensions we make the assumption that the conductivity of the top border is sufficiently conductive for the non-uniformities that arise in the cell length to be ignored. In a typical lead-acid cell, the grid is constructed of lead, and there can be significant variations in cell length [Sunu *et al* 81], [Tied *et al* 79a] and [Morimoto *et al* 88], especially for high discharge currents. Cells with a small aspect ratio (i.e., width/height $\rightarrow$ 0) are also modeled well with the present scheme.

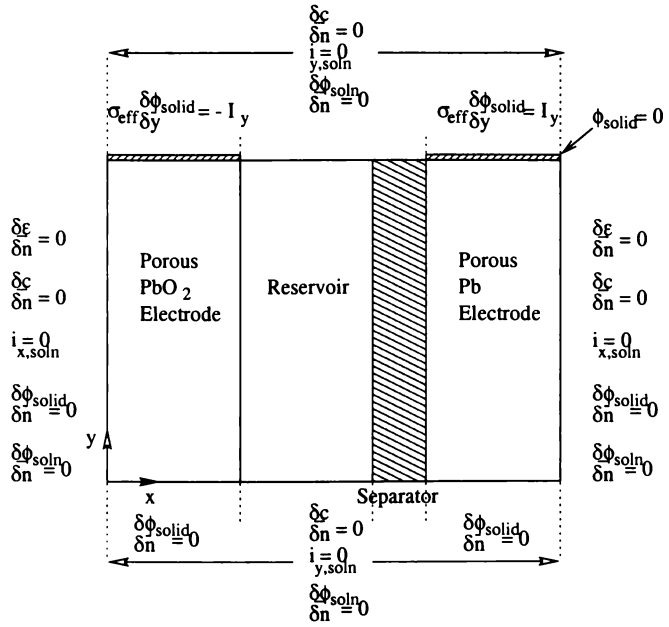

Figure 5.2: Schematic of the boundary conditions for two-dimensional finite element model with Bernardi *et al* input parameters.

For the initial conditions, we take the initial porosity and electrolyte concentration to be uniform at the start of discharge. These values are summarisied in Appendix A.4.

Figure 5.2 details the applied boundary conditions for the two-dimensional finite element model. Symmetry exists at the centre of each electrode, hence:

$$\frac{\partial c}{\partial \mathbf{n}} = \frac{\partial \phi_{soln}}{\partial \mathbf{n}} = \frac{\partial \epsilon}{\partial \mathbf{n}} = \frac{\partial \phi_{solid}}{\partial \mathbf{n}} = \mathbf{i}_{\mathbf{n},soln} = 0 \tag{5.57}$$

where $\mathbf{n}$ represents the unit vector normal to the boundary surface.

The cell is filled with electrolyte just to the height of the active material ($y = H$) in order to simplify the boundary conditions. In a real cell there is a reservoir of electrolyte above the plates. Hence, across the top and bottom boundaries:

$$\frac{\partial c}{\partial \mathbf{n}} = \frac{\partial \phi_{soln}}{\partial \mathbf{n}} = \mathbf{i}_{\mathbf{n},soln} = 0 \tag{5.58}$$

For the bottom of each electrode:

$$\frac{\partial \phi_{solid}}{\partial \mathbf{n}} = 0. \tag{5.59}$$

Current is collected at the top of the electrodes surfaces and the solid-phase current density is taken to be uniform across the top of the electrodes, hence:

$$-\sigma_{pos}^{eff}\frac{\partial\phi_{solid}}{\partial\mathbf{n}} = -I_y \text{ at the top of the positive electrode.}$$

and

$$-\sigma_{neg}^{eff}\frac{\partial\phi_{solid}}{\partial\mathbf{n}} = I_y \text{ at the top of the negative electrode.} \quad (5.60)$$

We set $\phi_{solid} = 0$ at the top centre of the Pb electrode in order to obtain a particular solution.

The material data used for the simulation are documented in Appendix A.4.

Results

In this section we compare the results of the two-dimensional finite element model with those of Bernardi *et al* for the same base input values.

The linear finite element mesh used for the simulation is shown in Figure 5.3. Both the mesh density and time interval were extensively convergence tested for solution accuracy. The time stepping algorithm used was the backwards difference method. The time step interval was 50 seconds. Solution times for a typical transient solution for this model were around 4 hours on a 300 Mhz UltraSparc II. The modified Newton-Raphson technique is employed to solve the set of non-linear equations as it has overall faster solution convergence properties for the coupled set of equations.

The model is discharged at a constant current density of 2.98 Acm^{-2}, based on the plate cross section. This equates to a current density of 25.8 mAcm^{-2} over the cross sectional area of the separator. The base case parameters are documented in Appendix A.4.

All the graphs have been converted to dimensionless units in the x and y directions. The dimensionless cell height is defined as y/H, and the dimensionless width is defined as x/L_{tot}, where H is the cell height and L_{tot} is the total cell width.

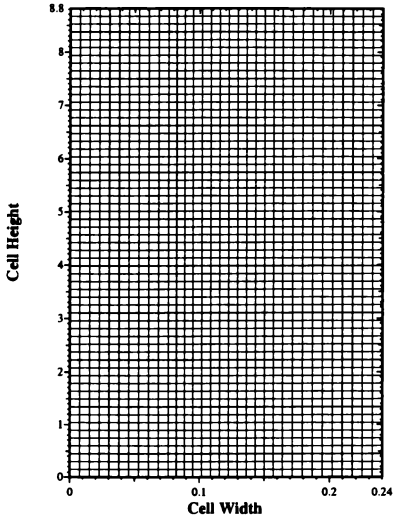

Figure 5.3: Quadrilateral finite element mesh used to model lead-acid cell with Bernardi *et al* parameters.

Figures 5.4 and 5.5 compare the reaction-rate distributions of the current finite element and Bernardi *et al* models at the beginning of discharge. We can see that there is good agreement of data between the models. Note that even for this low rate of discharge there are large variations in reaction-rates within the cell. For example, the reaction-rate doubles from the bottom to the top of the electrodes. Secondary current distributions [Newman 73], are responsible for the reaction-rate distribution. In the cathode, the solid-phase potential, ϕ_{solid} varies approximately 17 mV from the top of the electrode to the bottom, as shown in Figure 5.6. The ohmic potential drop due to the conductivity of PbO_2 is the primary cause of the reaction-rates distribution in the cathode. This is in contrast to the anode, where ϕ_{solid} varies less that 1 mV in the electrode. This is due to the much higher conductivity of Pb. Hence the non-uniform reaction-rate in the cathode causes the non-uniform reaction-rate in the anode.

[b]

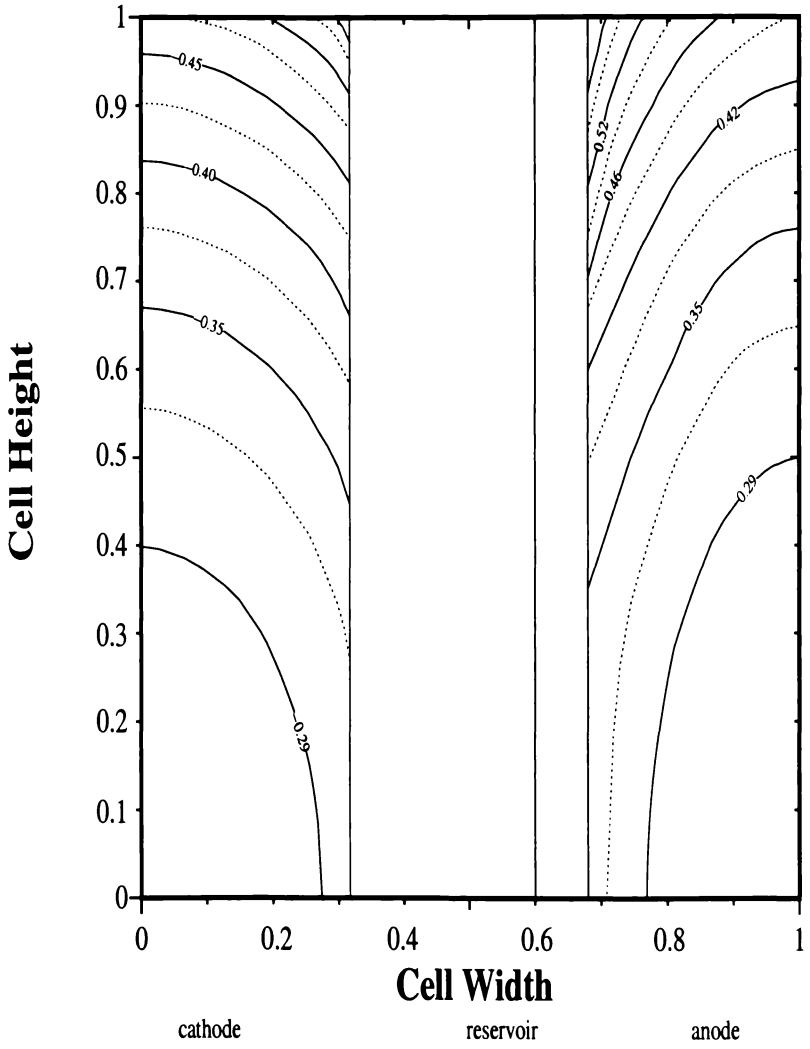

Figure 5.4: Reaction-rate contours at t=0, for the finite element model.

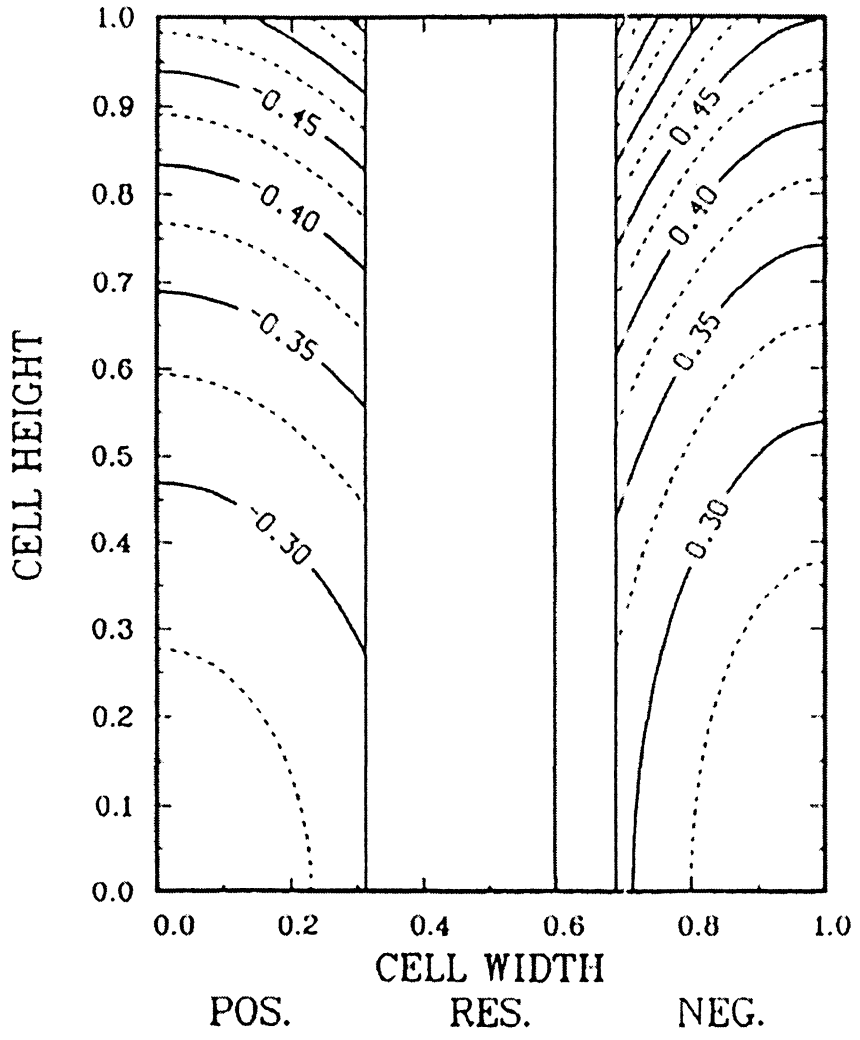

Figure 5.5: Reaction-rate contours at t=0, for the Bernardi *et al* model.

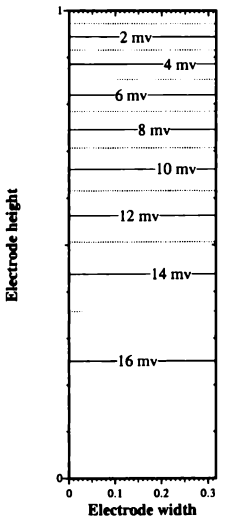

Figure 5.6: Solid-phase potential distribution in the positive electrode.

Figures 5.7 and 5.8 show the solution potential distribution in the cell region of both the current finite element model and the Bernardi *et al* model at the beginning of discharge. The potential contours agree well with one another, and the overall solution potential difference is very close ($\sim$ 20mV). The values differ because Bernardi *et al* reference the solution potential to the top of reservoir/separator interface.

In the anode, the solution-phase potential contours are approximately the same shape as the reaction rate contours (Figure 5.4). This is because the overpotential, η, $\approx \phi_{soln}$, and ϕ_{soln} is small.

The concentration, porosity, and local utilisation which is initially uniform, will become increasingly non-uniform as the discharge progresses due to the non-uniform reaction-rate distribution shown in Figure 5.4.

Figure 5.10 shows the contour distribution of the electrolyte after 1200 seconds of discharge for the finite element and the Bernardi *et al* models. There is reasonably good agreement of data between the graphs. The overall trends between both plots are very similar, and the values are within a few percent of one another. Sulphuric

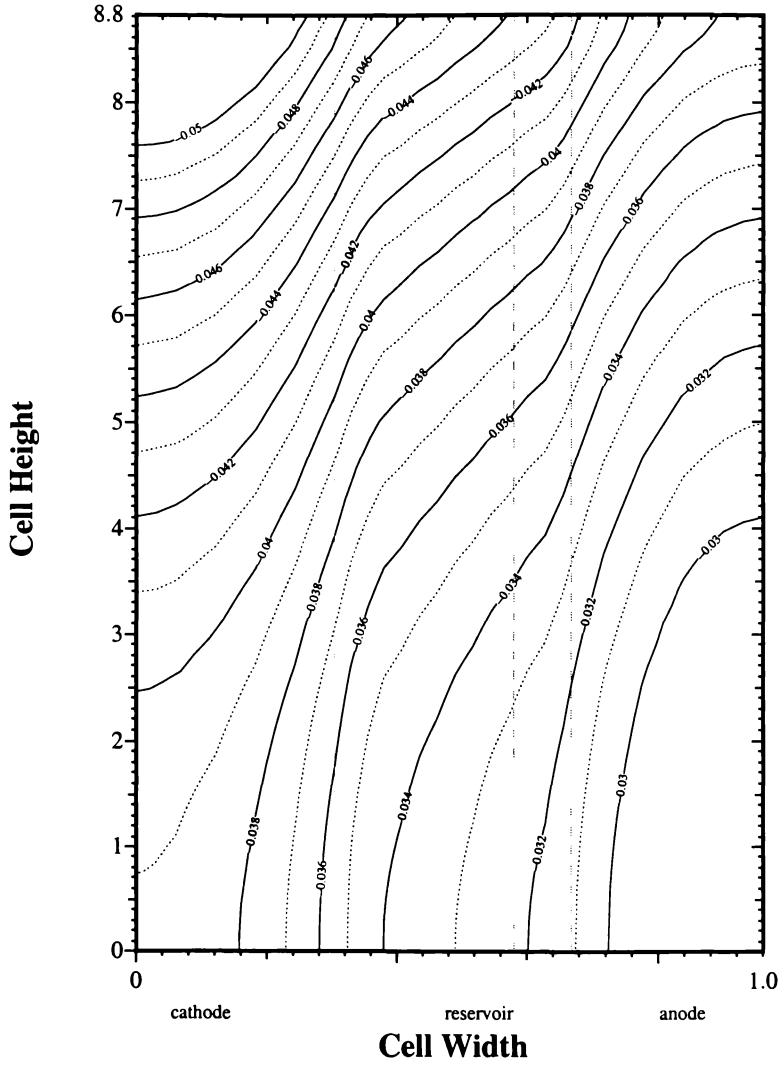

Figure 5.7: Solution potential contours at t=0 for the solution potential of the current finite element model.

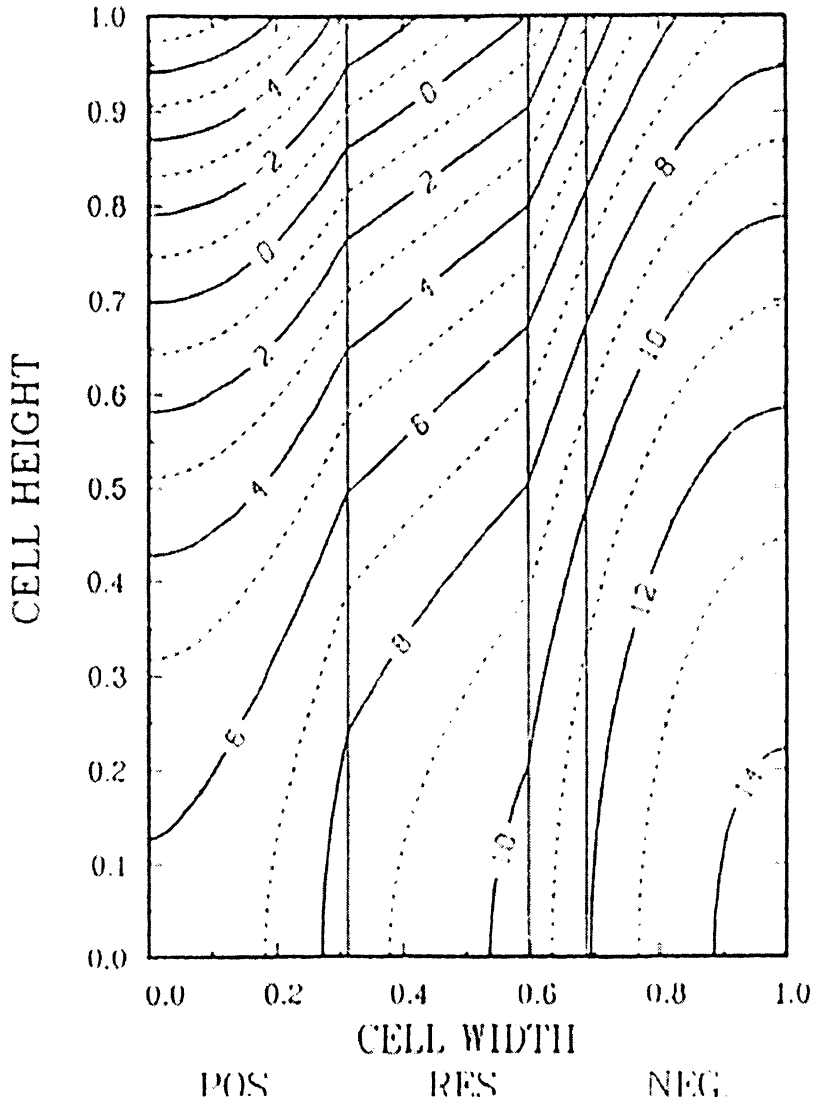

Figure 5.8: Solution potential contours at t=0 for the solution potential of the Bernardi *et al* model.

acid is consumed in both the electrodes during discharge, and $PbSO_4$ is produced. However the acid concentration is generally higher in the anode than in the cathode. This is because the reaction in the cathode produces water and hence dilutes the acid (equation 5.1). Also hydrogen ions are consumed in the cathode [Bode 77] hence reducing the ability of the electrode to carry solution current. The region where the acid concentration is highest corresponds to where the initial reaction-rate is lowest, the bottom centre of the anode. The lowest acid concentration is at the top centre of the cathode. This because the region has a high reaction-rate and sulphuric acid has a low diffusion constant. Hence the front of the electrodes have a higher concentration of acid than at their centres. The acid is consumed at a faster rate than it can be replenished with from the reservoir.

Figures 5.11 and 5.12 show the reaction rate contours for the respective finite element and Bernardi *et al* models after 1200 seconds of discharge. There is reasonable agreement between the two graphs. The reaction-rate in the electrodes is now more uniform with respect to height. $PbSO_4$ produced in the electrodes can cover active material and this reduces reaction-rates particularly where they were greatest. This means that other, less used areas of the electrode react at more favorable rates and hence reaction-rates become more uniform. The other main influence on the reaction-rates is the concentration of electrolyte. This influence is two-fold. Lower concentrations of H_2SO_4 mean there is less active material to react; and the conductivity of H_2SO_4 drops quite dramatically with decreases in concentration, which increases the concentration over-potential and reduces the reaction-rates in the cathode. In the model $\gamma_{neg} = 0$, and hence H_2SO_4 has no influence on the kinetics of the anode. This results in the anode having a less uniform reaction-rate in the y-direction than the cathode.

Figures 5.13 and 5.14 present the porosity contours at 1200 seconds of discharge for the current finite element model and the Bernardi *et al* model at the base

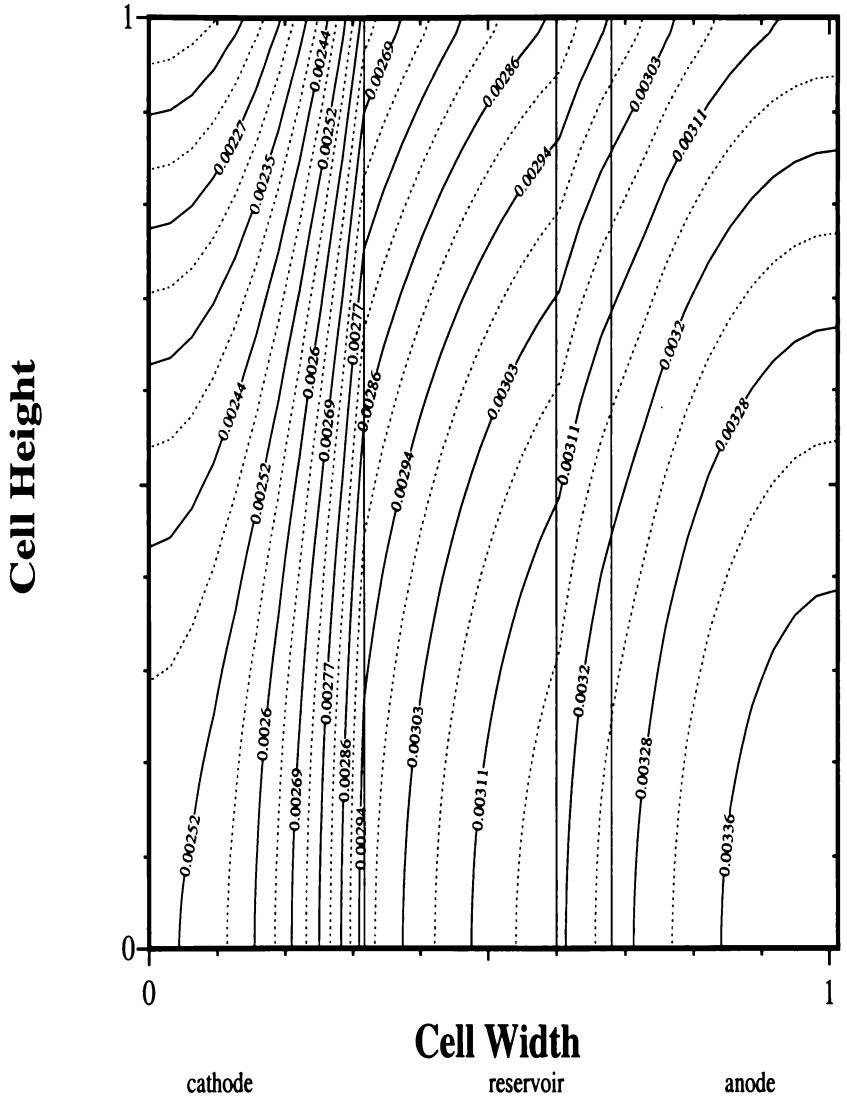

Figure 5.9: Concentration contour profiles of sulphuric acid in the cell at t=1200s of discharge for both the finite element model. Concentration is in molarity units.

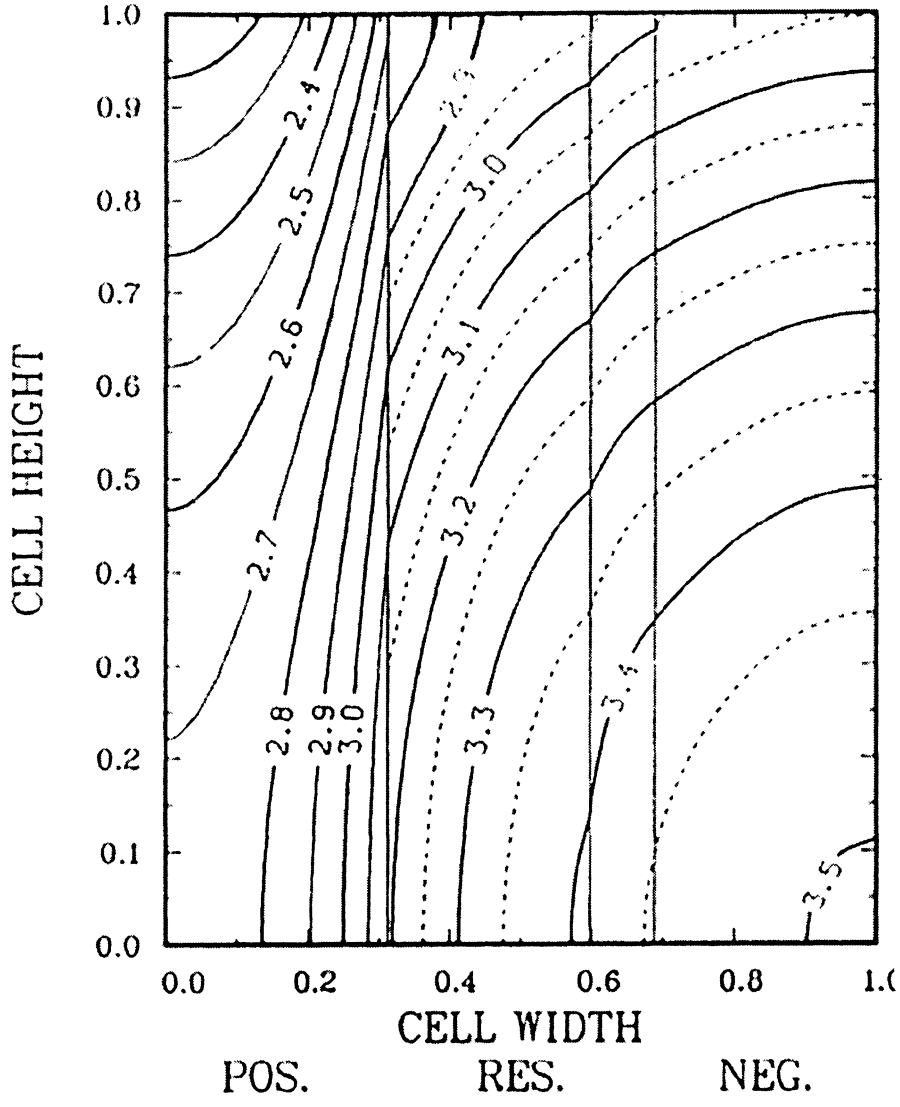

Figure 5.10: Concentration contour profiles of sulphuric acid in the cell at t=1200s of discharge for the Bernardi *et al* model. Concentration is in molarity units.

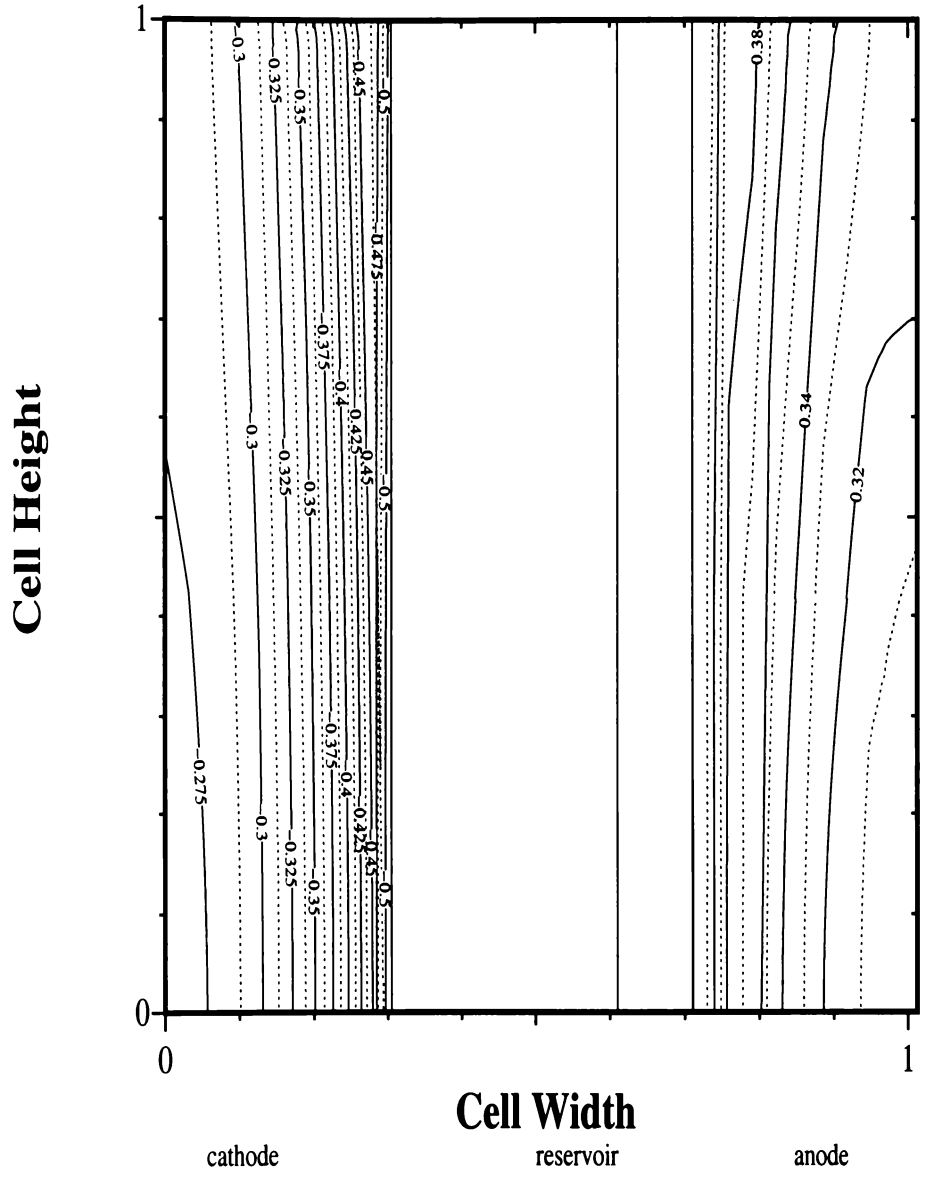

Figure 5.11: The reaction-rate contour distributions after 1200 s of discharge for the current finite element model.

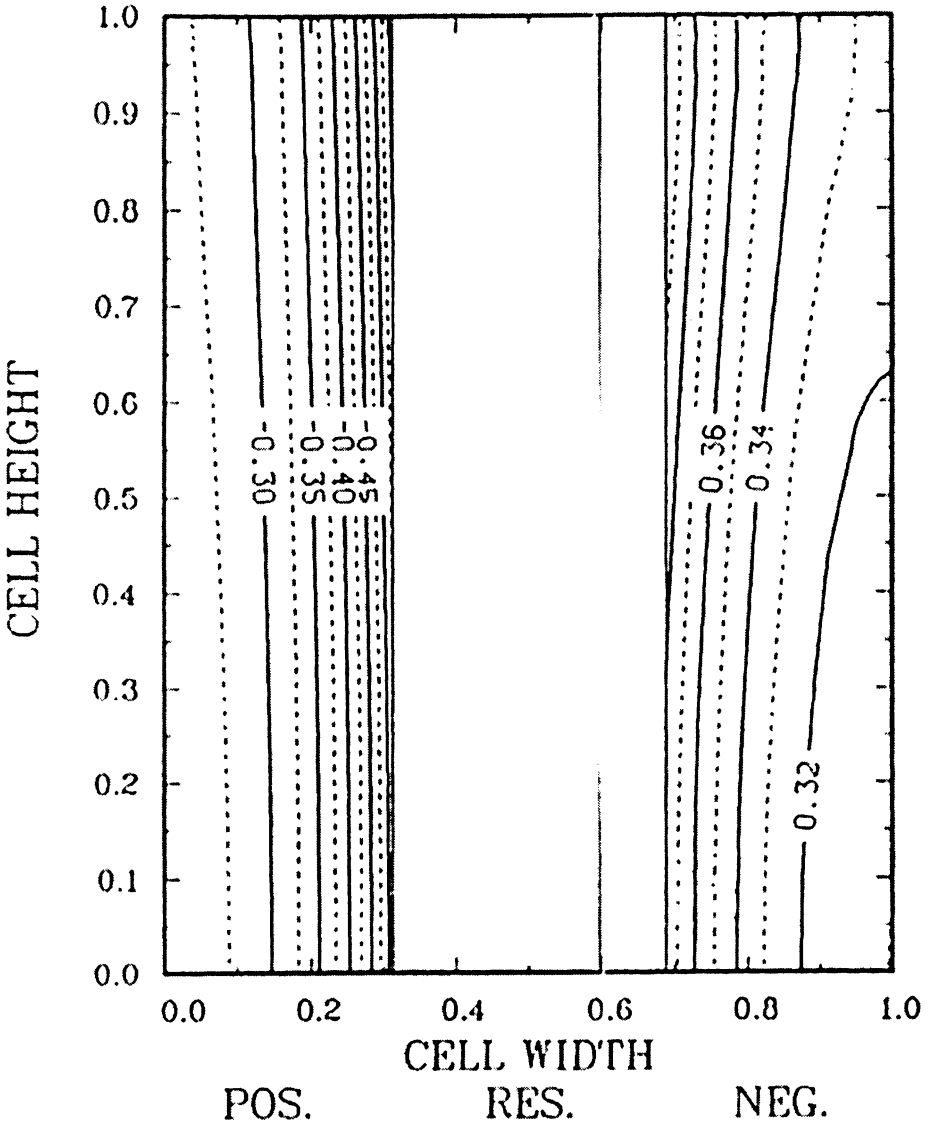

Figure 5.12: The reaction-rate contour distributions after 1200 s of discharge for the Bernardi *et al* model.

conditions. The porosity values and contours of the two models agree very well. Note that as the greater molar volume of $PbSO_4$ compared to PbO_2 and Pb causes the decrease in porosity as the active material reacts. The regions where the maximum reduction of porosity occur are where the reaction-rates are highest, i.e. towards the front/top of the electrodes.

Figure 5.15 compares the calculated cell voltage during a discharge of 25.7 mA/cm^2 based on separator area. There is very good agreement of data.

The comparison of the contour plot between the present finite element model and the Bernardi *et al* model is a testing benchmark. The results compare well with one another, the over all trends are the same, and the numbers agree within a few percent of one another.

5.5.3 Comparison with the Mao *et al* Model

Mao *et al* presented an interesting model in several ways. It was the first macrohomogeneous model utilising finite elements; and it is concerned with geometrical parameters and how they influence the discharge characteristics of a lead-acid battery; it is a simple model in that it uses a single differential equation to describe a lead-acid battery in the steady-state There are several interesting results from their model. They show that grid parameters in fact have little influence on the output of a battery. Reducing the separator width increases the output current of the battery. The transfer current distribution is very sensitive to the electrode reaction kinetics. They infer from this result that the active material utilisation and electrode rechargeability are strongly influenced by electrode design and that such design must therefore take into account of the kinetics of the electrode reactions.

An interesting application of the above results is to examine how the grid design influences how fast cells can be recharged In a discharged state, the solid matrix conductivity is severely reduced as both Pb and PbO_2 have been converted into $PbSO_4$, and the electrolyte concentration and conductivity are depleted. How

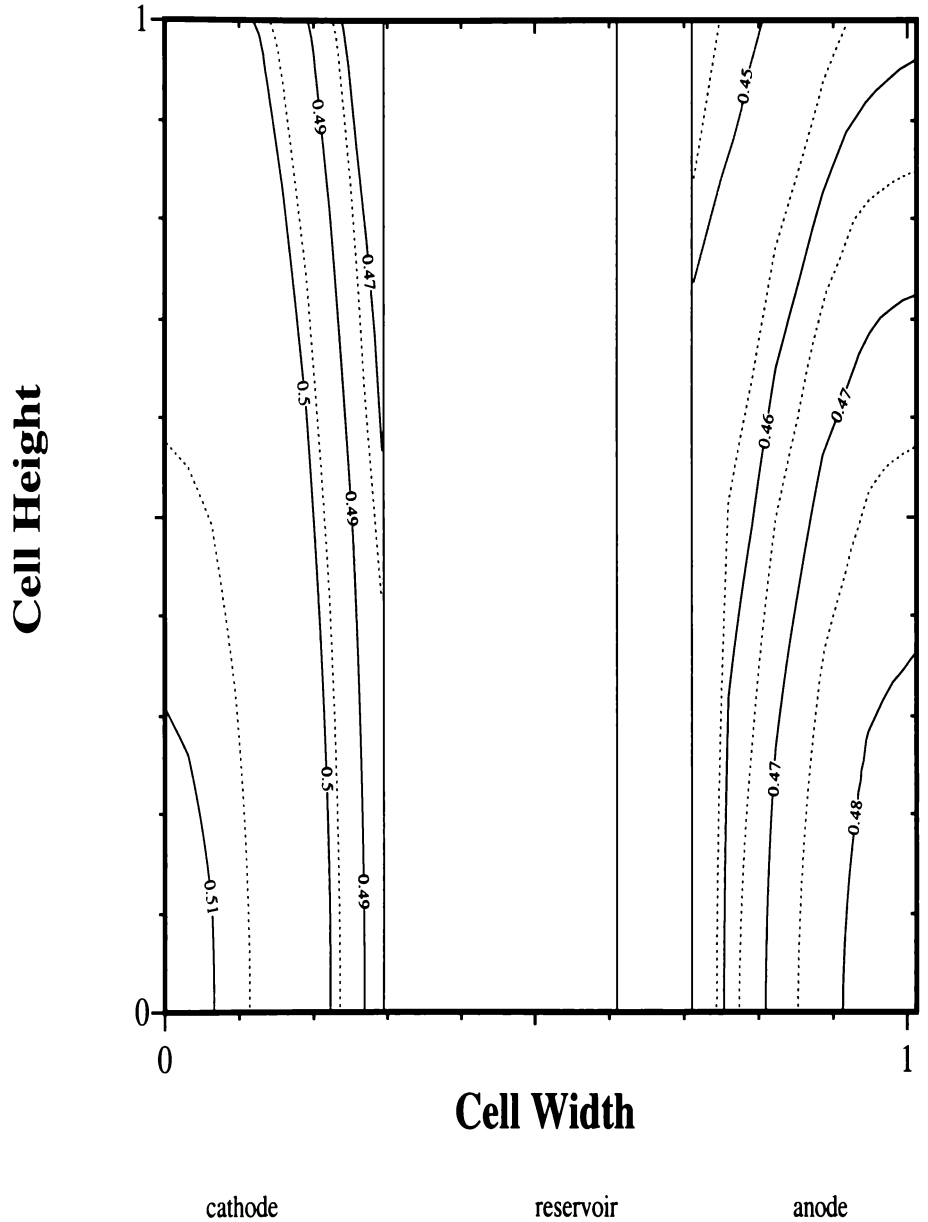

Figure 5.13: Porosity contour profiles after 1200 s of discharge for the current finite element model.

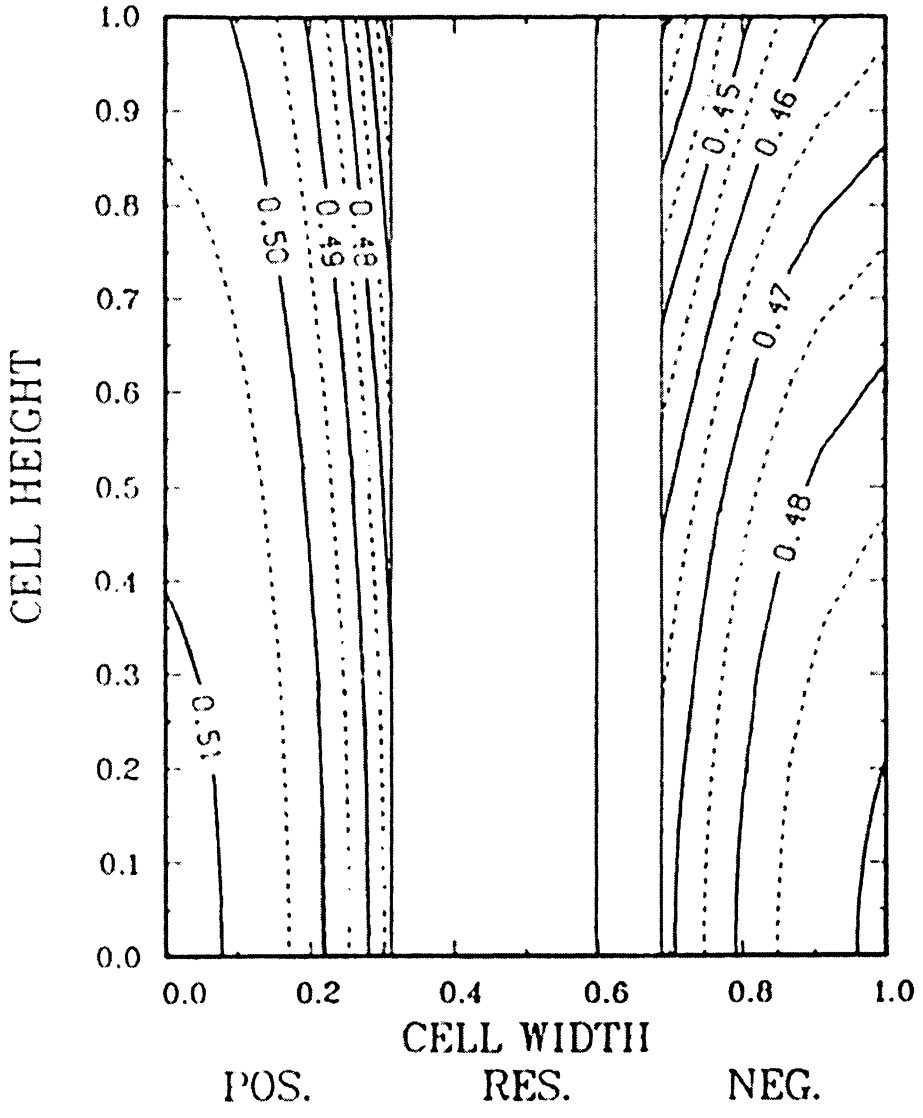

Figure 5.14: Porosity contour profiles after 1200 s of discharge for the Bernardi *et al* model.

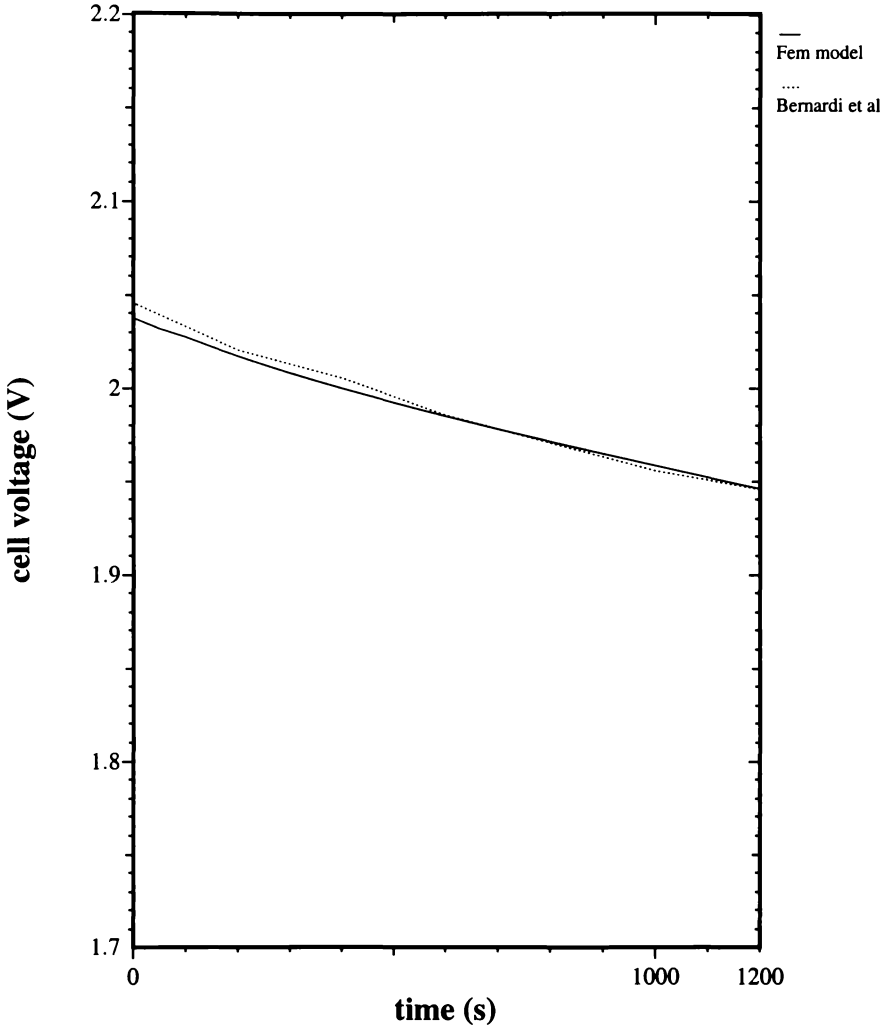

Figure 5.15: Comparison of the cell voltage during discharge at 25.7 mA/cm^2 between the finite element and Bernardi *et al* models.

does the reaction-rate etc. change as the battery gets more and more discharged? How valid are the models under conditions of partial discharge.

Mao *et al* [Mao 91] presented a simple two dimensional steady state finite element model based on Newman's macrohomogeneous theory utilising the IMSL finite element package PDE/PROTRAN [IMSL]. They derived a Poisson partial differential equation with a Butler-Volmer forcing function to represent the kinetics of the electrochemical reaction, i.e.

$$-\kappa_{eff,c}\nabla^2\phi_{soln} - A_a i_{c,0}\left[e^{\frac{\alpha_a F}{RT}\eta} - e^{-\frac{\alpha_c F}{RT}\eta}\right] = 0 \qquad \text{in the cathode;} \tag{5.61}$$

$$-\kappa_{eff,a}\nabla^2\phi_{soln} - A_a i_{c,0}\left[e^{\frac{\beta_a F}{RT}\eta} - e^{-\frac{\beta_c F}{RT}\eta}\right] = 0 \qquad \text{in the anode;} \tag{5.62}$$

where $\kappa_{eff,i}$ represents the effective conductivity of the electrolyte in region i multiplied by a correction term using the following equation:

$$\kappa_{eff,i} = \kappa\epsilon_i^{1.5} \tag{5.63}$$

and A_i is the specific surface area per unit volume of each electrode.

The electrode over-potential, η for the cathode is:

$$\eta = \phi_{solid} - \phi_{soln} - \Delta U \tag{5.64}$$

and for the anode is:

$$\eta = \phi_{solid} - \phi_{soln} \tag{5.65}$$

Mao *et al* make the assumption that the solid matrix conductivities are so high that the solid potential, ϕ_{solid}, varies insignificantly in the modeled electrodes and is assumed constant within each electrode. Hence if we make the anode the reference potential and set it equal to zero, the overall cell voltage will be:

$$V_{cell} = \phi_{solid,c} - \phi_{solid,a} \tag{5.66}$$

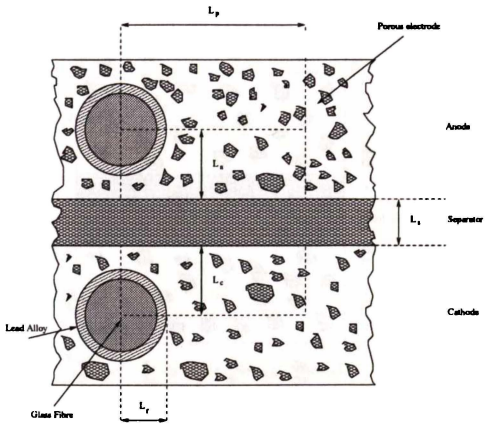

Figure 5.16: Schematic description of Mao *et al*'s two-dimensional region modeled.

The anodic and cathodic current densities j are then calculated for each electrode from the equation:

$$j_i = \frac{\kappa_{eff,i}}{A_i} \nabla^2 \phi_{soln} \tag{5.67}$$

Figure 5.16 shows a cross section of a pair of battery plates. The dashed lines detail the region modeled. The boundary conditions of the modeled domain are given by:

$$-\kappa_{eff} \frac{\partial \phi_{soln}}{\partial \mathbf{n}} = 0 \tag{5.68}$$

The model is applied to the Electrosource advanced HORIZON® battery system and investigates the effects of grid design, plate separation and geometry on the potential and current density distributions on battery performance.

The material data used by Mao *et al* is given in Appendix A.6. Mao *et al*'s data is derived from that of Gu *et al*'s, [Gu 87], but uses different transfer coefficients. Gu *et al*'s data is summarised in Appendix A.2.

Discussion of the Finite Element Model

We again take equations (5.3) to (5.7) and solve for the base initial conditions, viz constant concentration and porosity. The boundary conditions for the model are given in Figure 5.17. As before, we apply symmetry at the centre of both electrodes

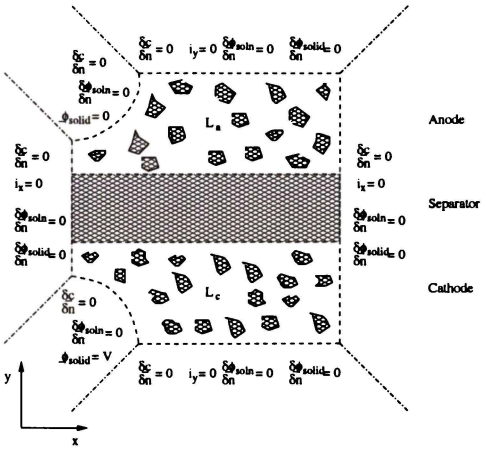

Figure 5.17: Schematic description of boundary conditions applied to finite element model with Mao *et al* input parameters.

and the left and right borders of the modeled region. The left border is the centre of the grid in the x-direction, and the modeled region can be reflected to the left of the axis of symmetry. Similarly we can reflect the modeled region on the right border. The symmetry assumption on the right and left borders is based on negligible variations on the modeled scale in the battery. These assumptions obviously break down when there are significant variations in the plates on a scale that is not negligible on the inter-grid scale.

The parameters in two-dimensions are on a volume basis, i.e. parameters such as current are measured in Acm^{-3}. In the z-direction, we use standard terminology and model a unit length [Zienkiewicz 89].

Results

In this section we will present results with the same input parameters as the steady state model of Mao *et al.* The plots of the solution potential, ϕ_{soln}, solution current i_{soln}, reaction-rates j are solved from the initial conditions of the concentration, c. The cell is discharged at a constant potential, 0.1 V below the rest potential of 2.1277V.

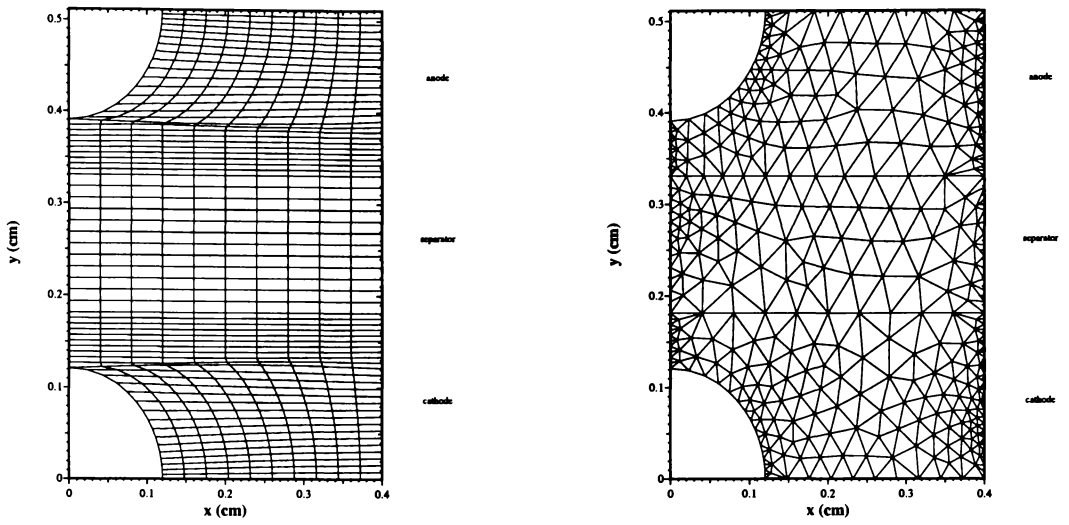

Figure 5.18: Quadrilateral and triangular finite element meshes used to model Mao *et al* model

The mesh was rigorously tested for accuracy and convergence to a reliable solution. Figure 5.18 shows the linear quadrilateral and triangular finite element mesh used. The triangular and quadrilateral meshes yielded the same results.

Figure 5.19 shows almost identical results for the reaction-rate profiles for the current finite element model and the Mao *et al* model for the same input parameters. We can see that the transfer current is highly non-linear within each electrode along the y axis, peaking at approximately 1 Acm^{-3} along the front sides of the electrodes, and at a minimum at the centre of both electrodes. The reaction rate proceeds at almost 3 times the rate at the front of the electrodes than at the centres.

Figure 5.20 compares the solution potential distributions for the current finite element and Mao *et al* models. The solution potential values differ for both models due to the fact that the current finite element model references the solid phase potential, ϕ_{solid}, to the grid wire of the anode, and the solution phase potentials, ϕ_{soln}, are calculated implicitly in the model. The Mao *et al* model is simpler and the ϕ_{soln} does not require a referenced value in order to obtain a particular solution. This results

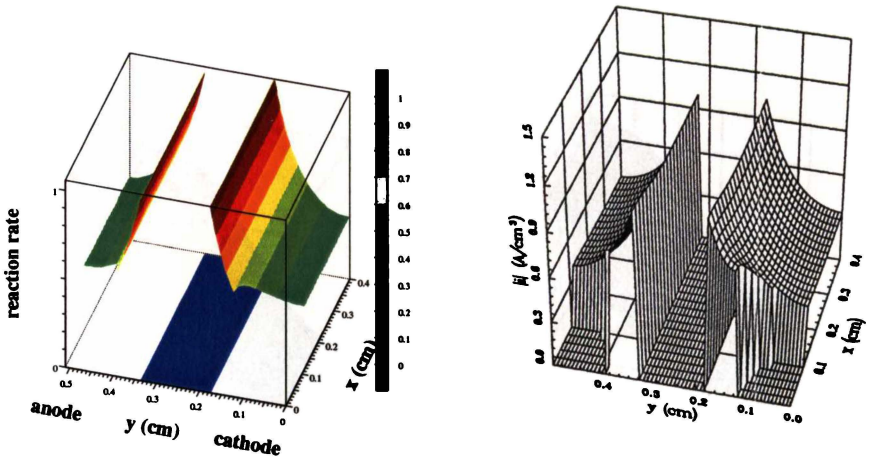

Figure 5.19: The predicted reaction rates of the present finite element model (left), and the Mao *et at* model (right).

in a symmetric potential distribution between the electrodes. What is important is that both results have the same solution potential difference across the cell, and both potential distributions are practically identical. This represents good agreement of data.

The solution current i_{soln} in the modeled cell is shown in Figure 5.21. For the modeled condition, Figure 5.21 shows a discharge current density of 94 mAcm^{-3}. This value is for a unit thick in the z-direction. In Mao *et al*, the calculated current density is calculated by integrating the reaction rate for an electrode. They calculate for the base conditions a value of approximately 37 mA for a thickness in the z-direction of 0.4 cm. This corresponds to a current density of 92 mAcm^{-3}.

For completeness we show the other significant unknown in the current finite element model, the concentration, c, 10 seconds into discharge in Figure 5.22. We can see that at early stages of discharge the concentration profile is also very uniform

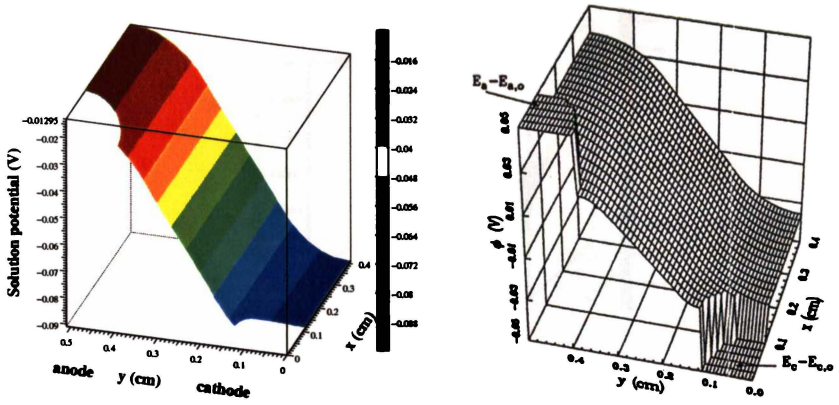

Figure 5.20: The predicted potential distribution for a discharge at 0.1V below open circuit voltage. The finite element model is on the left. Mao *et al*'s model is on the right.

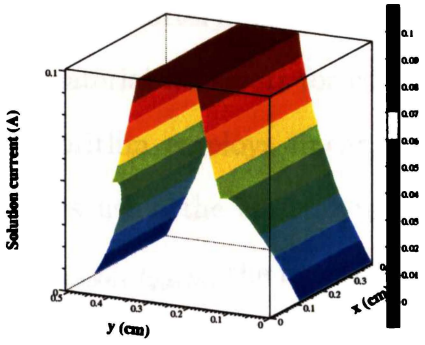

Figure 5.21: The predicted solution current distribution at the start of discharge for the present finite element model.

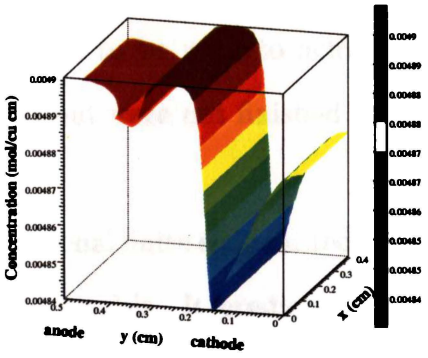

Figure 5.22: The concentration profile 10 seconds into a discharge at 2.0277V (0.1V below open circuit voltage)

in the x-direction, but that there is significant reduction of electrolyte at the front of the cathode.

5.6 Conclusion

A two-dimensional finite element model has been developed to simulate the discharge behavior of a lead-acid battery, incorporating the coupled processes of electrochemical kinetics and material transport for concentrated electrolyte theory.

The finite element algorithm employs linear, isoparametric triangular and quadrilateral C_0 finite elements using the electrolyte concentration, c, the components of the solution current, $i_{x,soln}$, $i_{y,soln}$, the reaction-rates, j, and the solution and solid-phase potentials, ϕ_{soln} and ϕ_{solid}, as the dependent variables. The approach applies the equations uniformly throughout each region in a lead-acid cell. The method easily accommodates arbitrary shapes within the domain and on the boundaries, it readily caters for prescribed variations in material properties and facilitates

mesh grading. The equations non-linear equations were linearised with a modified Newton-Raphson technique.

The application of higher order elements should result in more accurate solutions, facilitating less elements to be used to achieve the same result. Parabolic elements have been developed but were not finished in time for this work to be presented.

The present two-dimensional finite element technique has been carefully benchmarked against two published models. It predicted almost identical results for the same simulated parameters.

The model uses the "standard" set of Newman's macrohomogeneous flooded porous electrochemical equations [Newman *et al* 62], and applies them uniformly throughout the cell. These equations are equally applicable in each region.

The equations (5.3) to (5.7) are not optimal in terms of computationally efficiency. They were chosen as a starting point to maintain consistency with previously published models [Gu 87], [Nguyen *et al* 90], [Mao 91], [Bern *et al* 93]. This facilitates a way of evaluating the finite element method against other approaches.

CHAPTER 6
Conclusion and Future Work

6.1 Conclusions

This thesis has investigated the applicability of the finite element method to Newmans's macrohomogenous equations [Newman *et al* 62]. The technique was successfully used to model one-dimensional and two-dimensional lead-acid battery systems. The method of investigation was an engineering approach rather than mathematical. That is, the principles are applied using intuition, analogies from other fields such as computational fluid dynamics and numerical experimentation applied to the problems reflecting the practice. The emphasis has not been on mathematical rigor, exactly formulation definitions and proofs. The validation of this approach is that the results be carefully benchmarked against other published methods. This has successfully been done with four previously published papers [Gu 87], [Nguyen *et al* 90], [Bern *et al* 93] and [Mao 91]. There was good agreement of data with all models.

This techniqe offers signifcant improvements in region modeling, boundary condition matching, and computational efficiency over all previously published papers. Only the recently plublished paper by Gu *et al* [Gu 97] has treated the equations in such a consistant matter to each region of an electrochemical cell, but are unable to offer the simplicity and generality in geometry modeling that the presented finite element method offers. For instance completely different lead-acid cells with varying input material data and completely different geometry can be modeled and simulated in less than an hour.

6.2 Future Work

This work is an initial investigation into the applicability of the finite element method to Newman's macrohomogeneous equations. It used what can be called a "standard" set of macrohomogeneous equations. The recent paper by Gu *et al* [Gu 97], reformulated the standard set of macrohomogenous equations with three explicit unknowns, the solid potential, ϕ_{solid}, solution potential ϕ_{soln}, and acid concentration, c. In addition, Gu *et al* [Gu 97] included fluid dynamics equations and were able to solve for stratification. A computational fluid dynamics finite difference algorithm was used to solve the set of equations. As stated above, this formulation is computationally more efficient. Using the new formulation for the finite element algorithm present should result in good improvement in computational time and use of computing resources.

The two-dimensional results presented used linear quadrilateral isoparametric elements. Similar linear triangular elements have been developed. Linear elements give a constant variation across the element. The application of higher order elements should result in more accurate solutions and require less elements to achieve the same result. This work is nearly completed.

The inclusion of fluid dynamic equations in principle pose no problems in the solution of the macrohomogeneous equations, apart from increasing computational times.

The techniques presented in this thesis have convergence problems for high discharge rates, when the equations become even more non-linear. More advanced algorithms could be employed to aid in the solution of the equations. For example, in all of the present work to date the total loading function is applied in a single step. In other subject areas it is customary to apply the load as a series of small increments [Zienkiewicz 89]. This incremental approach essentially traces out the non-linear response of the system to a monotonically increasing load function. This

approach has been found to have superior convergence properties and it is expected that by using this method the macrohomogeneous equations will have a large window of convergence [Zienkiewicz 89].

This thesis has treated the macrohomogeneous equations as fully coupled system of equations. If the equations were decoupled, and solved in an iterative manor, huge gains in terms of computational resources could result. This technique is often applied in computational fluid dynamics [Cuvelier 85]. The algorithm can be extended to three dimensions so that a full cell can be modeled. This would allow the considerable non-uniformities of reaction-rate, potential and concentration that develop along both the electrodes height and width of the electrodes to be analysed.

Optimisation algorithms extensively used in structural analysis when applied to the macrohomogeneous equations could result in interesting and perhaps unexpected optimal electrode designs [Zienkiewicz 89]

However there will be a huge computational burden unless more advanced algorithms are developed to reduce the computational resources. Once again work in this area should result in excellent gains. The solution method used was the general black box solver Sparse [Kundert 1988]. More advanced and optimised algorithms will result in faster solution times [Barret *et al* 1994].

The commercial finite element package ANSYS was used to model the boundary domain and generate the quadrilateral mesh. The ANSYS scripting language ADPL was used to output the mesh and boundary conditions. ADPL can also be used to develop specific selecting commands so that the geometry and mesh making phases of an analysis can be a relatively minor exercise.

APPENDIX A
Base Parameters for a Lead-Acid Battery

The following data are the base parameters used for all the models in this thesis for lead-acid cells.

A.1 Lead-Acid Physical Properties used in Simulations

Table A.1 shows constants common for all the lead-acid cells modeled.

Table A.1: Base lead-acid physical properties used in simulations [Bode 77].

Quantity	Value
Conductivity of solution phase	
Lead	$4.8 \times 10^4 \mathrm{Scm}^{-2}$
Lead dioxide	$5.0 \times 10^2 \mathrm{Scm}^{-2}$
Conductivity of H_2SO_4 at 298K, κ_{298}	$7.9 \times 10^{-1} \mathrm{Scm}^{-2}$
at 255K, κ_{255}	$2.8 \times 10^{-1} \mathrm{Scm}^{-2}$
Diffusion of H_2SO_4 at 298C, D_{298}	$3.02 \times 10^{-5} \mathrm{cm}^2\mathrm{s}^{-1}$
at 255K, D_{255}	$8.79 \times 10^{-6} \mathrm{cm}^2\mathrm{s}^{-1}$
Faraday's constant, F	9.6487×10^4
Gas constant, R	8.314
Transference number of H^+, t_o	0.72
Molecular Weight of respective species	
MW_{PbSO_4}	3.0325×10^2
MW_{PbO_2}	2.3919×10^2
MW_{Pb}	2.0719×10^2
Density of respective species	
ρ_{PbSO_4}	6.3
ρ_{PbO_2}	9.7
ρ_{Pb}	11.34

A.2 Gu *et al*'s Model Input Parameters

The following values in Table A.2 are base-line values used for the simulation data in a lead-acid cell in Gu *et al*'s model [Gu 87]. They are the typical values and are referenced from previously published papers.

A.3 Nguyen *et al*'s Model Input Parameters

The values in Table A.3 are base-line values used for the simulation data in Nguyen *et al*'s [Nguyen *et al* 90] model for a lead-acid battery.

A.4 Bernardi *et al*'s Model Input Parameters

Tables A.4 and A.5 are the base line values used for the Bernardi *et al* [Bern *et al* 93] two dimensional lead-acid cell model.

A.5 Mao *et al's* Model Input Parameters

The base-line fixed values for Mao *et al*'s model are given in Table A.6. The values are taken from from Gu *et al* [Gu 87] and Bode [Bode 77].

A.6 Concentration/Temperature Dependent Parameters

The equilibrium overpotential ΔU_{PbO_2} (at 25C) is calculated from [Bode 77]:

$$\Delta U = 1.9228.0 + 1.47519 \times 10^{-1} \log m + 6.3552 \times 10^{-2} \log m^2 \qquad \text{(A.1)}$$
$$+7.3772 \times 10^{-2} \log m^3 + 3.3612 \times 10^{-2} \log m^4$$

where the molality of sulphuric acid, m, is given at 25C [Bode 77] by:

$$m = 1.00322 \times 10^3 c + 3.55 \times 10^4 c^2 + 2.17 \times 10^6 c^3 + 2.06 \times 10^8 c^4 \qquad \text{(A.2)}$$

The temperature dependence of the diffusion, D and ion conductivity, κ, of sulphuric acid is given by Gu *et al* [Gu 87]:

$$D = D_{25} \exp\left(\frac{2174}{298.15} - \frac{2174}{T}\right) \qquad \text{(A.3)}$$

$$\kappa = \kappa_{25} \exp\left(\frac{1801}{298.15} - \frac{1801}{T}\right) \tag{A.4}$$

The temperature and concentration dependence of the diffusion, D and ion conductivity, κ, of sulphuric is given by [Tied *et al* 79b]:

$$D = (1.75 + 2.6 \times 10^2 c) \times 10^{-5} e^{(7.29 - \frac{2.174 \times 10^3}{T})} \tag{A.5}$$

$$\kappa = c \times \exp\left(1.1104 + 1.99475 \times 10^2 c - 1.6097781 \times 10^4 c^2 + \frac{3.91695 \times 10^3 - 9.9406 \times 10^4 c - (7.2186 \times 10^5 / T))}{T}\right) \tag{A.6}$$

D and κ are formulated explicitly in terms of c in the equations unless stated. ΔU was not formulated explicitly in terms of c in any of the models. That is, it was determined from the previously calculated time-step value of concentration. This was due to convergence problems when ΔU was calculated explicitly in the governing equations.

Table A.2: Base parameters used for simulations of lead-acid cell [Gu 87].

Quantity	Value
Cathode length (half)	0.06 cm
Reservoir length	0.055 cm
Separator length	0.014 cm
Anode length (half)	0.06 cm
Initial Porosity:	
ϵ_{anode}	0.53
ϵ_{sep}	0.73
$\epsilon_{cathode}$	0.53
Maximum electroactive area,	
A_a	$1.0 \times 10^2 \mathrm{cm}^2/\mathrm{cm}^3$
A_c	$1.0 \times 10^2 \mathrm{cm}^2/\mathrm{cm}^3$
Transfer coefficients	
Anode:	
α_a	0.5
α_c	0.5
Cathode:	
α_a	0.5
α_c	0.5
Reference exchange current density	
$i_{o,anode}$ (25C)	$1.0 \times 10^{-2} \mathrm{Acm}^{-2}$
$i_{o,anode}$ (-18C)	$1.0 \times 10^{-3} \mathrm{Acm}^{-2}$
$i_{o,cathode}$ (25C)	$2.0 \times 10^{-2} \mathrm{Acm}^{-2}$
$i_{o,cathode}$ (-18C)	$2.0 \times 10^{-3} \mathrm{Acm}^{-2}$
Concentrations parameter for i_o, $\gamma_{cathode}$	1.5
γ_{anode}	1.5
$\zeta_{cathode}$	0.55
ζ_{anode}	0.55
Theoretical capacity, $Q_{max,cathode}$	5.66×10^3
$Q_{max,anode}$	5.66×10^3
Initial acid concentration, C_{ref}	$4.9 \times 10^{-3} \mathrm{molcm}^{-3}$
Exponent for tortuosity correction	
ex	1.5
ex_{sep}	3.53
exm	0.5

Table A.3: Base parameters used for simulations of lead-acid cell [Nguyen *et al* 90].

Quantity	Value
Cathode length (half)	0.08 cm
Separator length	0.1 cm
Anode length (half)	0.09 cm
Initial Porosity:	
ϵ_{anode}	0.6
ϵ_{sep}	0.96
Separator saturation, f_{sat}	0.95
$\epsilon_{cathode}$	0.62
Maximum electroactive area:	
A_a	2.3×10^4 cm^2/cm^3
A_c	2.3×10^5 cm^2/cm^3
Apparent transfer coefficients	
Anode:	
α_a	1.55
α_c	0.45
Cathode:	
α_a	1.15
α_c	0.85
Conductivity of solid phase	
σ_{anode}	4.8×10^4 S/cm
$\sigma_{cathode}$	5.0×10^2 S/cm
Reference exchange current density	
$i_{o,anode}$ (25C)	5.0×10^{-6} Acm^{-2}
$i_{o,anode}$ (-18C)	5.0×10^{-7} Acm^{-2}
$i_{o,cathode}$ (25C)	3.2×10^{-7} Acm^{-2}
$i_{o,cathode}$ (-18C)	3.2×10^{-8} Acm^{-2}
Concentrations parameter for i_o, $\gamma_{cathode}$	0.3
γ_{anode}	1.0×10^{-4}
$\gamma_{cathode}$	0.3
ζ_{anode}	1.5
$\zeta_{cathode}$	1.5
Theoretical capacity, $Q_{max,cathode}$	2.62×10^3
$Q_{max,anode}$	3.12×10^3
Initial acid concentration, C_{ref}	4.9×10^{-3} molcm^{-3}
Exponent for tortuosity correction	
ex	1.5
f_{sat}	0.95
exm	0.5

Table A.4: Base parameters used for Bernardi *et al*'s lead-acid cell [Bern *et al* 93].

Quantity	Value
Cell height (active material only), H	8.8 cm
Cell width, L_{tot}	0.243 cm
Cell length (active material only) W	13.8 cm
Reservoir thickness, L_{res}	0.069 cm
Separator thickness, L_{sep}	0.022 cm
Initial Anode porosity, ϵ_{anode}	0.53
Separator porosity, ϵ_{sep}	0.64
Initial Cathode porosity, $\epsilon_{cathode}$	0.55
Separator κ tortuosity exponent, ex_3	2.19
Current density based on separator area, I_x	0.026 A/cm^2
Current density based on plate cross section, I_y^{pos}	2.98 A/cm^2
Current density based on plate cross section, I_y^{neg}	2.98 A/cm^2
Half thickness of plate (including grid), L:	
anode	0.076 cm
cathode	0.076 cm
Volume fraction of inert material:	
anode	0.2
cathode	0.15
Initial Porosity:	
ϵ_{anode}	0.6
ϵ_{sep}	0.96
Separator saturation, f_{sat}	0.95
$\epsilon_{cathode}$	0.62
Maximum electroactive area:	
A_a	2.3 $\times 10^4$ cm^2/cm^3
A_c	2.3 $\times 10^5$ cm^2/cm^3
Apparent transfer coefficients	
Anode:	
α_a	1.55
α_c	0.45

Table A.5: Base parameters used for Bernardi *et al*'s lead-acid cell model [Bern *et al* 93].

Cathode:	
α_a	1.15
α_c	0.85
Conductivity of solid phase	
σ_{anode}	4.8×10^4 Scm^{-1}
$\sigma_{cathode}$	5.0×10^2 Scm^{-1}
Reference exchange current density	
$i_{o,anode}$ (25C)	5.0×10^{-6} Acm^{-2}
$i_{o,cathode}$ (25C)	3.2×10^{-7} Acm^{-2}
Concentrations parameter for i_o, $\gamma_{cathode}$	
γ_{anode}	0.0
$\gamma_{cathode}$	0.3
Morphology parameter ζ_{anode}	1.5
Morphology parameter $\zeta_{cathode}$	1.5
Theoretical capacity ,$Q_{max,cathode}$	2.81×10^3 C cm^{-3}
$Q_{max,anode}$	2.36×10^3Ccm^{-3}
Initial acid concentration,C_{ref}	4.9×10^{-3} mol cm^{-3}
Exponent for tortuosity correction	
ex	1.5
f_{sat}	0.95
exm	0.5

Table A.6: Fixed parameters used for Mao *et al*'s lead-acid cell model [Mao 91].

Quantity	Value
A_a	100.0 cm^2/cm^3
A_c	100.0 cm^2/cm^3
α_a	1.0
α_c	1.0
β_a	1.0
β_c	1.0
$i_{a,o}$	2.849×10^{-3} Acm^{-2}
$i_{c,o}$	3.404×10^{-3} Acm^{-2}
ϵ_a	0.61
ϵ_c	0.55
ϵ_s	0.65
Electrolyte conductivity, κ	0.79 Scm^{-1}
Temperature	25C

APPENDIX B
A Note on the Software Utilised

Almost all the software used was in the public domain, mostly under GNU copyright.

The software was developed under a Linux operating system with the g77 compiler, linked in tightly with the emacs editor, ftnchek and the gdb debugger.

No multidimensional finite element software can practically exist without some kind of pre- and post- processing. Fortunately two freeware packages, Geompack and Plotmtv are available (amongst others) that were more than adaquate. Initially the geometry was input by hand, however during the final stages of the project, the commerical finite element package ANSYS was used to generate the geometry and mesh the domain.

B.1 Pre Processing

The manual input of a mesh in two dimensions is much more time consuming than the computer execution of the problem itself. It was originally performed this way in the early years of the FEM. Today programs exist that automatically partition a domain into a mesh of elements. However, mesh generation techniques tend to be commerical, and are generally not published. Geompack by Barry Joe has been extensively published [Joe 91], and is available in source code in the public domain for non-commerical use. It provides a stable, robust, readily configurable meshing package, and has been used extensively in this work. In the final stages of the project, ANSYS was used to generate the geometry, mesh the domain and output a specified data deck suitable for the finite element code.

B.2 Solution

The programs are all programmed in standard Fortran 77. The solution of the non-symmetric [A]{x} = {b} matrix systems utilised several different black box routines. The main solver used the "Sparse" package off of Netlib. Naglibs non-symmetric solver, f04atf was used from time to time when available.

A pentium 133 with 64M of RAM running Linux was used to for most of the code construction and results generation. It provided ample speed for all the one-dimensional models and small two-dimensional models. An Ultra Sparc II running at 300Mhz with 384M of RAM was used to run the large two-dimensional models.

B.3 Post Processing

All the post processing of the fem models in this thesis utilises Plotmtv, a freeware package written by Kenny Toh of Intel Corp. It has a simple but functional graphical user interface (gui) on X11, can displace full 2D and 3D surface, line and scatter plots, contour plots as well as vector plot. It can generate either colour or greyscale postscript output files. The gui allows one to rotate, zoom, or pan the data to generate the most suitable visualisation for the postscript plot.

APPENDIX C
Structure of Fem Programs Used

C.1 Program Layout

The finite element program implements the theory developed in Chapter 3 and is programmed in the standard top-down manner in Fortan 77. The program follows the general structure outlined in figure C.1.

At the beginning of the interval all the initial conditions are input for the end of each time-step. The mesh is then calculated for the required input spacings. The program then begins the start of the interval.

Inside each time interval, the coupled non-linear equations are solved iteratively by using either of the two Newton methods discussed in Chapter 3.

Firstly the equations are "solved" for each element of the grid and assembled into their appropriate Jacobian and residual matrices. The relevant boundary conditions are then applied to the assembled system of equations. The resultant assembled Jacobian matrix is sparse, banded and non-symmetric.

The System of equations are then solved using a black-box solver. A detailed explanation of the solvers used is given in Appendices B.

The Newton iteration continues with the new Jacobian (not for the modified Netwon method) and residual matrices being calculated and assembled to the existing Jacobian and residual matrices. This iterative cycle continues until suitable convergence is attained. The solution for the time interval is then outputed.

The program then increments in time and the next solution is solved. The theta time-stepping method (discussed in Chapter 3) is used to give the ability to

switch between explicit and implicit methods at each interval. It was found that the backward difference method provided the the most stable time-stepping approach.

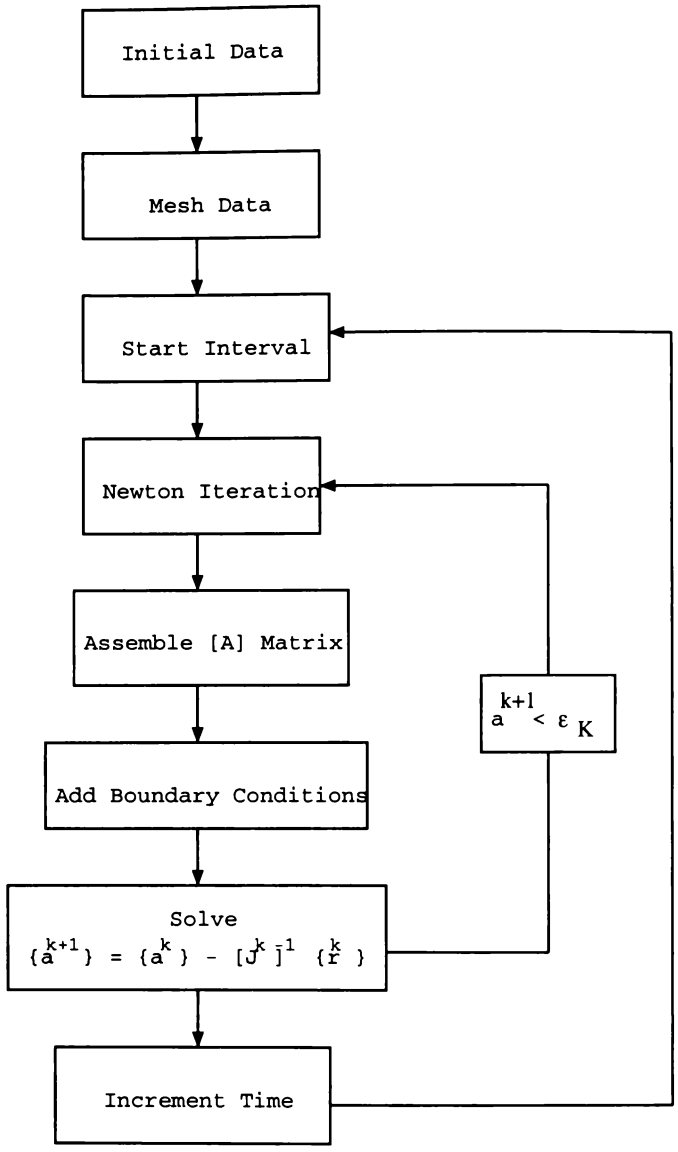

Figure C.1: Block diagram of Newton-type solution technique for each time interval.

APPENDIX D
Input Data Format Specification for Two Dimensional FEM Model

The following data deck documents the input data deck for the two dimensional finite element model used in Chapter 5.

D.1 Data Deck

The data deck is specified for six partial differential equations.

Title

No. nodes, No. elements, No. regions, No. coeffs, No. derv b.c. , debug level

time start, No. intervals, theta, time interval

region(i), a_{max}(i), Q_{max}(i), ex(i), i_0(i), ,c_0(i), γ(i), α_a(i), α_c(i), δU(i), i=1, No. regions

region(i), asolx(i), capax(i), i=1, No. regions

region(i), asoly(i), capay(i), i=1, No. regions

region(i), dcurx(i), dcury(i), sgsdx(i), sgsdy(i), i=1, No. regions

region(i), epcoef(i), bconst(i), i=1, No. regions

region(i), diffx(i), diffy(i), OneK(i), twoK(i), i=1, No. regions

x(i), y(i), i=1, No. nodes

n, nmtl(i), (nel(i,j), j=1, nodes in element), i=1, No. elements

equation(i), initial condition(i), i=1, No. equations

deriv bc.No(i),deriv b.c.node(i,1),deriv b.c.node(i,2), 1=1,No. dbc

ib(i), esbcNo(i), bv(i), i=1,nebc

REFERENCES

[Alav *et al* 91] Alavyoon, A., Eklund, A., Bark, F. H., Karlsson, R. I., and Simonsson, D., (1991): *Electrochim. Acta*, **36**, 2157.

[Barret *et al* 1994] Barret, R., Berry, M., Chan, T., Demmel, J., Donato, J.,Dongarra, J., Eijkhour, V., Pozo, R., Romine, C., and Van der Vorst, H., (1994): Templates for the Solution of Linear Systems: Building Blocks for Iterative Methods, *Netlib.*

[Bern *et al* 93] Bernardi, D. M., Gu, H., and Schoene, A.Y., (1993): Two-Dimensional Mathematical Model of a Lead-Acid Cell, *J. Electrochem. Soc.*, **140**, 2250.

[Berndt 70] Berndt, D., (1970): *Power Sources 2*, Pergamon, 17.

[Bode 77] Bode, H., (1977): Lead-Acid Batteries, *Wiley-Interscience Publication.*

[Buchanan 95] Buchanan, G. R., (1995): Finite Element Analysis, *McGraw-Hill.*

[Bullock 94] Bullock, K., R., (1994): Lead/acid batteries, *J. Power Sources*,**51**, 1.

[Burnett 87] Burnett, D.S., (1987): Finite Element Analysis, *Addison Wesley Publishing Company.*

[Choi 78] Choi, K.W., and Yao, N.P., (1978): Thermal Analysis of Lead-Acid Cells for Load-Levelling Applications, *J. Electrochem. Soc.*, **125**, 1011.

[Choi 79] Choi, K.W., and Yao, N.P., (1979): Heat Transfer in Lead-Acid Batteries Designed for Electric-Vehicle Propulsion Application, *J. Electrochem. Soc.*, **126**, 1321.

[Cuvelier 85] Cuvelier, C., Segal, A., and van Steenhoven, A.A., (1985): Finite Element Methods and Navier-Stokes Equations, *D. Reidel Publishing Company.*

[de Levie 67a] de Levie, R., *Advances in Electrochemistry and Electrrochemical Engineering*, Wiley-interscience, New York 1967, **6**, 327.

[de Levie 67b] de Levie, J., (1967): Electrochemical Response of Porous and Rough Electrodes,, *Advanced Electrochemical Engineering*, **329**, 329.

[Dimp 88] Dimpault-Darcy, E.C., Nguyen, T. V., and White, R. E., (1988): Two-Dimensional Mathematical Model of a Porous Lead Dioxide Electrode in a Lead-Acid Cell, *J. Electrochem. Soc.*, **135**, 278.

[Dun 71] Dunning, J. S. (1971): *Analysis of Porous Electrodes with Sparingly Soluble Reactants*, dissertation, University of California.

[Dun *et al* 71] Dunning, J. S., and Newman, J. (1971): Analysis of Porous Electrodes with Sparingly Soluble Reactants, *J. Electrochem. Soc.*, **118**, 1251.

[Euler 60] Euler, J., and Nonenmacher, W., (1960): *Electrochimica Acta*, **2**, 268.

[Euler 61] Euler, J., (1961): *Electrochimica Acta*, **4**, 27.

[Fraure 1881] Fraure, C.A., (1881), *Compt Rend.*, **92**, 951.

[Garcia 94] Garcia, A.L., (1994): Numerical methods For Physicists, *Prentice-Hall Inc.*.

[Gid *et al* 73] Gidaspow D., and Baker, B.S., (1973): A Model for Discharge of Storage Batteries, *J. Electrochem. Soc.*, **120**, 1005.

[Gu 83] Gu, H., (1983): , *J. Electrochem. Soc.*, **130**, 1461.

[Gu 87] Gu, H., and Nguyen, T. V., (1987): A Mathematical Model of a Lead-Acid Cell, *J. Electrochem. Soc.*, **134**, 2953.

[Gu 97] Gu, W. B., Wang C.Y., and Liaw, B.Y., (1997): Numerical Modeling of Coupled Electrochemical and Transport Processes in Lead-Acid Batteries, *J. Electrochem. Soc.*, **144**, 2053.

[Gugg 59] Gugenheim, E. A., (1959): Thermodynamics, *North Holland Publishing Company, Amsterdam.*

[Hint 76] Hinton E., Rock, R., and ZienkiewiczO .C., (1976), A Note on Mass Lumping and related Processes in the Finite Element Method, *Earthquake Eng. Struct. Dyn.*, **4**, 245-249.

[IMSL] (1989): PDE/PROTRAN, A System for the Solution of Partial Differential Equations, IMSL, Inc.

[Jam 74] Jammer, M., (1974): The Philosophy of Quantum Mechanics, *Wiley and Sons, New York.*

[Joe 91] Joe, B., (1991), GEOMPACK – a software package for the generation of meshes using geometric algorithms, *Adv. Eng. Software* , **13**, 325.

[Joe86] Joe, B., (1986), Delaunay triangular meshes in convex polygons, *SIAM J. Sci. Stat. Comput.*, **7**, 514-539.

[Joe89] Joe, B., (1989), Three-dimensional triangulations from local transformations, *SIAM J. Sci. Stat. Comput.*, **10**, 718-741.

[Joe91a] Joe, B.,(1991), Construction of three-dimensional Delaunay triangulations using local transformations,*Computer Aided Geometric Design*, **8**, 123-142.

[Joe91b] Joe, B., (1991), Delaunay versus max-min solid angle triangulations for three-dimensional mesh generation, *Intern. J. Num. Met. Eng.*, **31**, 987-997.

[Joe92] Joe, B., (1992), Three-dimensional boundary-constrained triangulations, *"Artificial Intelligence, Expert Systems, and Symbolic Computing"*, ed. E. N. Houstis and J. R. Rice, Elsevier Science Publishers, 215-222.

[Joe93] Joe, B.,(1993), Construction of k-dimensional Delaunay triangulations using local transformations, *SIAM J. Sci. Comput.*, **14**, 1415-1436.

[Joe94] Joe, B., (1994), Tetrahedral mesh generation in polyhedral regions based on convex polyhedron decompositions, *Intern. J. Num. Meth. Eng.*, **37**, 693-713.

[JoeS86] Joe, B., and Simpson R.B., (1986), Triangular meshes for regions of complicated shape, Intern. J. Num. Meth. Eng., 23, pp. 751-778.

[Johnson 87] Johnson, C., (1987): Numerical Solution of Partial Differential Equations by the Finite Element Method, *Press Syndicate of the University of Cambridge.*

[Koch 59] Koch, D.F.A., (1959): *Electrochimica Acta*, **1**, 32.

[Kundert 1988] Kundert, K. S., (1988): *Berkeley University via Netlib* A Sparse Linear Equation Solver.

[Lee 86] Lee, J., Choi, K.W., Yao, N.P., and Christianson, C. C., (1986): *J. Electrochem. Soc.*, **133**, 1286.

[Macsyma] Macsyma, (1993): Macsyma System Reference Manual, Version 14, *Macsyma Inc.*

[Mao 91] Mao, Z., White, R. E., and Jay, B., (1991): Current Distribution in a HORIZON Lead-Acid Battery during Discharge, *J. Electrochem. Soc.*, **138**, 1615.

[Mer 62] Meredith, R.E., and Tobias, C.W., (1962): Advances in Electrochemistry and Electrochemical Engineering, Vol 2, C.W. Tobias, Editor, *Interscience Publishers, NY.*

[Micka *et al* 73] Micka, K., and Roušar, I. (1973): Kinetics of the Porous Lead Electrode in the Lead-Acid Battery, *Electrochim. Acta*, **18**, 629.

[Micka *et al* 74] Micka, K., and Roušar, I. (1974): Kinetics of the Porous Lead Electrode in the Lead-Acid Battery, *Electrochim. Acta*, **19**, 499.

[Micka *et al* 76] Micka, K., and Roušar, I. (1976): Theory of Porous Electrodes-XIV The Lead-Acid Cell, *Electrochim. Acta*, **21**, 599.

[Morimoto *et al* 88] Morimoto, Y., Ohya, Y., Abe, K., Yoshida, T., and Morimoto, H., (1988): , *J. Electrochem. Soc.*, **135**, 293.

[NAG] NAG: The Numerical Algorithms Group Ltd, Oxford UK.

[Newman 73] Newman, J., (1973): Electrochemical Systems, *Prentice Hall, Englewoord Cliffs, NJ.*

[Newman 75] Newman, J., (1975): Porous-Electrode Theory with Battery Applications, *AIChE Journal*, **21**, 25.

[Newman *et al* 62] Newman, J., and Tobias, C.W., (1962): Theoretical Analysis of Current Distribution in Porous Electrodes, *J. Electrochem. Soc.*, **109**, 1183.

[Newman *et al* 93] Newman, J., Tiedemann, W., (1993): Potential and Current Distribution in Electrochemical Cells, *J. Electrochem. Soc.*, **140**, 1961.

[Nguyen *et al* 90] Nguyen, T. V.,Gu, H., and White, R. E.(1990): The Effects of Separator Design on the Discharge Performacnce of a Starved Lead-Acid Cell, *J. Electrochem. Soc.*, **137**, 2998.

[Nish *et al* 86] Nishiki, H., (1986): , *J. Applied Electrochem.*, **16**, 291.

[Planté 1872] Plante, G., (1872), *Compt. Rend.*, **74**, 592.

[Planté 1959] Plante, G., (1859), *Compt. rend.*, **49**, 402.

[Prat 80] Patankar S.V., (1980): Numerical Heat Transfer and Fluid Flow; *Hemisphere Publishing Company U.S.A.*.

[Ritter 1803] Ritter, J., W., (1803), 106; *Voight's Magazine* **6** ,195.

[Shep 65] Shepherd, C. M., (1965): *J. Electrochem. Soc.*, **112**, 657.

[Sim 73] Simonsson, D., (1973): Kinetics of the Porous Lead Electrode in the Lead-Acid Battery, *J. Electrochem. Soc.*, **120**, 151.

[Sim *et al* 88] Simonsson, D., Ekdunge, P., and Lindgren, M., (1988): Kinetics of the Porous Lead Electrode in the Lead-Acid Battery, *J. Electrochem. Soc.*, **135**, 1613.

[Simon *et al* 70] Simon, A.C., Wales, C.P. and Caulder, J.S.M., (1970): *J. Electrochem. Soc.*, **117**, 987.

[Stein 58] Stein, W., (1958): *Naturwissenschaften*, **45**, 458.

[Sunu 84] Sunu, W.G., (1984): Mathematical Model for Design of Battery Electrodes: Lead-Acid Cell Modelling, *Electrochemical Cell Design, Plenum Press*, 357.

[Sunu *et al* 81] Sunu, W.G., and Burrows, B.W., (1981): Current Density and Electrolyte Distribution in Motive Power Lead-Acid Cells,, *J. Electrochem. Soc.*, **128**, 1405.

[Sunu *et al* 82] Sunu, W.G., and Burrows, B.W., (1982): Mathematical Model for Design of Battery Electrodes: I. Potential Distribution, *J. Electrochem. Soc.*, **129**, 688.

[Sunu *et al* 84] Sunu, W.G., and Burrows, B.W., (1984): Mathematical Model for Design of Battery Electrodes: II. Current Distribution, *J. Electrochem. Soc.*, **131**, 1.

[Taylor 81] Taylor, C., and Hughes, T. G. (1981): Finite Element Programming of the Navier-Stokes Equations, *Pineridge Press Ltd.*.

[Tied 77] Tiedemann, W., Newman, J., and Dusua, F., (1977): Power Distribution in the Lead-Acid Battery Grid, *Power Sources 6, Academic Press, NY* 15.

[Tied *et al* 79a] Tiedemann, W., Newman, J. (1979): Battery Design and Optimization, *The Electrochemical Society Soft Bound Proceeding Series, Pennington, NJ*, 39.

[Tied *et al* 79b] Tiedemann, W., Newman, J. (1979): Battery Design and Optimization, *The Electrochemical Society Soft Bound Proceeding Series, Pennington, NJ*, 23.

[Vinal 55] Vinal, G.W., (1955): Storage Batteries, *McGraw-Hill, New York.*

[White 85] White, R.E., (1985): An Introduction to the Finite Element Method with Applications To Nonlinear Problems, *Wiley-Interscience Publication.*

[Zienkiewicz 89] Zienkiewicz O.C., (1989): The Finite Element Method; 4th edition; *Mc.Graw-Hill U.K..*